

Data Acquisition and Digital Processing in Nuclear Fusion

Tiago Ferreira de Castro te Lintel Hekkert

Thesis to obtain the Master of Science Degree in

Engineering Physics

Examination Committee

Chairperson: Professor Doctor Horácio João Matos Fernandes
Supervisor: Professor Doctor Bernardo Brotas de Carvalho
Member of the Committee: Doctor António Joaquim Nunes Batista

October 2013

Acknowledgements

It is for me a great pleasure to express here my gratitude to the people whose help made possible the realization of this work.

In the first place I would like to thank my Adviser Professor Doctor Bernardo Brotas de Carvalho for the way that he orientated me through the work, for his availability and patience shown during the making of this thesis. Also for the trust he deposited in me while I was participating on several projects at IPFN or even abroad.

I would like to thank the precious help of Doctor António Batista, Engineer João Fortunato and Engineer Rui Dias with important aspects of the developed ADC modules at IPFN and with their technical knowledge and the aid and always helpful suggestions of Engineer Ivo Carvalho and Engineer Pedro Duarte during the acquisitions at tokamak ISTTOK.

I would like also to express my gratitude to Doctors Manfred Zilker and Andreas Werner for their help during and after a mission to the IPP at Greifswald, Germany.

Thank you all my friends from IST that I made during the course of MEFT, thank you Gonçalo Quintal, Samuel Almeida, António Vito, Pedro Oliveira, Luzia Carias, Tiago Silva, Joana Batista, João Pereira and many others that helped me to cheer difficult times.

Finally I would like to leave a special acknowledge to my family that supported me, in particular for the aid and love given through the years by my parents and family members, Catarina Castro, Carolina António, Carlos António and Catarina Laranjeiro.

Resumo

O tema desta tese aborda Aquisição de Dados e Processamento Digital direccionado para diagnósticos magnéticos usados actualmente na Investigação em Fusão Nuclear. O cerne deste trabalho é a descrição de arquitecturas desenvolvidas em Verilog, algoritmos usados, testes efectuados e os resultados obtidos de aquisições de sinais vindos de bobines de Mirnov do ISTTOK e de montagens construídas. São usados módulos digitais com um modo de Chopper galvanicamente isolados e com uma amostragem a 2MSPS (com 18 bits de resolução) desenvolvidos pelo IPFN (Instituto de Plasmas e Fusão Nuclear, Lisboa).

Na primeira parte desta tese é descrito os princípios físicos básicos da fusão nuclear, os dispositivos que permitem que haja fusão nuclear na Terra e os diagnósticos usados mais comuns. É posteriormente descrito mais em detalhe os diagnósticos magnéticos. No capítulo seguinte é descrito brevemente o estado-de-arte da aquisição de dados e processamento digital direccionado para a fusão nuclear.

O terceiro capítulo descreve as técnicas, arquitecturas e suporte em software para a aquisição de dados e processamento digital durante a realização deste trabalho. O quarto e quinto capítulos estão relacionados com testes, resultados obtidos e a sua análise.

No último capítulo são apresentadas as conclusões principais desta dissertação e são dadas algumas sugestões para a continuação do trabalho feito.

Abstract

This thesis concerns Data Acquisition and Digital Processing related to magnetic diagnostics currently used in Nuclear Fusion Investigation. The core of this thesis is the description of developed architectures in Verilog, used algorithms, the performed tests and obtained results of acquisitions from ISTTOK's Mirnov coils signals and made test assemblies. The used modules are galvanic isolated digital modules with signal chopper mode and a sampling at 2 MSPS (18-bit full resolution data) developed by IPFN (Instituto de Plasmas e Fusão Nuclear, Lisbon).

On the first part is described the basic physical principals of nuclear fusion, as the devices that make nuclear fusion on earth possible and the most popular diagnostics used, it is them described in more detail the magnetic diagnostics. The current situation of the research on nuclear fusion and in more detailed the situation on data acquisition and digital processing is briefly described in chapter two.

The third chapter shows the used technics, architectures, software support for data acquisition and digital processing during this thesis. The forth chapter and the fifth chapter are related to the tests and obtained results from acquisitions and their analysis.

On the final Chapter it is presented the conclusions of this work and it is suggested future works that can be done/continued after this thesis.

Palavras-chave

Fusão Nuclear

Acquisição de dados

Processamento Digital

ATCA

Módulos integradores

Diagnósticos magnéticos

Keywords

Nuclear Fusion

Data Acquisition

Digital Processing

ATCA

Integrator modules

Magnetic diagnostics

Contents

Acknowledgements	iii
Resumo	iv
Abstract	v
Palavras-chave	vi
Keywords	vi
Contents	vii
List of Figures	x
List of Tables	xiv
Acronyms	xv
1 - Introduction	1
1.1 - Fusion	1
1.2 - Types of confinement Methods	2
1.2.1 - Gravitational confinement	2
1.2.2 - Inertial confinement	2
1.2.3 - Magnetic confinement	3
1.3 - Tokamak	3
1.4 - Stellarators	4
1.5 - JET	5
1.6 - ITER	5
1.7 - Tokamak – Heating systems	6
1.7.1 - Ohmic heating	6
1.7.2 - Neutral Beam Injection (NBI)	6
1.7.3 - Radio frequency heating	6
1.8 - Tokamak – Most common diagnostics	6
1.8.1 - Interferometry	6
1.8.2 - Reflectometry	6
1.8.3 - Deflection analyzer of an ion beam	7
1.8.4 - Magnetic measurements	7
2 - State-of-the-Art of integrator modules related to magnetic measurements in Nuclear Fusion	9
3 – Data Processing System	13
3.1 – Introduction	13
3.2 – Data Processing System of ISTTOK	13
3.2.1 - ATCA	14
3.2.2 - FPGA	16
3.2.3 – Real Time Operating System tuning	17
3.2.3.1 – Linux Kernel	17
3.2.3.2 - Real-Time	17
3.2.3.2.1 - RT priority	17
3.2.3.2.2 - Core affinity	17

3.2.3.2.3 - Virtual Memory	18
3.2.5 – Numerical integrators	18
3.3 - Data Processing – Used Software and Firmware	20
3.3.1 - Data Processing on the FPGA.....	20
3.3.2 - Data Processing Algorithm.....	21
3.4 - Architectures	22
3.4.1 - First Project.....	22
3.4.2 – Firmware Architectures developed to ISTTOK.....	23
3.3.3 - Architecture developed for IPP.....	24
4 - Experimental Development.....	28
4.1 – Introduction	28
4.2 - Signal Reconstruction	28
4.2.1 - Signal Reconstruction of a constant voltage.....	28
4.2.2 - Reconstruction of a pure sine signal.....	29
4.2.3 – Long acquisition of a sine signal and numerical integration	29
4.3 – Noise acquisition and integration.....	31
4.3.1 - First set of acquisitions: Post Compensated Drift with constant temperature. ADC modules of 100nF capacitor on the input filter	35
4.3.2 - Second set of acquisitions: Pre Compensated Drift with constant temperature. Modules of 100nF capacitor on the input filter.....	37
4.3.3 - Third set of acquisitions: Pre Compensated Drift of 100s with temperature variation and maximum temperature of 43°C. Modules of 100nF capacitor on the input filter.....	39
4.3.4 – Fourth set of acquisitions: Pre Compensated Drift of 60s with temperature variation and maximum temperature of 43°C. Modules of 100pF capacitor on the input filter.....	42
4.4 - Acquisition of signals from ISTTOK’s Mirnov coils.....	44
4.4.1 – Pulsed Plasma at ISTTOK	45
4.4.2 – AC Plasmas at ISTTOK.....	51
4.5 – Acquisition tests at IPP, Greifswald.....	53
4.5.1 - First set of acquisitions: Acquisition of a short-circuited signal.....	53
4.5.2 - Second set of acquisitions: Tests with a made assembly, simple voltage integration	54
4.5.3 - Third set of acquisitions: Tests with a made assembly, integration of a capacitor discharge	56
4.5.4 - Forth set of acquisitions: Tests with a made assembly, integration of a large number of capacitor discharge (>40), long acquisition of 1000s.....	58
4.5.5 - Fifth set of acquisitions: Test performed in Portugal.....	60
4.5.6 - Sixth set of acquisitions: Test performed remotely in Greifswald.....	61
5 - Results and Discussion	62
5.1 – Introduction	62
5.2 – Noise acquisition and integration.....	62

5.2.1 – Temperature tests and analysis.....	65
5.3 - Acquisition of signals from ISTTOK’s Mirnov coils.....	69
5.3.1 – Plasma current results.....	69
5.3.2 – Testing different Firmware Architectures.....	70
5.4 - Acquisition tests at IPP, Greifswald.....	74
6 - Conclusions.....	75
7 - References and Bibliography.....	76
8 - Appendices.....	79

List of Figures

Figure 1 – Fusion of Tritium and Deuterium	1
Figure 2 – Nuclear binding energy released Vs Atomic mass.....	1
Figure 3 – Plasmas characteristics.....	2
Figure 4- Charged particle movement in a magnetic field.....	3
Figure 5 - Charged particle movement in a tokamak.....	3
Figure 6 – Resulting Helical Magnetic field in a tokamak.....	4
Figure 7 – Scheme of the magnetic coils and the plasma of Wendelstein 7-X.....	4
Figure 8 – Scheme summarizing the operation conditions of several tokamaks	5
Figure 9 –Diagram of electromagnetic signal passing by the plasma (right) and at left it’s possible average plasma density through time (left).....	6
Figure 10 – Main circuits used for integration of analog signals [1]	10
Figure 11 - Circuit of an analog integrator with sample	11
Figure 12 - Principle of the chopper integrator [4].....	11
Figure 13 - Block diagram of digital–analog long-pulse integrator.....	12
Figure 14 - ADC module used	13
Figure 15 – Used ATCA crate with the ADC modules inserted.....	14
Figure 17 – ATCA crate	15
Figure 17 – ATCA board scheme.....	16
Figure 19 – Image of a FPGA	16
Figure 20 – Simplified diagram of Kernel’s interactions.....	17
Figure 21 – Virtual Memory – VM combines active RAM and inactive memory to form a large range of contiguous addresses	18
Figure 21 – Schematic of the digital chopper integrator and the filters and amplifier system before the ADC	19
Figure 22 - Schematic of the digital chopper integrator and the filters and amplifier system before the ADC	19
Figure 23 - Simplified block diagram of the first used architecture	20
Figure 24 - Schematic of the influence of EO and WO	21
Figure 25- Used Software algorithm to make the acquisition	22
Figure 26 - Simplified block diagram of the first used architecture (the dashed box is to separate the clock domain).....	23
Figure 27 – Simplified block diagram of the FPGA architecture	24
Figure 28 – Photographs taken during the tests at IPP, Greifswald. At right is the author programing on-site the parameters for the acquisition and at left is his supervisor.....	25
Figure 29 - Simplified block diagram of the FPGA architecture developed for the IPP.....	25
Figure 30- Simplified block diagram of the used connections related to the clock system.....	26
Figure 31 - Electrical setup for testing the Integrators with a W7-Stelarator magnetic probe.....	27
Figure 32 - Reconstruction of a constant voltage signal (right) and the reconstruction of a constant voltage signal during a transition of the Chopper in detail (left)	28

Figure 33 - Reconstruction of a sine shaped signal (top), reconstruction of a sine shaped signal in detailed (below).....	29
Figure 34 – Detail of Offset of Sine signal	30
Figure 35 – Detail of Fixed Compensated Integral of Sine signal.....	31
Figure 36 – Post-Compensated Drift of one module (acquisition with constant temperature).....	32
Figure 37 – Pre-Compensated long duration Drift of one module (acquisition with constant temperature)	32
Figure 38 - Raw data from a long acquisition of 1000s, it is shown in the image some important values as the Average value and the RMS.....	33
Figure 39 - Post compensated Integral from a long acquisition of 1000s, it is shown in the image some important values as the Average Value and the RMS value.....	34
Figure 40 – Multiplot of all Post-Compensated Drift on acquisition 1a, acquisition done with constant temperature	36
Figure 41 – Multiplot of all Post-Compensated Drift on acquisition 1b, acquisition done with constant temperature	36
Figure 42 - Multiplot of all Pre Compensated Drift on acquisition 2a, acquisition done with constant temperature	38
Figure 43– Multiplot of all Pre Compensated Drift on acquisition 2b, acquisition done with constant temperature	38
Figure 44 - Offset of one module (acquisition with temperature variation).....	40
Figure 45 - Multiplot of all Pre Compensated Drift on acquisition 3a, (acquisition with module heating).....	41
Figure 46 - Multiplot of all Pre Compensated Drift on acquisition 3b, (acquisition with module heating).....	41
Figure 47 - Multiplot of all Pre Compensated Drift on acquisition 4a (acquisition with module heating).....	43
Figure 48 - Multiplot of all Pre Compensated Drift on acquisition 4b (acquisition with module heating).....	43
Figure 49 – Pictures from ISTTOK’s room, at the left is the plug from the signals coming from the Mirnov coils of the tokamak, at the right in the used ATCA crate.....	44
Figure 50 – Raw signals from all the Mirnov coils.....	46
Figure 51 - Integral of the signal from one Mirnov coil during the whole ISTTOK operating sequence (top), and from the plasma discharge (bottom)	47
Figure 52 – Integral of the signal from all coils during the whole ISTTOK operating sequence	48
Figure 53 - Integral of the signal from all coils in detail, on the beginning this graphic the values of the integral were set to zero and some of the signals were inverted.....	49
Figure 54 - Integral of the signal from all coils in detail, on the beginning this graphic the values of the integral were set to zero	50
Figure 55 - Intensity of the signal from all coils in detail, on the beginning this graphic the values of the integral were set to zero.....	51
Figure 56 - Intensity of the signal from all coils, for the full ISTTOK cycle.....	52
Figure 57 - Intensity of the signal from all coils in detail, on the beginning this graphic the values of the integral were set to zero and the some of the signals were inverted.....	53

Figure 58 – Schematic of the first used assembly to test the performance of the module by generating a magnetic field with a DC generator.....	54
Figure 59 - First used assembly.....	55
Figure 60 - Pre-Compensated Integral, the acquisition was during 40 seconds and the pre-compensation was done at 10 seconds.....	55
Figure 61 – Second used Assembly.....	56
Figure 62 – Detail of a Pre-Compensated Integral, the acquisition was during 40 seconds and the pre-compensation was done at 10 seconds.....	56
Figure 63 – Adjustment of an exponential function to the data presented in Figure 62.....	57
Figure 64 - Multiplot of Pre-Compensated Integral, the acquisition was during 1000 seconds and the pre-compensation was done at 100 seconds.....	58
Figure 65 - Pre-Compensated Integral (detail), the acquisition was during 1000 seconds and the pre-compensation was done at 100 seconds.....	59
Figure 66 - Multiplot, detail of the Drift with the Chop signal.....	60
Figure 67 – Multiplot, detail of the Drift with the Chop signal.....	61
Figure 68 - Comparison between WO (or Before Chop Offset) values from different channels in two post compensated acquisitions with constant temperature.....	62
Figure 69 - Comparison between Offset's RMS from different channels in two post compensated acquisitions with constant temperature.....	63
Figure 70 - Final Pre Compensated Drift Values of acquisition 3a and 3b (acquisition with temperature variation).....	64
Figure 71 - Final Pre Compensated Drift Values of acquisition 4a and 4b (acquisition with temperature variation).....	64
Figure 72 - Values of the voltage RMS through the acquired data during acquisition 3a, (acquisition with temperature variation).....	65
Figure 73 - Multiplot of all Pre Compensated Drift on acquisition 3a with the integral of the temperature.....	66
Figure 74 - Multiplot of all Pre Compensated Drift on acquisition 3a with the integral of the temperature.....	67
Figure 75 - Plasma current along time from ISTTOK measured by the Mirnov Coils, shot number 34531.....	69
Figure 76 – Plasma current along time from ISTTOK measured by the Rogowski Coil, shot number 34531. The offset drift trend is shown in blue.....	70
Figure 77 - Drift of a channel after the corrections of EO and WO.....	71
Figure 78 - Integral from a short-circuited signal.....	72
Figure 79 - Integrated Signal coming from the Mirnov coils, during an AC discharge (detail).....	73
Figure 80 – Schematic of part of the ADC module developed by IPFN.....	79
Figure 81 - Schematic of part of the ADC module developed by IPFN.....	80
Figure 82 - Used ATCA board.....	81
Figure 83 - Integral of Sine signal.....	82

Figure 84 - Detail of Integral of Sine signal.....	82
Figure 85 - Offset of one module (acquisition with constant temperature).....	83
Figure 86 - Pre-Compensated Integral, the acquisition was during 40 seconds and the pre-compensation was done at 10 seconds. The difference from figure Figure 60 is that the terminals of the coil were switch and the signal is shown inverted.....	83
Figure 87 - Detail of a Pre-Compensated Integral, the acquisition was during 40 seconds and the pre-compensation was done at 10 seconds.....	84
Figure 88 - Values of the voltage RMS through the acquired data during acquisition 3b, (acquisition with temperature variation).....	84
Figure 89 – Autocorrelation of the compensated integral of noise (the terminals of the module were short-circuited), the acquisition lasted 10 seconds	85
Figure 90 - Autocorrelation of the compensated integral of noise (the terminals of the module were short-circuited), the acquisition lasted 100 seconds	85
Figure 91 - Autocorrelation of the compensated integral of noise (the terminals of the module were short-circuited). The acquisition lasted 100 seconds, it is the same as in Figure 90, but the autocorrelation was limited to the first 10 seconds.....	86
Figure 92 - Multiplot of all Pre Compensated Drift on acquisition 3a with the integral of the temperature adjusted to the channel 2 integral curve.....	87
Figure 93 - Multiplot of all Pre Compensated Drift on acquisition 3a with the integral of the temperature adjusted to the channel 1 integral curve.....	88
Figure 94 - Multiplot of all Pre Compensated Drift on acquisition 3a with the integral of the temperature adjusted to the channel 0 integral curve.....	88
Figure 95 - Multiplot of all Pre Compensated Drift on acquisition 3b with the integral of the temperature adjusted to the channel 2 integral curve.....	89
Figure 96 - Multiplot of all Pre Compensated Drift on acquisition 3b with the integral of the temperature adjusted to the channel 1 integral curve.....	89
Figure 97 - Multiplot of all Pre Compensated Drift on acquisition 3b with the integral of the temperature adjusted to the channel 0 integral curve.....	90
Figure 98 - Multiplot of all Pre Compensated Drift on acquisition 4a with the integral of the temperature adjusted to the channel 2 integral curve.....	90
Figure 99 - Multiplot of all Pre Compensated Drift on acquisition 4a with the integral of the temperature adjusted to the channel 1 integral curve.....	91
Figure 100 - Multiplot of all Pre Compensated Drift on acquisition 4a with the integral of the temperature adjusted to the channel 0 integral curve.....	91
Figure 101 - Multiplot of all Pre Compensated Drift on acquisition 4b with the integral of the temperature adjusted to the channel 2 integral curve.....	92
Figure 102 - Multiplot of all Pre Compensated Drift on acquisition 4b with the integral of the temperature adjusted to the channel 1 integral curve.....	92
Figure 103 - Multiplot of all Pre Compensated Drift on acquisition 4b with the integral of the temperature adjusted to the channel 0 integral curve.....	93

List of Tables

Table 1 – Acronyms	xv
Table 2 – Characteristics of several types of analog signals integrators, presented before in Figure 10 [1]	10
Table 3 - Resume of Offset EO and Offset WO values	35
Table 4 – Resume of RMS and Deviation values of Post-Compensated Drift	35
Table 5 – Resume of RMS and Deviation values of Offset	35
Table 6 - Resume of Offset EO and Offset WO values	37
Table 7 - Resume of RMS and Deviation values of Pre Compensated Drift.....	37
Table 8 - Resume of RMS and Deviation values of Offset	37
Table 9 - Resume of EO and WO values with temperature variation	39
Table 10 - Resume of RMS and Deviation values of Pre Compensated Drift with temperature variation.	39
Table 11 - Resume of RMS and Deviation values of Offset with temperature variation	39
Table 12 - Resume of EO and WO values with temperature variation	42
Table 13 - Resume of RMS and Deviation values of Pre Compensated Drift with temperature variation.	42
Table 14 - Resume of RMS and Deviation values of Offset with temperature variation	42
Table 15 – Used ADC modules.....	45
Table 16 – EO parameter values	50
Table 17 - WO parameter values.....	51
Table 18 - Resume of EO and WO values	54
Table 19 - Resume of EO and WO values	60
Table 20 - Resume of Offset EO and Offset WO values	61
Table 21 – Resume of the calculated temperature correction factors.....	68
Table 22 - Resume of the calculated temperature correction factors and its deviation	68
Table 23 – EO and WO comparison, acquisitions with different Chop frequency	74

Acronyms

ADC	Analogue to Digital Converter
ATCA	Advanced Telecommunications Computing Architecture
CPU	Central processing unit
DAC	Digital to Analogue Converter
DAQ	Data acquisition systems
DMA	Direct Memory Access
DRAM	Dynamic Random Access Memory
ENOB	Effective Number Of Bits
EO	Electronics Offset
ESD	Electrostatic Discharge
FIFO	First In, First Out
FPGA	Field Programmable Gate Array
FW	Firmware
HDL	Hardware description language
IOCTL	input/output control
IPFN	Instituto de Plasmas e Fusão Nuclear
IPP	Max-Planck-Institut für Plasmaphysik
IRQ	Interrupt Request
IST	Instituto Superior Técnico
ISTTOK	Instituto Superior Técnico Tokamak
NEBS	Network Equipment-Building System
OS	Operating System
PC	Personal computer
PCI	Peripheral Component Interconnect
PCIe	Peripheral Component Interconnect Express
PLL	Phase-locked loop
RT	Real-Time
RTOS	Real-Time Operating Systems
SCADA	Supervisory Control and Data Acquisition
SICADA	Sistema de Controlo e Aquisição de Dados do ISTTOK
SW	Software
VHDL	VHSIC Hardware Description Language
VHSIC	Very High Speed Integrated Circuits
VMEbus	VersaModular Eurocard bus
VM	Virtual Memory
WO	Wiring Offset

Table 1 – Acronyms

1 - Introduction

1.1 - Fusion

Nuclear fusion powers the sun and the other stars and is a promising source of energy to support the increasing world demand. It consists on the light-z nuclei combination with the mass reduction of the products in comparison with the reagents and the consequent energy release.

After a fusion reaction, the total masses are less than before, the “missing” mass is converted into energy, as quantified by the well-known Einstein equation:

$$E = (m_r - m_p)c^2 \quad (1)$$

Where E is the energy resulting from the reaction, m_r is the mass of the nuclei before the reaction, m_p is the mass of the nuclei after the reaction, and c is the speed of light. As an example it is schematized the fusion of Tritium and Deuterium in Figure 1 and Equation (2).

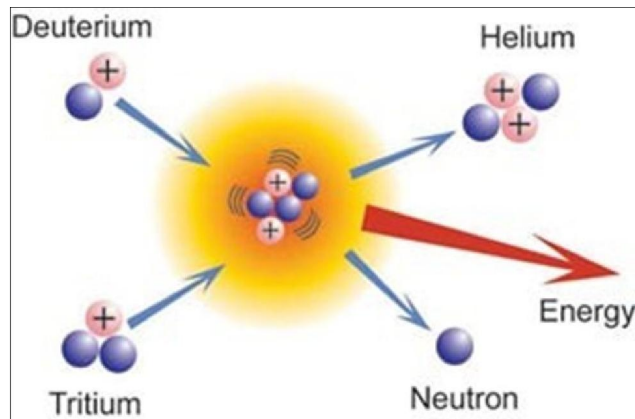
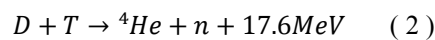


Figure 1 – Fusion of Tritium and Deuterium



Nuclear fission, regarding fusion, is the separation of a heavy nucleus with energy release. Figure 2 is a simple diagram that shows the nuclear binding energy released in Fusion and in Fission. It is easily verified that the amount of energy that can be obtain in nuclear fusion is much higher than in nuclear fission.

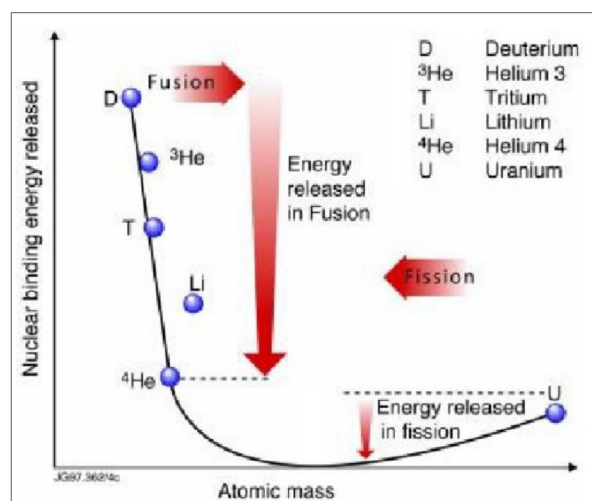


Figure 2 – Nuclear binding energy released Vs Atomic mass

In order to induce the fusion of two nuclei it is necessary to overcome the mutual repulsion due to their positive charges (the distances between reagents have to be small enough to have the nuclear force being bigger than the electrostatic forces). The most promising method of supplying the energy is to heat the reagents to a sufficient high temperature so that the thermal velocities of the nuclei are high enough to produce the required reactions. At these temperatures the fusion fuel will ionize and constitute a plasma. In Figure 3 it is shown several types of plasmas and the conditions of temperature and density needed.

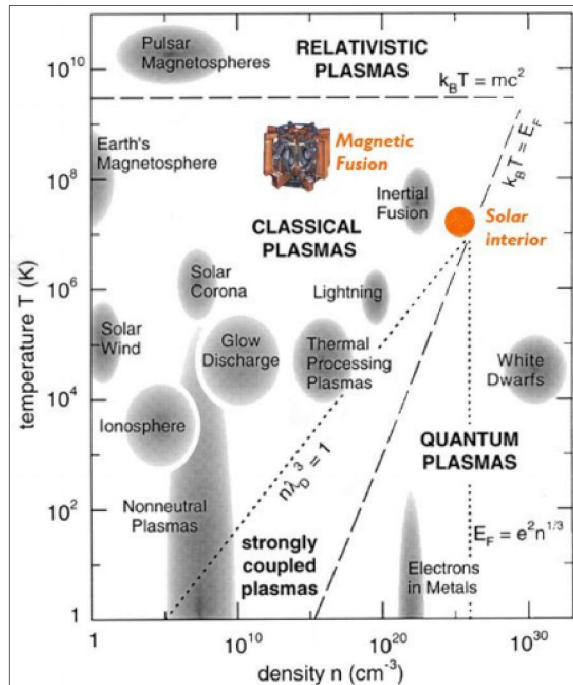


Figure 3 – Plasmas characteristics

Because the reaction activation occurs due to a random thermal motion of the reacting

nuclei, this process is therefore called thermonuclear fusion. The critical technical requirement is the sustainment of a sufficiently stable high temperature ($\sim 10^8\text{K}$) plasma in a practical reaction volume and for a sufficiently long period of time to render the entire process energetically viable.

1.2 - Types of confinement Methods

There are only three studied plasma confinement methods possible to have nuclear fusion, the gravitational confinement, the magnetic confinement and the inertial confinement.

1.2.1 - Gravitational confinement

Nuclear fusion reactions occur in the stars by the confinement of the reagents through gravitational forces associated to their immense mass.

As we enter the interior of a star the density and the temperature of the reagents is bigger in a way that is possible to have fusion reactions. The generated energy is big enough to compensate the energy losses on the stars surface.

Confinement by gravity is not possible on earth due to the dimensions and masses that is necessary.

1.2.2 - Inertial confinement

Inertial confinement fusion (ICF) is a process where nuclear fusion reactions are initiated by heating and compressing a fuel target, typically in the form of a pellet that most often contains a mixture of deuterium and tritium. The energy is delivered to the small fuel pellet by electromagnetic radiation of a very potent laser or due to the action of high power ion beam.

1.2.3 - Magnetic confinement

A fusion plasma cannot be maintained at thermonuclear temperatures if it is allowed to come in contact with the walls of the confinement chamber, because material eroded from the walls would quickly cool the plasma. In fusion investigation magnetic fields can be used to confine a plasma within a chamber without contact with the wall.

A charged particle moving in a magnetic field will experience a Lorentz force, Equation (3), which is perpendicular to both the direction of particle motion and to the magnetic field direction.

$$m \frac{d}{dt} v = q(v \times B) \quad (3)$$

The particle in a magnetic field will move along the field and circle about it; that is, will spiral about the field line. (Figure 4)

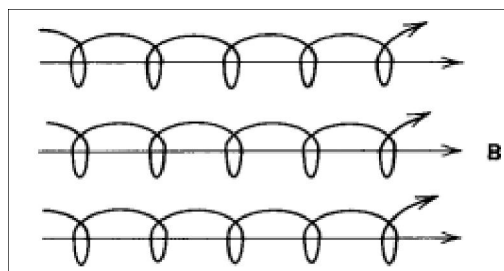


Figure 4- Charged particle movement in a magnetic field

1.3 - Tokamak

Closed Toroidal Confinement Systems (Tokamak) - The magnetic field lines may be configured to remain completely within a confinement chamber by the proper choice of position and currents in a set of magnetic coils. Particles following along the closed toroidal field lines would remain within the toroidal confinement chamber, as shown in Figure 5. The curvature and nonuniformity of the toroidal field

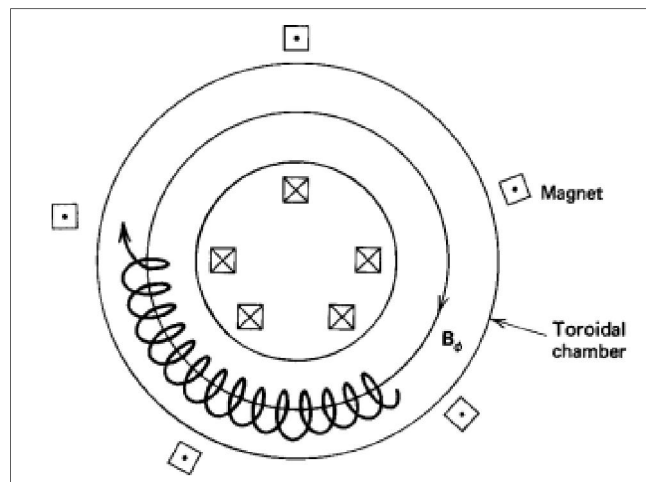


Figure 5 - Charged particle movement in a tokamak

produce forces which act upon the charged particles to produce drift motions that are radially outward. A poloidal magnetic field must be superimposed upon the toroidal magnetic field in order to compensate these drifts, resulting in a helical magnetic field, as shown in Figure 6.

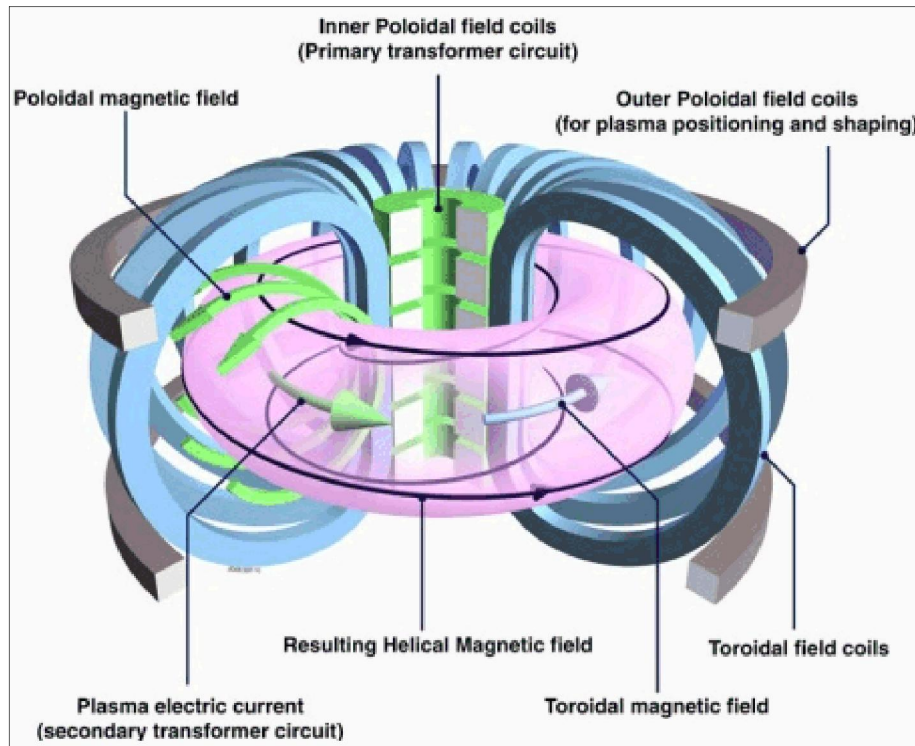


Figure 6 – Resulting Helical Magnetic field in a tokamak

1.4 - Stellarators

The term stellarator is used to describe that class of toroidal confinement devices that produce closed flux surfaces entirely by means of external magnets (in contrast to the tokamak, in which a current in the plasma produces the poloidal magnetic field). The stellarator confinement concept was one of the first to be investigated. However, the success of the closely related tokamak in the late 1960s drew attention away from stellarator research. More recently, in the 1990s, problems with the tokamak concept have led to renewed interest in the stellarator design, and a number of new devices have been built. Some important modern stellarator experiments are Wendelstein 7-X [4] (Figure 7), in Germany, and the Large Helical Device, in Japan.

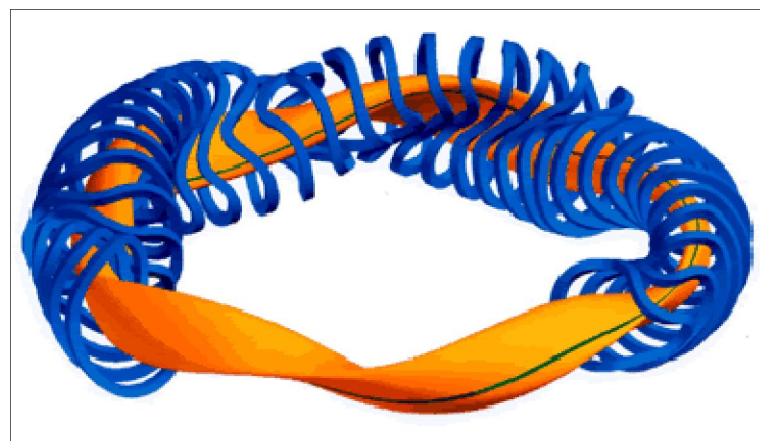


Figure 7 – Scheme of the magnetic coils and the plasma of Wendelstein 7-X

Comparing the stellarator and the tokamak, the stellarator has the advantage of operating in steady state and the disadvantage of the complexity of the design and construction of its magnetic field. The tokamak has the advantage that the current crosses the plasma be used for heating ohmic (Joule) and the disadvantage of operating in pulsed regime. But there are some tokamaks that are able to work with AC discharges, which allows to work with plasma for larger times, as it will be seen further in this work.

1.5 - JET

The Joint European Torus, located in Oxfordshire (UK), is the largest magnetic confinement plasma physics experiment worldwide currently in operation. It has the purpose to open the way to future nuclear fusion experimental reactors such as ITER and DEMO. The objectives of JET are to obtain and study a plasma in conditions and dimensions approaching those needed in a thermonuclear reactor. These studies will be aimed at defining the parameters, the size and the working conditions of a tokamak reactor.

JET has the world's record of energy produced by fusion: 16MW. For this it was used a neutral beam heating power of 22MW with an additional 3MW of ion cyclotron heating. The resulting fusion energy gain factor (Q) was equal to 0.6. The energy produced by fusion is calculated by the flux of neutrons that come from the plasma. The earliest plasma fusion experiments were in the pinch devices of the 1950s and the resulting Q value was around 10^{-12} .

1.6 - ITER

The International Thermonuclear Experimental Reactor) is an international nuclear fusion research and engineering project, which is currently building the world's largest and most advanced experimental tokamak nuclear fusion reactor. The tokamak will be located at the Cadarache facility in the south of France.

It has two fundamental objectives:

(i) Prove the scientific and technological viability of nuclear fusion through a gain factor of 10 to 20;

(ii) Test the operation in simultaneous of all technologies necessary for a safe and efficient operation of a reactor of nuclear fusion.

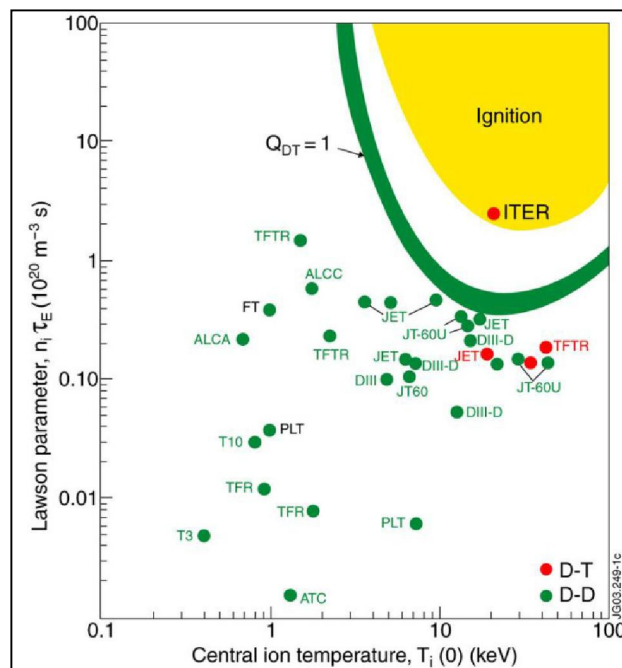


Figure 8 – Scheme summarizing the operation conditions of several tokamaks

1.7 - Tokamak – Heating systems

Ignition requires heating systems, below are the most common:

1.7.1 - Ohmic heating: With an electric field applied to the plasma a current is created and electrons are accelerated. It is due to the collisions between the electrons and the ions in which there is energy released as thermal energy (Joule effect).

1.7.2 - Neutral Beam Injection (NBI): It is the injection of highly energetic hydrogen or deuterium atoms into the plasma, where they become ions and give up their energy to the plasma ions and electrons via Coulomb scattering. The injected particles must be neutral in order to pass through the magnetic field surrounding the plasma.

1.7.3 - Radio frequency heating: It is the transfer of energy from an external source to the plasma by means of electromagnetic waves. When the electromagnetic wave propagates through a plasma the electric field of the wave accelerates the charged particles which then heat the plasma through collisions.

1.8 - Tokamak – Most common diagnostics

1.8.1 - Interferometry

Interferometry is a set of techniques in which electromagnetic waves are superimposed so as to be able to extract information about them. In Fusion investigation two electromagnetic signals are sent, one by the plasma and the other by vacuum, the two paths must have the same length. The electromagnetic wave that propagates in the plasma suffers an additional phase shift comparing with the one that sent over the same route in vacuum, and from the presented deviation of the two waves we can take information about the line-integrated density. Figure 9 shows a diagram of the electromagnetic wave passage by the plasma and a possible measured average plasma density through time.

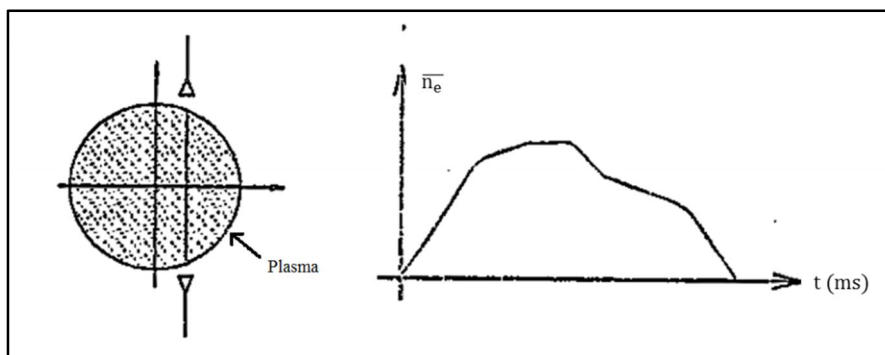


Figure 9 –Diagram of electromagnetic signal passing by the plasma (right) and at left it's possible average plasma density through time (left)

1.8.2 - Reflectometry

An alternative method for measuring the electron density is reflectometry. In this method microwave radiation with a certain frequency is launched into to the plasma along the density gradient and reflected at the layer where the electron density equals a critical value. The relative positions of the

different density layers in the electron density profile are determined by making the measurement with a range of different probing frequencies.

1.8.3 - Deflection analyzer of an ion beam

This diagnostic uses an ion beam that traverses the plasma. It is based on the fact that the charged particles moving in a magnetic field describe, in the plane perpendicular to the field, with circumferences with radius equal to:

$$r_L = \frac{v_{\perp} m}{e B} \quad (4)$$

The analysis of doubly ionized ions that are produced by collisions of the primary ion beam with electrons of the plasma, can be used to determine, using a numerical code, the density of plasma, the poloidal magnetic field and the plasma potential and the respective profiles and evolution over time.

1.8.4 - Magnetic measurements

In Fusion investigation several types of magnetic diagnostics are used, which in most of the cases are composed by magnetic sensors such as inductors or conductor loops. Some of the more simple examples of these devices are the Mirnov coils (fluctuations/instabilities) and the Rogowski coils (plasma current). These diagnostics are particularly indicated to analyze the magnetic properties existent on the proximity of the plasma column.

In these types of diagnostics occurs an electromotive force induced on the devices that is originated by the variation of magnetic flux that passes by them over time. It is necessary to integrate the receiving signal/data during the acquisition to get a voltage that is proportional to the flux/magnetic field being measured.

With Equation 6 we can know the flux Φ from the induced voltage V and by Equation (5) we calculate the magnetic field \vec{B} , where N is the number of loops, A is the average area and \vec{n} is the normal of the coil.

$$\Phi = - \int_{t_0}^t V(t') dt' \quad (5)$$

$$\vec{B} \cdot \vec{n} = \frac{\Phi}{NA} \quad (6)$$

In Rogowski coils to calculate the plasma current is then used the following formula $I(t) = \Phi / nA\mu_0$ (7), where $I(t)$ is the plasma current, Φ is the flux calculated by Equation (5), n is the turns per unit of length each of area A and μ_0 is the permeability of free space.

With Mirnov coils the induced electromotive force measured is in accordance with the equation: $\epsilon = -N \frac{d}{dt} (\int \vec{B} \cdot d\vec{A})$ (8), where N is the number of coils, \vec{B} the magnetic field that the plasma column generates plus the magnetic field produced by the tokamak's coils the and ϵ is the induced electromotive force.

The process of time integration has a problem, defined as the "integrator problem", caused by electronic noise and voltage offsets during acquisition of long periods of time (e.g. 1000 s). The

consecutive integration of noise will influence the integral that is being constructed by leading its value to have an additional undesired error drift.

On this thesis it is characterized several techniques and algorithms to have a clear signal of a magnetic diagnostic and it is described the performed tests and obtained results.

The used modules are galvanic isolated digital modules with signal chopper mode and a sampling at 2 MSPS (18-bit full resolution data). To perform this tests it was been done modifications on previously used Firmware in Verilog and drivers in C and the development of Software to assistance the operator, a text based user-friendly interface.

2 - State-of-the-Art of integrator modules related to magnetic measurements in Nuclear Fusion

The progress in the study of plasma confinement is so remarkable that the next generation device has a great potential to reach the ignition condition (with the ITER project).

Stable and steady-state operation is one of the most crucial issues for the development of a fusion reactor. In tokamaks, stable and steady-state operation is still a challenging subject which has not yet been solved. In order to reach these goals, diagnostics will be more important not only for measuring plasma parameters but also for precise plasma control. [2]

Presently there are a lot of efforts focused on achieving higher frequencies acquisitions as well very fast digital processing to promptly send the answers to the devices in order to have precise control and obtain data for studies.

To shorten the data processing time, Field Programmable Gate Array (FPGA) are usually utilized. Since there is no need to transfer the data to an external computer, the digital processing can be done in real time. [7]

The diagnostics developed for ITER produce approximately 5 Gigabits per second of data and make use of a million diagnostic channels. The planned acquisition boards allow use to digitize a few hundred Mega samples per second and will use protocols Aurora and PCI Express that can transport data at several Gigabits per second between modules.

In tokamaks the magnetic diagnostics provide essential information as the main electromagnetic parameters of the plasma (plasma current I_p and internal inductance l_i), the position or speed of the plasma current centroid and the shape of the plasma boundary. Information provided by magnetics is used in most machine control loops and by almost all other diagnostics. [6]

The magnetic diagnostics based on inductive sensors have many advantages in the harsh environment of fusion devices (high temperature, limited space, high-vacuum and radiation exposed (n , γ environment) [3]. Pickup coils and flux loops do not have complex designs, can be made of radiation hard materials, and can detect even the smallest field changes on the level of several tesla. [4]

In these types of diagnostics occurs an electromotive force induced on the devices that is originated by the variation of magnetic flux that passes by them over time. It is necessary to integrate the receiving signal/data during the acquisition to have the wanted signals and results. [4]

The process of time integration has a problem, defined as the “integrator problem”, caused by electronic noise and voltage offsets during acquisition of long periods of time (e.g. 1000 s). The consecutive integration of noise will influence the integral that is being constructed by leading its value to have an additional undesired error drift. At present, the developed integrators appear to be stable within $100 \mu\text{V}\cdot\text{s} / 1000\text{s}$. [4]

It was been done a lot of afford to isolate the noise from the signals after or during the acquisition. One of the factors that influence the electronic noise is the temperature [12], measuring it through the acquisition will allow the compensation of this factor in real time.

In today's tokamaks the integration of the incoming signals from magnetic diagnostics is done by devices that can be divided in analog integrators and digital integrators. The most common process are shown in Figure 10 and described in Table 2 [1].

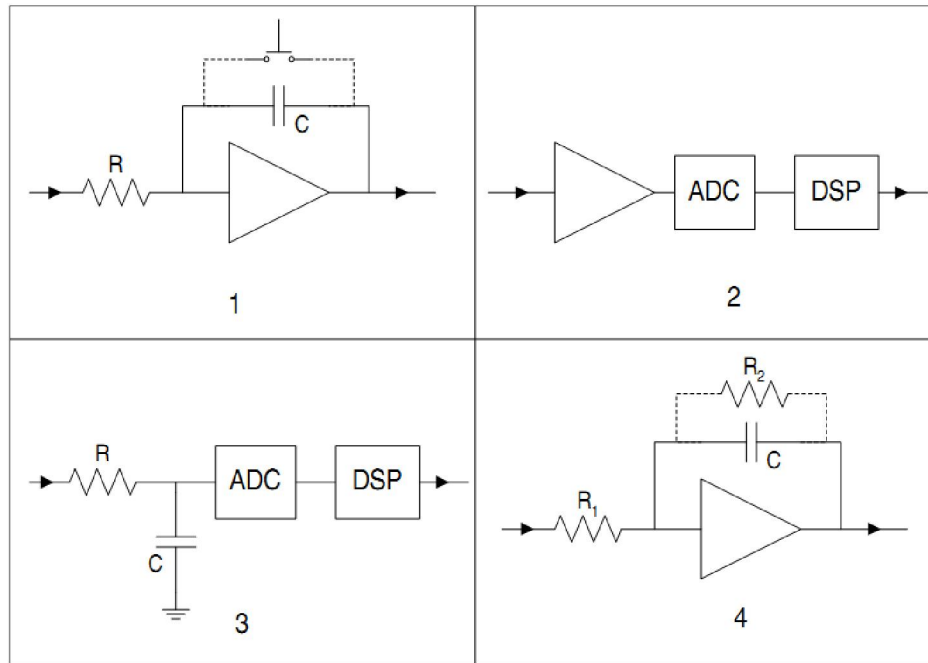


Figure 10 – Main circuits used for integration of analog signals [1]

Circuit number	Characteristics	Advantages	Disadvantages
1	Ideal active analogic integrator	Direct integration	Implies control logic controlled externally
2	Direct conversion of the signal and numerical integration	Digital precision	Dynamic range and bandwidth limited by the ADC
3	RC low-pass filter with numerical correction	Simplicity	Attenuation at high frequencies
4	Active analog integrator with level replacement base mesh and subsequent correction of the numerical integral	Stability	Amplification of input offset voltage by mesh R1 R2

Table 2 – Characteristics of several types of analog signals integrators, presented before in Figure 10 [1]

The major advantage of analog electronic signal integration comparing to digital integration is the continuous output signal, which can be used directly as a flux measure and no further signal processing is needed. The circuit of an analog integrator connected to a Pickup Coil is shown in detail at Figure 11.

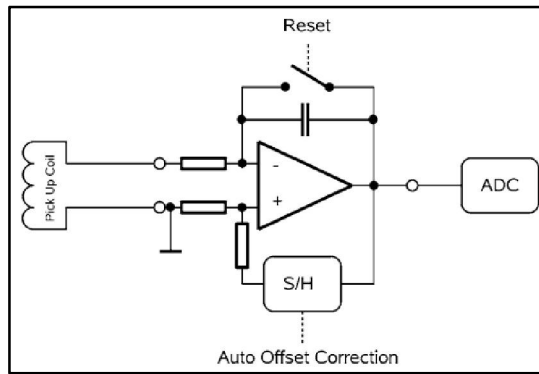


Figure 11 - Circuit of an analog integrator with sample and hold circuit for automatic offset correction [4]

The analog integrator has its output range limited by its power supply (it can become saturated in the case of a high flux variation such as a disruption); it has a low dynamic range output comparing to the one of digital integration, which is determined by the input saturation level, the signal rise time, and the sample rate.

Analog integrators have other intrinsic problems as the integrator drift, due to the offsets of the operational integrator which introduces an absolute error that increases with integration time. In numerical integrators the digitized induction signal has to be integrated and corrected for offsets in time using digital signal processing, which uses algorithms that have major advantages with respect to offset corrections compared with sample and hold circuits when the input signal is noisy. [3] [4]

A simple schematic of a numerical integrator is shown in Figure 12. One of the principles of this integrator is to modulate the induction signal as early in the signal path as possible in order to avoid the vulnerability by any additional offset and error voltages.

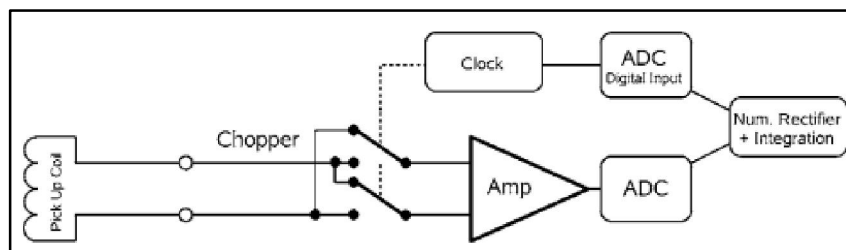


Figure 12 - Principle of the chopper integrator [4]

The chopper, which is driven by a clock, switches the terminals of the incoming signals in a way that the integrator gets rid of the temperature dependence of the junctions and semiconductor characteristic.

A digital–analog integrator was developed for use with inductive magnetic sensors in long-pulse tokamaks as in the ITER project. The continuous compensation of input offsets is accomplished by

alternating analog-to-digital convertor samples from the sensor and a dummy load, while a RC network provides passive integration between samples (the schematic of this integrator is shown in Figure 13). [5]

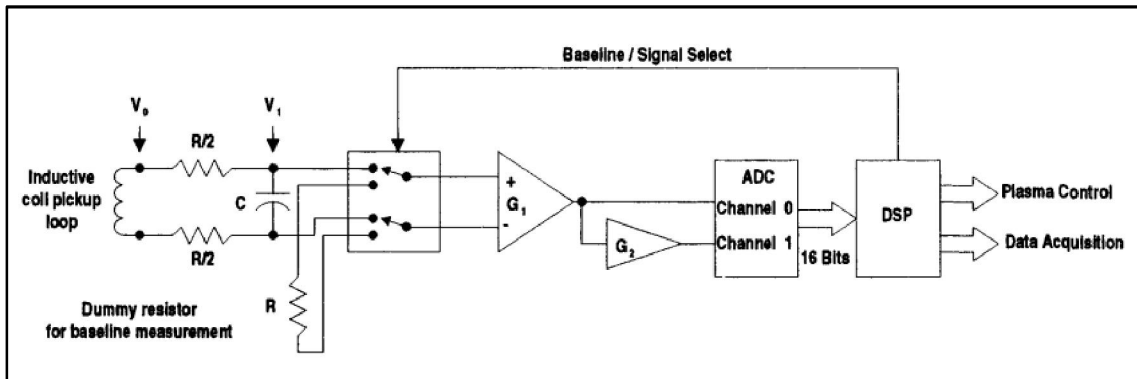


Figure 13 - Block diagram of digital-analog long-pulse integrator

In bench tests a drift error of 1 mV s was obtained at the end of a 1200 s integration period.

On this thesis one of the presented results is the drift obtained from acquisitions that lasted 1000s with the input short-circuited and constant temperature, it was achieved a maximum drift of 25 uV×s.

3 – Data Processing System

3.1 – Introduction

Control and data acquisition systems are the set of the hardware, firmware and software that enables to do measurements and control processes, they are fundamental for the operation of fusion devices. Control in nuclear fusion research usually refers for the coordinated operation and efficiency of all the components of the experiment, while data acquisition is all instruments and processes that enables the measurements of any useful physical quantity (currents, voltages, power, ...).

On this chapter is presented the main characteristics of the used Data Acquisition System and the necessary techniques and developed architectures for this work. On the first section of the chapter is described briefly the Control and Data Acquisition of ISTTOK, afterwards the used Hardware and then the developed Firmware, Software and algorithms to clear the signals.

3.2 – Data Processing System of ISTTOK

ISTTOK's control and data acquisition system was projected in a distributed, modular, multivendor, integrated and transparent philosophy. [13] [1]

Almost all of the hardware of control and acquisition related to ISTTOK, composed by signal-conditioning circuits, data acquisition boards (ADC), timing and generation of waveforms (DACs) was designed and built in IPFN using the VMEbus bus standard, but nowadays it has been gradually moved to ATCA.

To perform this work it was been done modifications on previous used Firmware written in Verilog, Linux device drivers in C and the development of a Software to assistance the operator, a text based user-friendly interface.

The used modules are galvanic isolated digital modules developed by IPFN with signal chopper mode and a sampling at 2 MSPS (18-bit full precision data). It can be seen in Figure 14 one of the used modules, the schematic is in the appendices. The crate used for the acquisitions, an ATCA crate, can be seen in Figure 15.

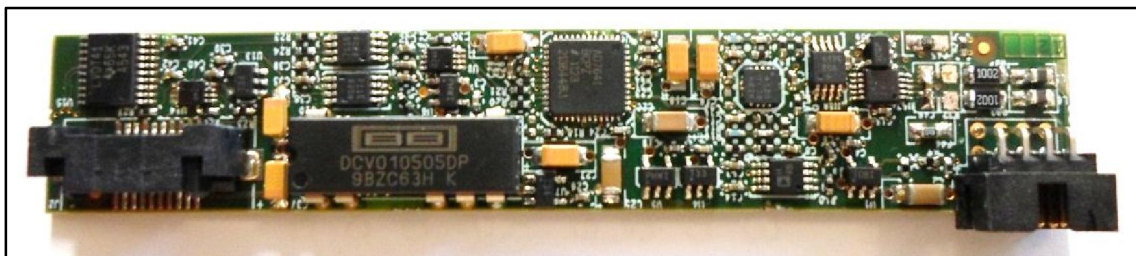


Figure 14 - ADC module used



Figure 15 – Used ATCA crate with the ADC modules inserted

3.2.1 - ATCA

Nowadays control and data acquisition on fusion experiments are performed by computerized systems, distributed and modular that sometimes uses more than one computer busses. Computer bus have the fundamental function to allow the connection between the conversion modules analog to digital and digital to analog, the signal conditioning electronics and the processors, by another words is the set of hardware, firmware and software that permits connect digital instrumentation to a computer.

Until recently, telecommunications vendors have successfully developed and deployed many generations of equipment based upon proprietary system platforms. Vendors accepted the additional R&D costs and increased time-to-market associated with proprietary hardware because these proprietary platforms enabled vendors to differentiate and compete at a hardware level. However, modern networks are increasingly powered by software and their value is more and more defined by the rich layers of complex software-based applications and services that are supported by the network elements. In addition, each new wave of networking innovation challenges vendors to produce new system platforms with more sophisticated enabling technologies, more flexible support of multiple protocols, and more capacity to meet the increasing traffic demands of new services – and to deliver all this much more quickly and more cost-effectively.

The benefits of open standardization are already well accepted in other industries: lower individual research and development (R&D) costs as the total costs are shared over a wider community; shorter time-to-market; increased competition among component suppliers leading to greater innovation and downward pressure on pricing; and acceleration of the adoption of new best-in-class technologies. One such open platform is ATCA.

The ATCA is a series of specifications for an open, standards-based system platform for building high-capacity, high-performance and high-availability Network Equipment-Building System (NEBS) compliant telecom shelves. It supports the integration of plug-and-play smart I/O blades with processing server blades in a single chassis, all interconnected using standard switch fabrics. It was developed by the PCI Industrial Computer Manufacturers Group (PICMG).



Figure 16 – ATCA crate

The basic elements of the platform are illustrated in the figure below (Figure 17):

Front Boards - containing the desired electronic functions and the connectors required to interface with these functions. On the Front Board, three connector zones are defined: Zone 1 for power connection and Shelf management, Zone 2 for Data Transport Interface, and Zone 3 for user-defined IO (Input/Output) interconnect;

RTMs - providing user defined input and output connectivity to the companion Front Board from the rear;

Backplane - providing connector interfaces for power distribution and input/output connectivity between Front Boards, as well as final mechanical alignment and support;

Subrack - providing attachment points for the Backplane, as well as alignment, support, and mechanical engagement for the insertion and extraction of Front Boards and RTMs;

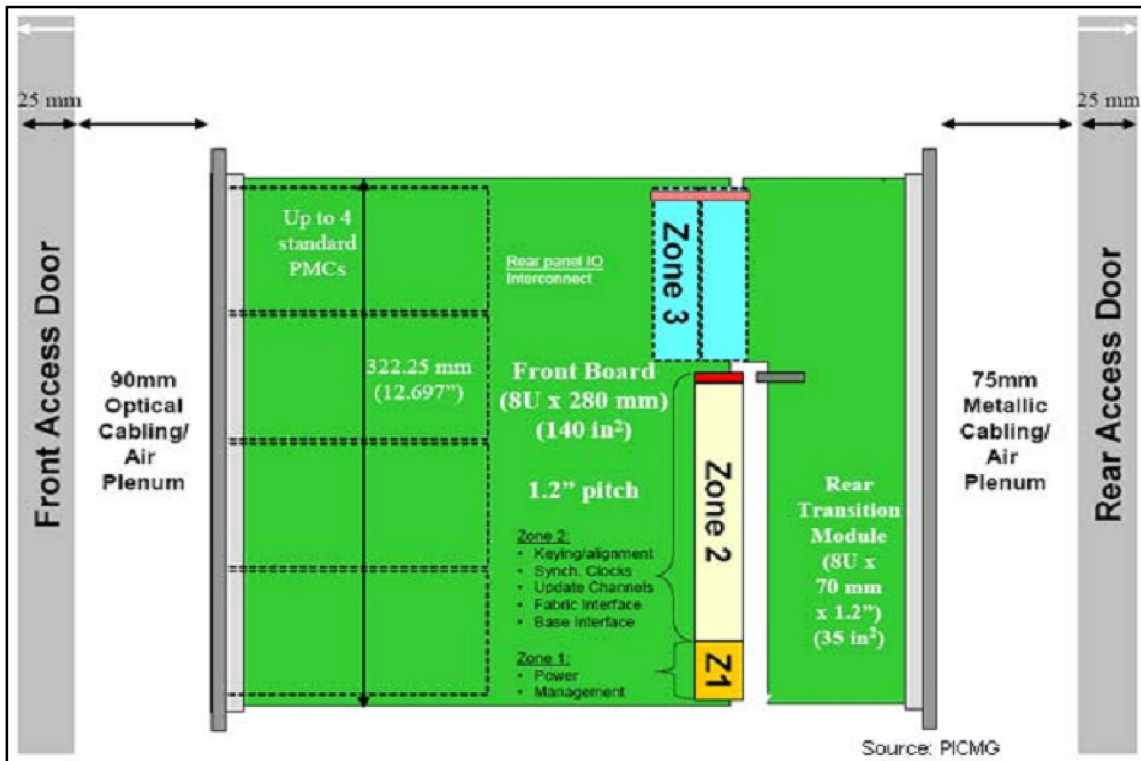


Figure 17 – ATCA board scheme

3.2.2 - FPGA

FPGA stands for Field Programmable Gate Array and, as the name suggests, it can be described as an integrated circuit in which can program any digital function. The FPGAs contain programmable logic components called Logic Blocks and a hierarchy of reconfigurable connections allowing the logic elements to be physically connected, having the desirable function in digital logic. The used FPGA can be seen in Figure 18.

To program the FPGAs is used a HDL (Hardware Description Language) such as VHDL or Verilog. The Firmware developed in this thesis was written in Verilog.



Figure 18 – Image of a FPGA

3.2.3 – Real Time Operating System tuning

3.2.3.1 – Linux Kernel

The Operating System Kernel is a computer program that, among other, manages the requests (input or output) from software into data processing instructions for the CPU and other hardware parts of the PC (It is fundamental in any OS). With the aid of the firmware and device drivers, the kernel provides the most basic level of control over all of the computer's hardware devices (diagram at Figure 19).

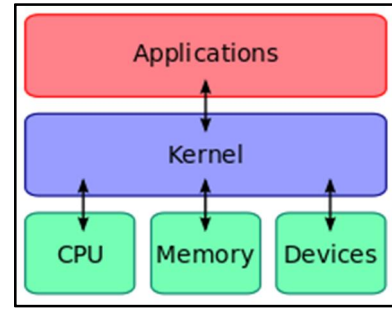


Figure 19 – Simplified diagram of Kernel's interactions

The Linux kernel allows a programmer to write device drivers for the system which may be an enormous advantage for the performance of certain program tasks or even enabling the execution of new processes not before planned.

The Linux kernel also permits within certain limits the manipulation of parameters of subsystems (as Virtual Memory that will be explained a few paragraphs bellow, section 3.1.4.3). This may as well optimize the performance of program tasks.

3.2.3.2 - Real-Time

Real-Time is an expression used to refer to systems in which the execution of a process/task would be guaranteed within the needed strict time. To meet these operational deadlines, programmers use real-time operating systems (RTOS) on which the maximum response time can be calculated or measured reliably for the given application and environment.

3.2.3.2.1 - RT priority

A typical RTOS uses priorities and the highest priority task wanting the CPU always gets the CPU within a fixed amount of time after the event waking the task has taken place. On such an RTOS the latency of a task only depends on the tasks running at equal or higher priorities, all other tasks can be ignored. On a normal OS (such as normal Linux) the latencies depend on everything running on the system, which of course makes it much harder to be convinced that the deadlines will be met every time on a reasonably complicated system. This is because preemption can be switched off for an unknown amount of time. The high priority task wanting to run can thus be delayed for an unknown amount of time by low priority tasks running with preemption switched off.

The used PC has Linux based OS, with Red Hat version x Linux. Linux version 2.6.33.9-rt31.74.el6rt.x86_64. The used RTOS was RT_PREEMPT with the MRG extensions [24].

3.2.3.2.2 - Core affinity

This was accomplished by starting isolating by the grub utility [21] of the OS one or more of the four cores. With a script it was possible to indicate a task to the core that was isolated, in this case the task was related to the processing and save the incoming data in the PC. In the Software it was used special libraries to specify the affinity of the CPU.

A Linux tool called “Tuna” [20] was also used initially to adjust scheduler tunables as CPU affinity and RT priority.

3.2.3.2.3 - Virtual Memory

The Virtual Memory is a system that combines physical memory along with some secondary storage device to give the appearance that a computer system has more physical memory than is actually installed. A virtual memory system tries to efficiently allocate physical memory (RAM) among many competing demands, including: kernel code, kernel global data, dynamically allocated kernel memory, kernel caches (buffer, page, swap, and slab), application code, application stack space, static application memory, and application heap.

Another action was needed to have a Real-Time System was the manipulation of certain parameters from Virtual Memory.

The parameters of VM can be seen in `/proc/sys/vm`

As the data ultimately intended for disk is written, Linux caches this information in an area of memory called the page cache. Linux usually writes data out of the page cache using a system call called `pdflush`. There are tunables for adjusting the minimum and maximum number of `pdflush` processes.

`/proc/sys/vm/dirty_background_ratio` (default 10) is the maximum percentage of active that can be filled with dirty pages before `pdflush` begins to write them. Primary tunable to adjust, most of the cases downward. The goal is to reduce the amount of data Linux keeps cached in memory, so that it writes it more consistently to the disk rather than in a batch. This parameter was set to 0.

`/proc/sys/vm/dirty_ratio` (default 40) is the maximum percentage of total memory that can be filled with dirty pages before processes are forced to write dirty buffers themselves during their time slice instead of being allowed to do more writes. This parameter was set to 1.

After isolating a core for the task related to the acquisition, set interrupts priorities and manipulation of parameters from Virtual Memory the system became a real-time system and there was not more loss of data.

Without Real-Time the amount of data that could be saved to disk without data lost would be $7 * 2 \text{MSPS} * 32 \text{bits/s} / 100$ or 5.34MB/s with the system with Real-Time the amount of data was 61.04MB/s.

3.2.5 – Numerical integrators

As it was mentioned in the introduction several types of magnetic diagnostics are used in nuclear fusion, the needed integrators for these diagnostics can be divided into two groups, analogic integrators and digital integrators. This thesis is about a new digital (or numerical) integrator shown already in Figure 14.

It can be seen at Figure 21 the electrical schematic of the used module related to the chopper. The signals from the clock and/or the signal from the chopper are recorded, so that the final obtained value is the integral, resulted from the sum of the constant incoming values.

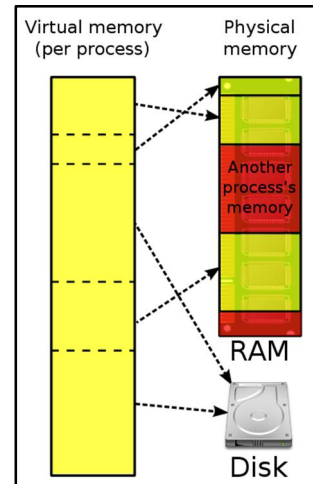


Figure 20 – Virtual Memory – VM combines active RAM and inactive memory to form a large range of contiguous addresses

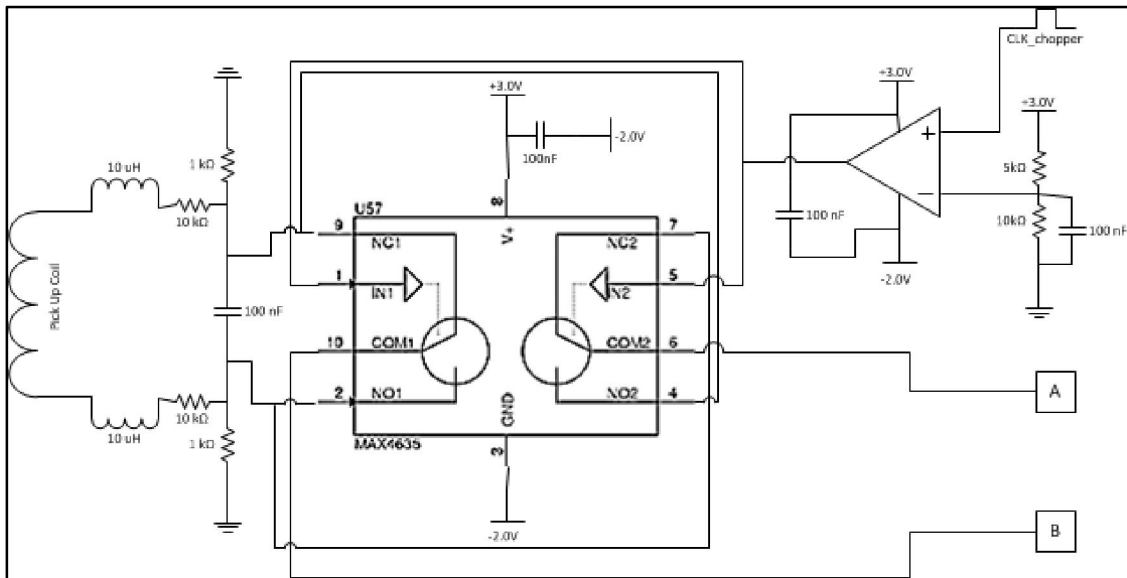


Figure 21 – Schematic of the digital chopper integrator and the filters and amplifier system before the ADC

In Figure 21 is seen that the signal coming from the Pick Up Coil first goes through a low-pass filter of second order, with the presented values the cut-off frequency is at 1kHz. A previous version this ADC module had at this filter a capacitor of 100pF (and not 100nF as it is presented), the cut-off frequency was at 1MHz. In Figure 22 is shown the rest of the implemented circuit before the signal goes to the ADC, it can be summarized as being a necessary anti-aliasing treatment with a low-pass filter of first order.

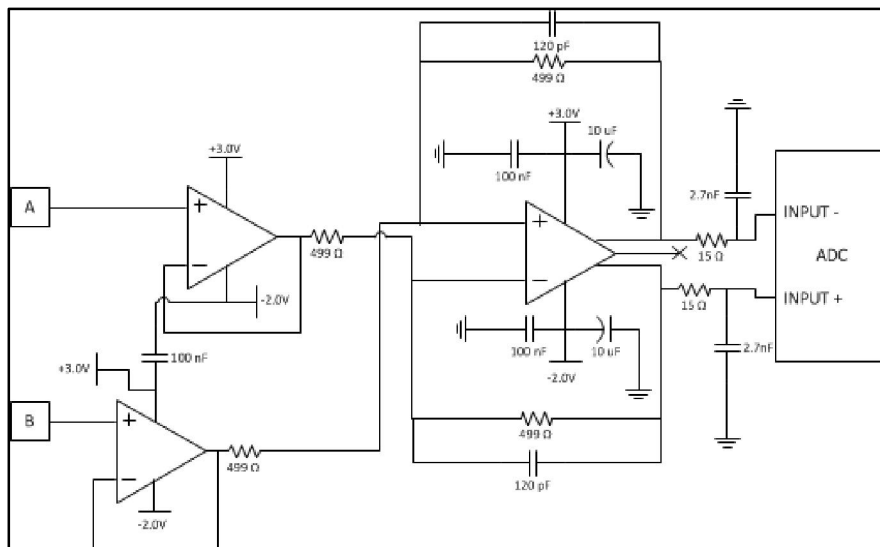


Figure 22 - Schematic of the digital chopper integrator and the filters and amplifier system before the ADC

The measured effective number of bits (ENOB) of this module was 15,7 bits with a decimation of 100 of the samples by the firmware. Acquiring all data in raw mode at 2MSPS the ENOB will decrease to about 12,7 bits.

3.3 - Data Processing – Used Software and Firmware

3.3.1 - Data Processing on the FPGA

On the figure below is shown the block diagram of the first used FPGA logic architecture, this architecture was used as basis for other architectures developed during the tests for this thesis. The other architectures will be shown on the next section.

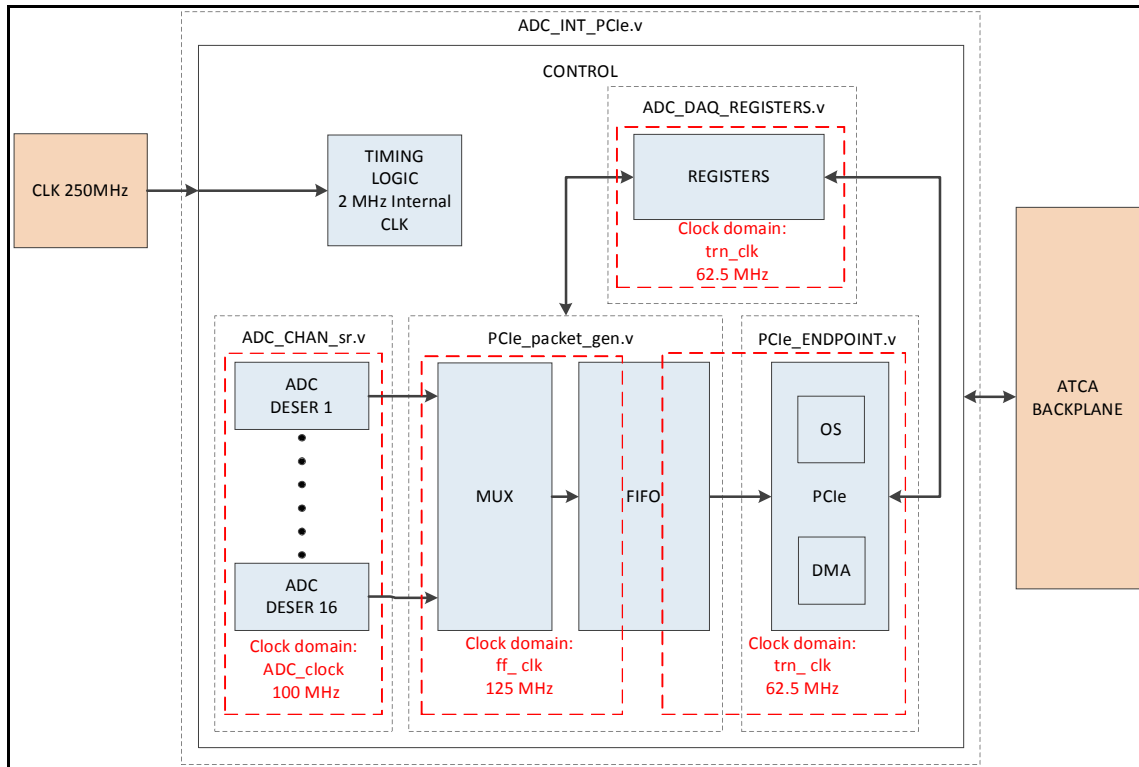


Figure 23 - Simplified block diagram of the first used architecture

The data of the ADCs (2 MSPS) is deserialized, passes by a Multiplexer to a FIFO buffer and then a PCIe packet is build and sent, in real time, by DMA, to the host memory. The packet payload comprises a 32 bits word time counter, 16 words of 32 bits with the ADCs data and a 32 bits word with status information.

DMA stands for Direct Memory Access and it is a feature of modern computers that allows some hardware subsystems in the computer to access the memory without using the CPU.

In this first architecture the 2 MHz sampling clock is generated from a 250MHz oscillator implemented on the board. The software trigger resets the time counter.

The developed software in C uses special drivers called input/output controls (IOCTLs) to set flags and parameters in the FPGA's registers such as for example the Chopping frequency.

3.3.2 - Data Processing Algorithm

There are two corrections needed to be done during or after the acquisition to compensate the “Electronics Offset” (EO) and the “Wiring Offset” (WO), as it can be seen in Figure 24. The EO after being calculated is sent to the FPGA registers to be subtracted from the incoming data of the board in real-time. The calculation of this Offset can be done by acquiring raw data values of the signal and do an average. These values are characteristic of the modules and the acquisition board.

The WO is an increment done constantly on the integration at each cycle during the acquisition that is not compensated by the EO Offset correction algorithm done before. It is estimated by doing the integral of the signal for some time. The correction of the WO Drift is then performed by the Software.

The procedure starts with the initial average calculation during a few seconds (defined by the operator) of the EO (up to one LSB precision) with the modules inputs short-circuited. The EO is the “After Chop” Offset and after being calculated it is stored in FPGA registers and accordingly subtracted from the incoming data of the board in real-time, in order to minimize its effect on the acquired data.

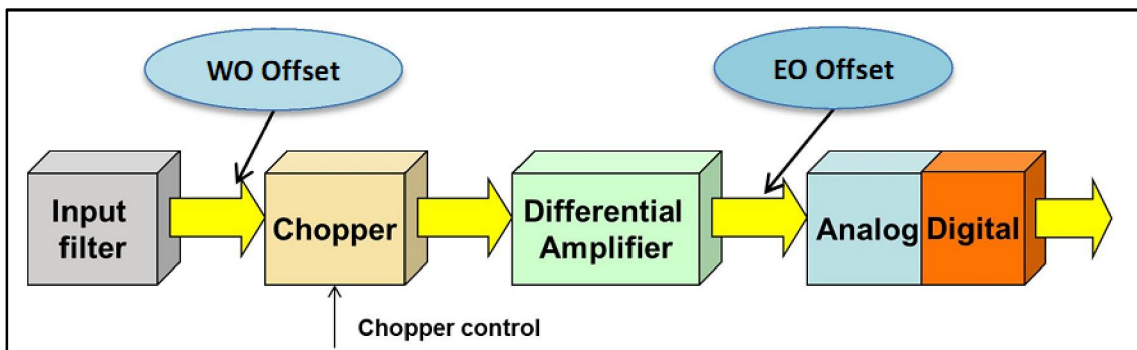


Figure 24 - Schematic of the influence of EO and WO

After the calculation of the EO the acquisition starts, the data is saved on disk.

There is a second correction that is needed to be done. It is due to the WO which is designed also as the “Before Chop” Offset. This increment is very small in comparison to the EO, in absolute term, but unfortunately cannot be eliminated by the phase modulation technique.

The integral is done normally, and after a certain time it is analyzed and determined the increment done at each cycle. The WO can be calculated at the first few seconds defined by the operator (Pre-compensated) or at the end of the acquisition (Post-compensated).

The “WO” average drift contribution is subtracted for each DMA packet (in software). The integral is made having in consideration the increment that was done by subtracting it during the integration. The used Software algorithm use during the acquisition is demonstrated in Figure 25.

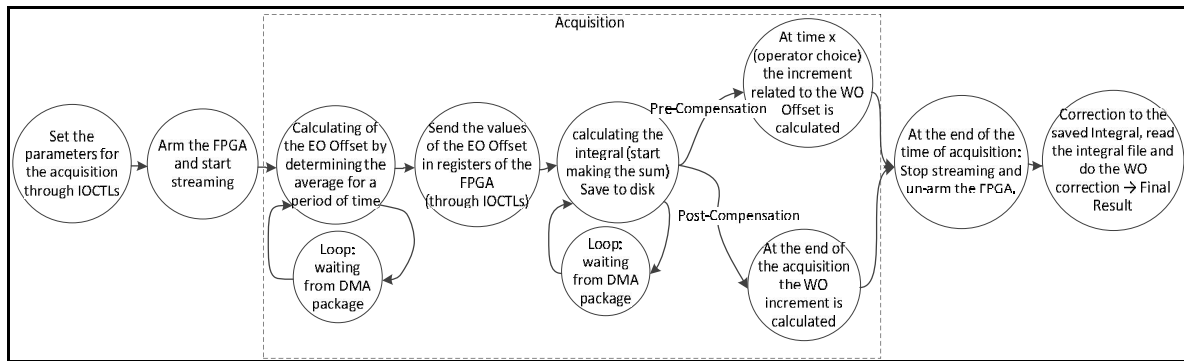


Figure 25- Used Software algorithm to make the acquisition

During acquisition of long periods of time (e.g. 1000 s) the current used RAMs do not have enough space to keep all data (almost 8 GB of data from each channel). It is need to gradually save the data on disk. This process of constantly writing data, described on the Software, can delay the process of the drives getting the data in such way that information is lost during the acquisition. The lost data are counted during the process by two parameters:” loss_hits” and “max_buff”_count. “max_buff”_count is the number of times the driver IRQ (interrupt request) handler was called while there was still one or more buffers waiting to be read, this number should not be higher than 16 (which is the number of DMA buffers defined in the drivers). While “loss_hits” is a counter that does the accumulation of all missed interrupts, not as important as the number represented by “max_buff”_count. The maximum data transfer without losses was 61.04MB/s, 8 channels at 2MSPS, and each sample with 32bits, with the Hardware used.

3.4 - Architectures

3.4.1 - First Project

The procedure though a Short-Circuit Input acquisition starts with the initial average calculation during 10 s of the “EO” Offset (up to one LSB precision). The “WO” drift is calculated at the first 100s (Pre-compensated) or at the end of the acquisition (Post-compensated). Not all the data during this first project were being stored in Hard Disk File, the data was down sampled to 1:100 to be saved. The block diagram of the used architecture is shown below (Figure 26).

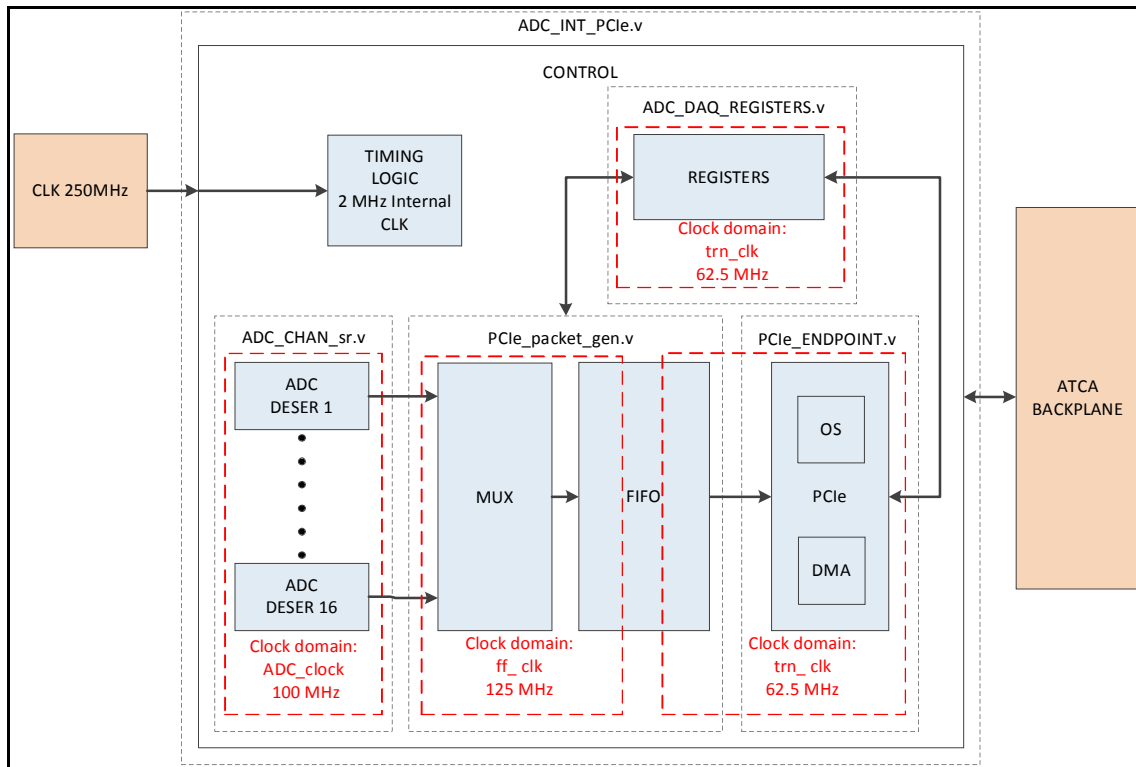


Figure 26 - Simplified block diagram of the first used architecture (the dashed box is to separate the clock domain)

One of the results presented is the drift obtain from acquisitions that lasted 1000 s with the input short-circuited and constant temperature. With a post-compensated analysis (after the total acquisition the final valor is set to zero) it was obtain a maximum drift extension of 25 uV×s. With a pre-compensated analysis of 100 seconds (the parameter to adjust the incoming data is calculated after 100s) it was obtain a maximum of 50 uV×s after 900 seconds of sampling.

During the tests in some acquisition the temperature of the modules were changed, by carefully heating the module with a hot air gun until temperatures of ~43°C. The heating of the modules was monitored by a thermocouple attached to one module. The electronic noise was influenced by the changes of temperature that were induced. The final integration of a pre-compensated acquisition from several modules suggests that there is a relation between the temperature and the noise that can be predictable, making possible real time corrections on the integration based on temperature sampling.

On the final part of the next chapter it was included a few test that were made to test the reconstruction of certain signals, such as constant signals and sine shaped signals and its integration. By the results obtained it is showed that on the transition of chop it is lost ignored only two samples.

3.4.2 – Firmware Architectures developed to ISTTOK

It was used the same ATCA crate on ISTTOK’s laboratory room but now with 12 ADC modules to acquire the signals coming from 12 Mirnov coils at 2 MSPS during the discharges, with the objective to integrate the new control system of AC discharges on ISTTOK. [17]

For ISTTOK different architectures were used:

First Architecture: The integration was made on the Software, the EO of each channel was calculated by the Software then sent to the Firmware and the WO was calculated after the acquisition or at the beginning (depending if it was post-compensated or pre-compensated integral, respectively). The firmware was the first that was presented;

Second Architecture: The integration was made on the FPGA, the parameters EO and WO were sent by the Software at the beginning of the acquisition. (They had been previously calculated or calculated with the data of the first moments of the acquisition);

The block diagram of the last architecture can be seen in the Figure 27.

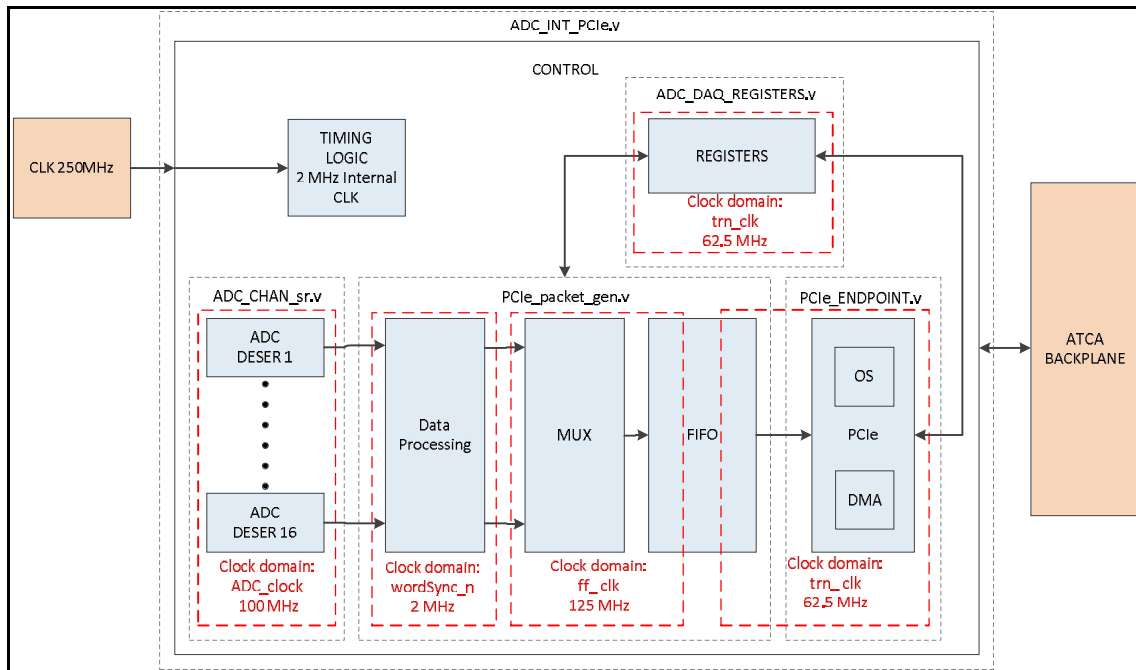


Figure 27 – Simplified block diagram of the FPGA architecture

During the tests at ISTTOK two different plasmas were acquired, pulsed plasmas and AC plasmas. An Alternate Current (AC) plasma discharge results of the change of the field allowing the plasma to travel front and backwards several times. The ISTTOK tokamak has a long tradition on Alternate plasma Current (AC) discharges, a recent paper presented the ISTTOK control system and the optimizations that extended the AC current discharges duration to more than 1 s, corresponding to 40 semi-cycles without apparent degradation of the plasma parameters. [14]

3.3.3 - Architecture developed for IPP

The objective was to demonstrate the performance of the ADC digital modules developed by the Instituto de Plasmas e Fusão Nuclear (IPFN) through tests in the Max-Planck-Institut für Plasmaphysik (IPP) at Greifswald, Germany. Some photographs taken during the tests can be seen at Figure 28. The performance of the modules and obtained results were as expected [18]. These modules might be used in W7-X, the new Stellarater being developed in IPP, creating a new protocol between IPFN and IPP.



Figure 28 – Photographs taken during the tests at IPP, Greifswald. At right is the author programming on-site the parameters for the acquisition and at left is his supervisor

Several tests were made as the integration of electronic noise and long acquisitions of 1000s of different signals from generators and from made assemblies. An assembly that was done in Germany had the purpose to simulate as real as possible the signals that would come from fusion devices. The main difference of this architecture comparing to the first used is the time logic that was changed and the use of an uTDC board made by IPP as it can be seen in the figures below (Figure 29 and Figure 30).

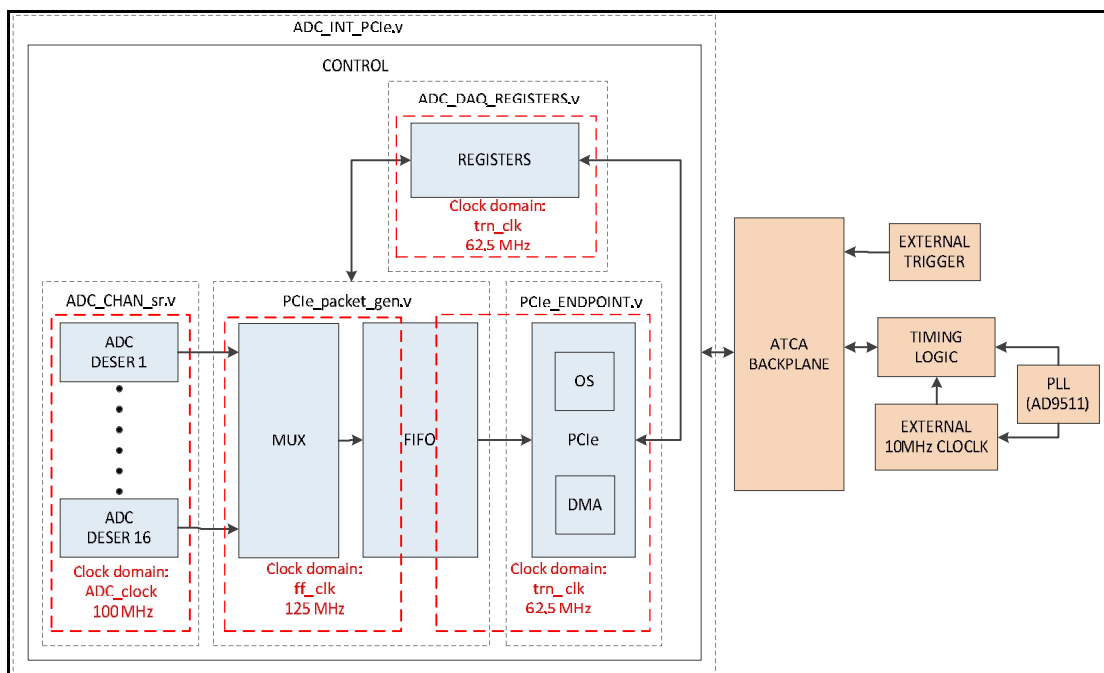


Figure 29 - Simplified block diagram of the FPGA architecture developed for the IPP

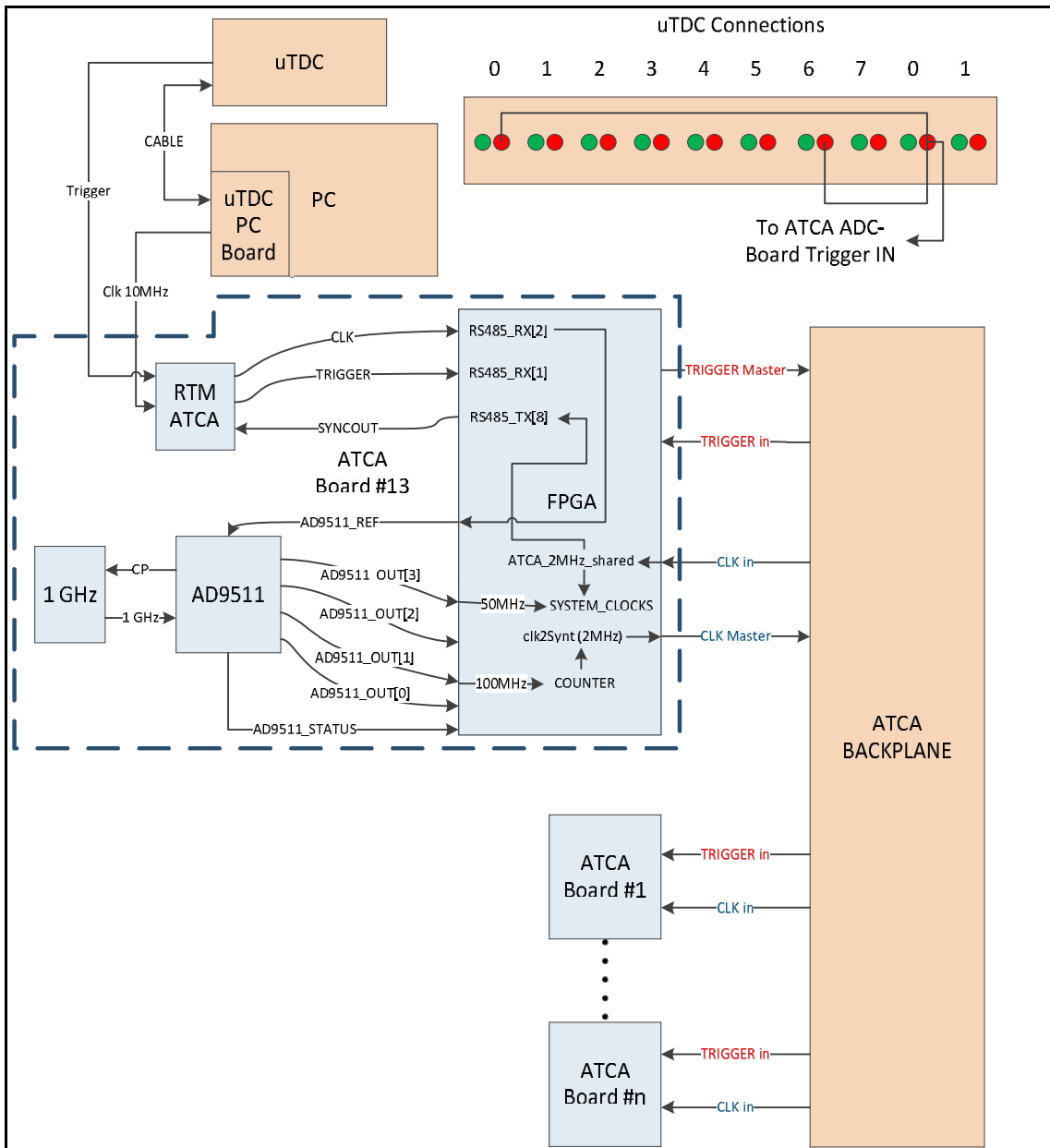


Figure 30- Simplified block diagram of the used connections related to the clock system

It is demonstrated, at the figure above, the uTDC [22] connections needed and the connections between the ATCA BACKPLANE and the boards, the clock and the trigger and sent by the master board to all the other boards to be all synchronous. The mentioned chip on the ATCA carrier designed by AD96511 is a programmable PLL (Phase-locked loop).

Some of the tests done with this architecture in Greifswald, Germany were similar to the ones made in Portugal. A few new tests were made with made assemblies using coils, a generator and a capacitor, the schematic an used assembly in shown in the figure above. The improvised coil had 20 loops of copper and a resistance of $\sim 0.12 \Omega$ and the implemented capacitor was of 33mF (the time constant would be about 4 ms) as shown in Figure 31.

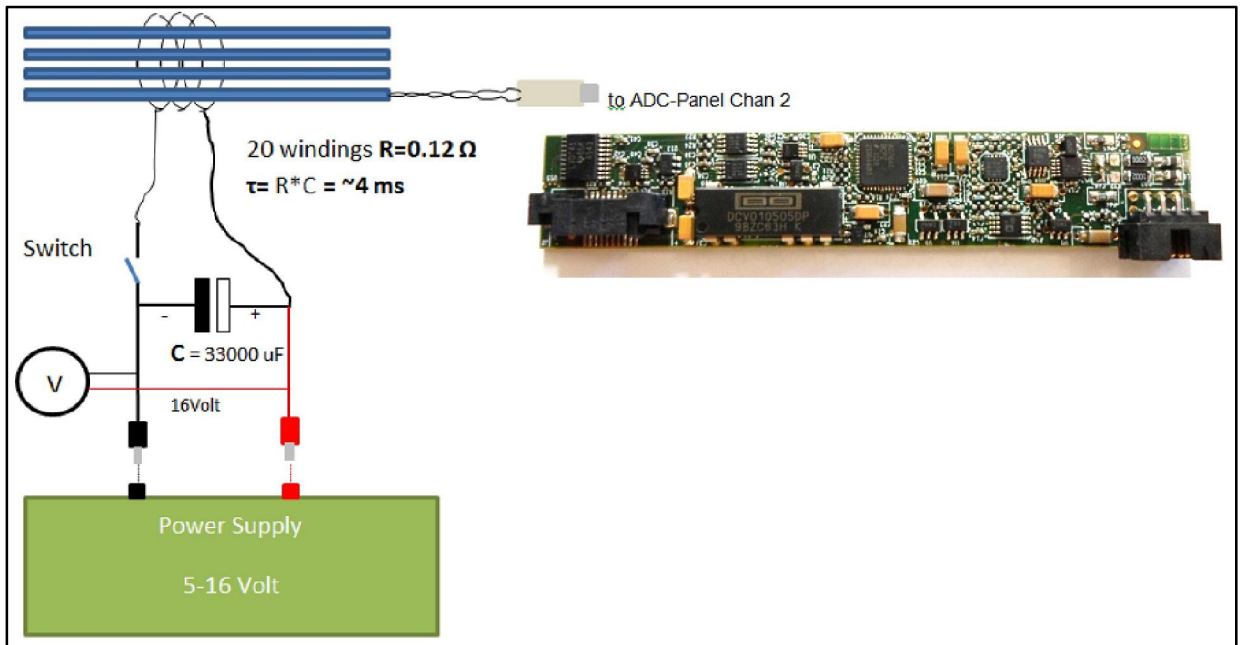


Figure 31 - Electrical setup for testing the Integrators with a W7-Stelarator magnetic probe

4 - Experimental Development

4.1 – Introduction

On this chapter is presented the tests and experiments made during this thesis. At first is shown with simple signals acquisition its chop reconstruction and integration. Afterwards is explored the “integrator problem” by making noise acquisition and integration, showing the drifts average values, the influence of the temperature on the integral. The obtained results with the temperature changes on the integral suggest that this factor could be compensated in real time (during the acquisition). Acquisitions and integration of signals from IST’s tokamak (ISTTOK) Mirnov Coils are then shown and this chapter finishes with tests performed for the IPP to demonstrate the performance of the developed modules.

4.2 - Signal Reconstruction

A few tests were done using the first developed Firmware (shown in section 3.3.1), they are related to acquisition and reconstruction of simple signals such as constant voltage signals and sinusoidal signals coming from generators.

4.2.1 - Signal Reconstruction of a constant voltage

At the terminals of the digital ADC module it was set a difference of 19.12V with two 9V 6LR61 alkaline batteries. The acquisition frequency is of 2 MHz and the chopper frequency is of 1.95 kHz. The raw data was saved together with the data from each channel it was also saved the chopper phase signal, so that the signal could be reconstruct afterward (Figure 32). The program used to manage the data was written in MATLAB.

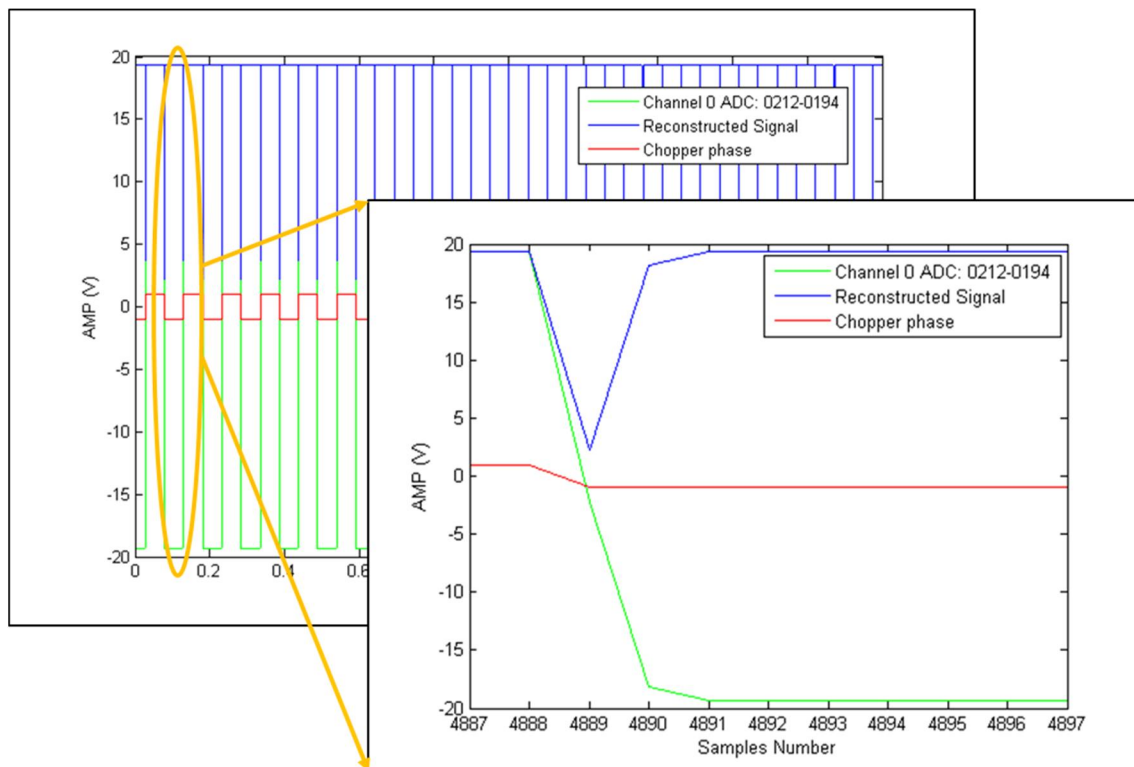


Figure 32 - Reconstruction of a constant voltage signal (right) and the reconstruction of a constant voltage signal during a transition of the Chopper in detail (left)

By this reconstruction only two samples are to be ignored, as it can be seen in the Figure 32, which shows the remarkably fast behavior of the ADC module design.

4.2.2 - Reconstruction of a pure sine signal

First the ADC input terminals were shorted to determinate both Offsets (EO and WO). Then a signal from a generator with a sine form, amplitude of 18V and a frequency of 200Hz was set to the ADC terminals, the results can be seen below in Figure 33.

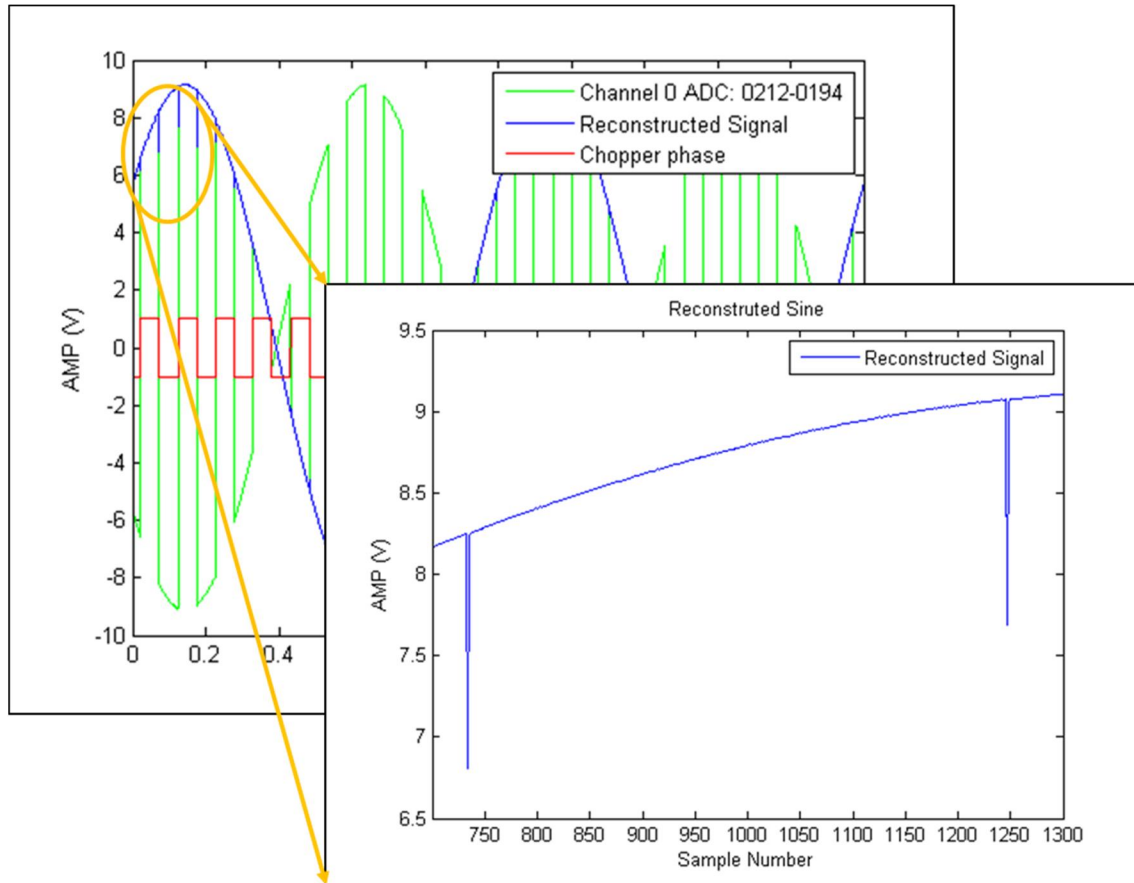


Figure 33 - Reconstruction of a sine shaped signal (top), reconstruction of a sine shaped signal in detailed (below)

4.2.3 – Long acquisition of a sine signal and numerical integration

To see if loss of data was occurring a long acquisition was made of a sine signal coming from a generator with the same properties as the ones listed on the section above (4.2.2). The results are shown below.

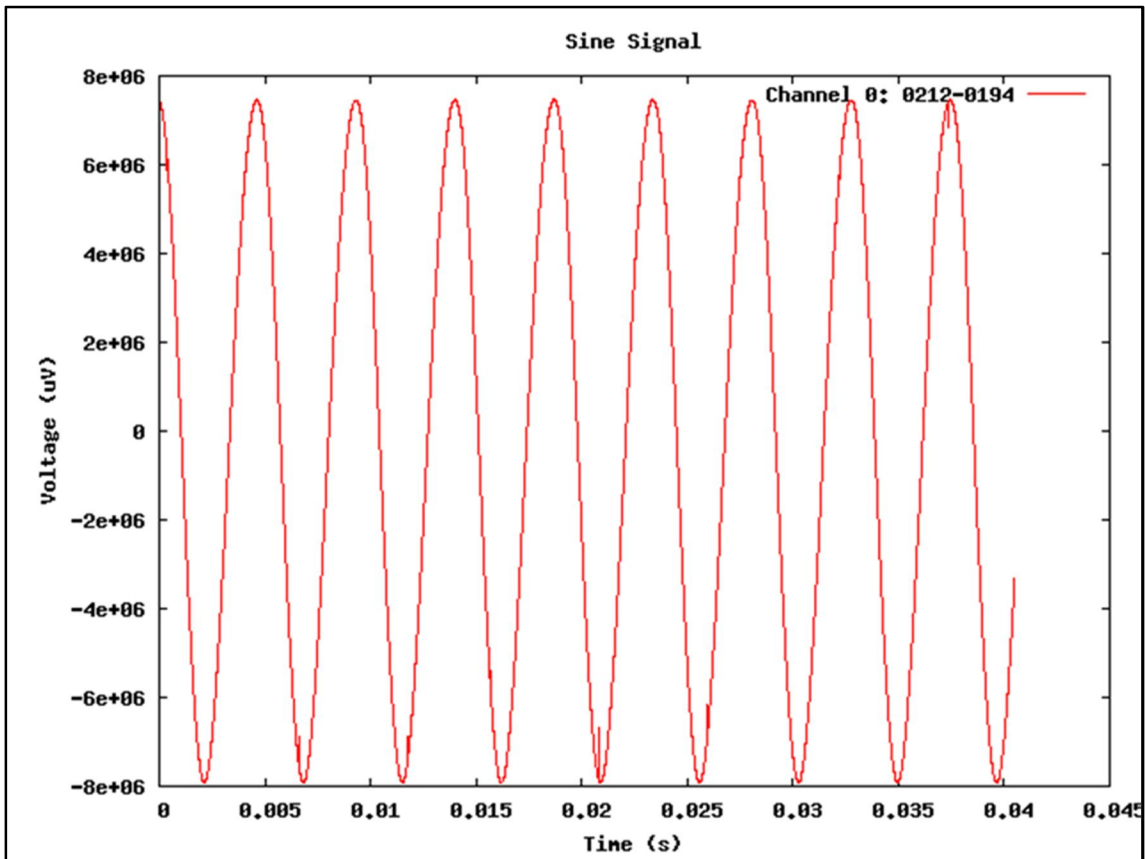


Figure 34 – Detail of Offset of Sine signal

It can be seen, in the detailed images, that the integral of the sine signal (Figure 35) is has a certain phase shift ($\pi/2$) comparing to the sine signal (Figure 34), as it is expected. A couple of results of this acquisition are shown in the appendices, Figure 83 and Figure 84. By the integral is seen that no data is lost, Figure 35 and Figure 83.

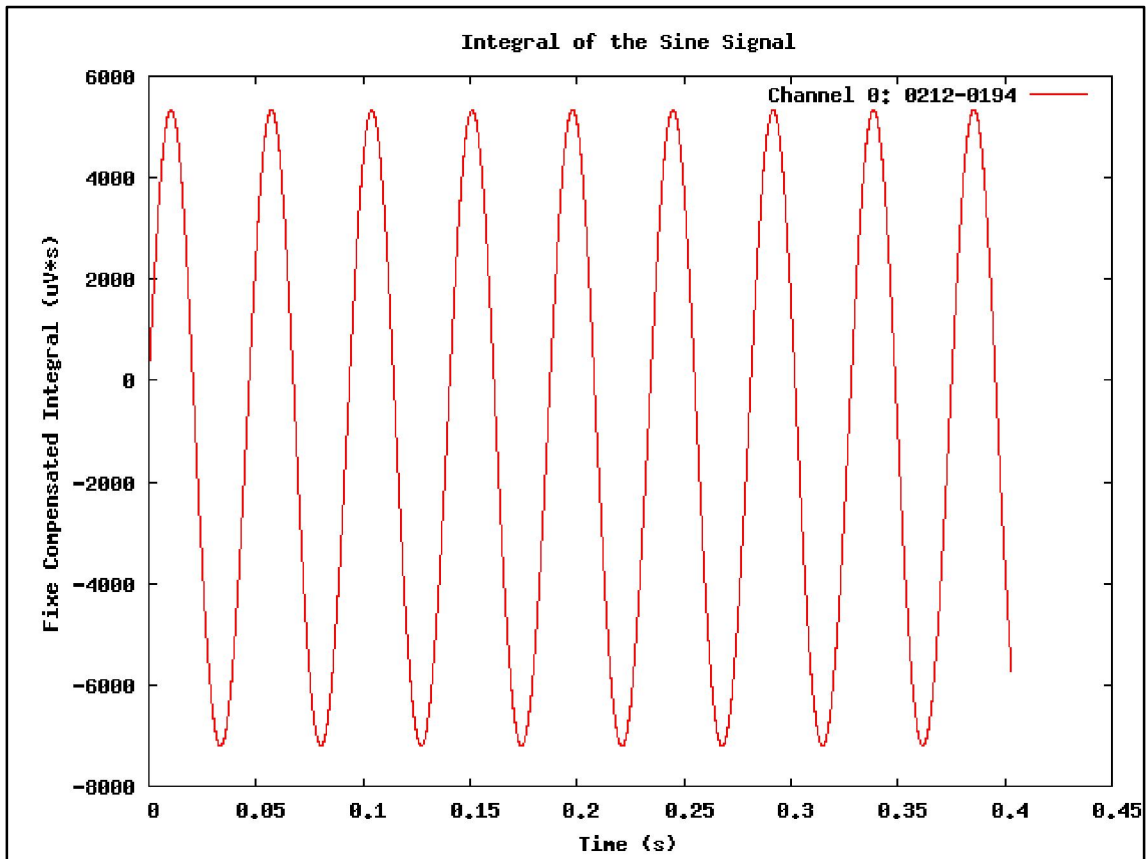


Figure 35 – Detail of Fixed Compensated Integral of Sine signal

4.3 – Noise acquisition and integration

The procedure though a Short-Circuit Input acquisition starts with the initial average calculation during 10 s of EO. The WO drift is calculated at the first 100s, if the acquisition is Pre-compensated (Figure 37), or at the end of the acquisition, if the acquisition is Post-compensated (Figure 36). Not all the data displayed were being stored in Hard Disk File but a selection of 1:100 samples. In figure Figure 85 is shown the signal acquired with the terminals short-circuited.

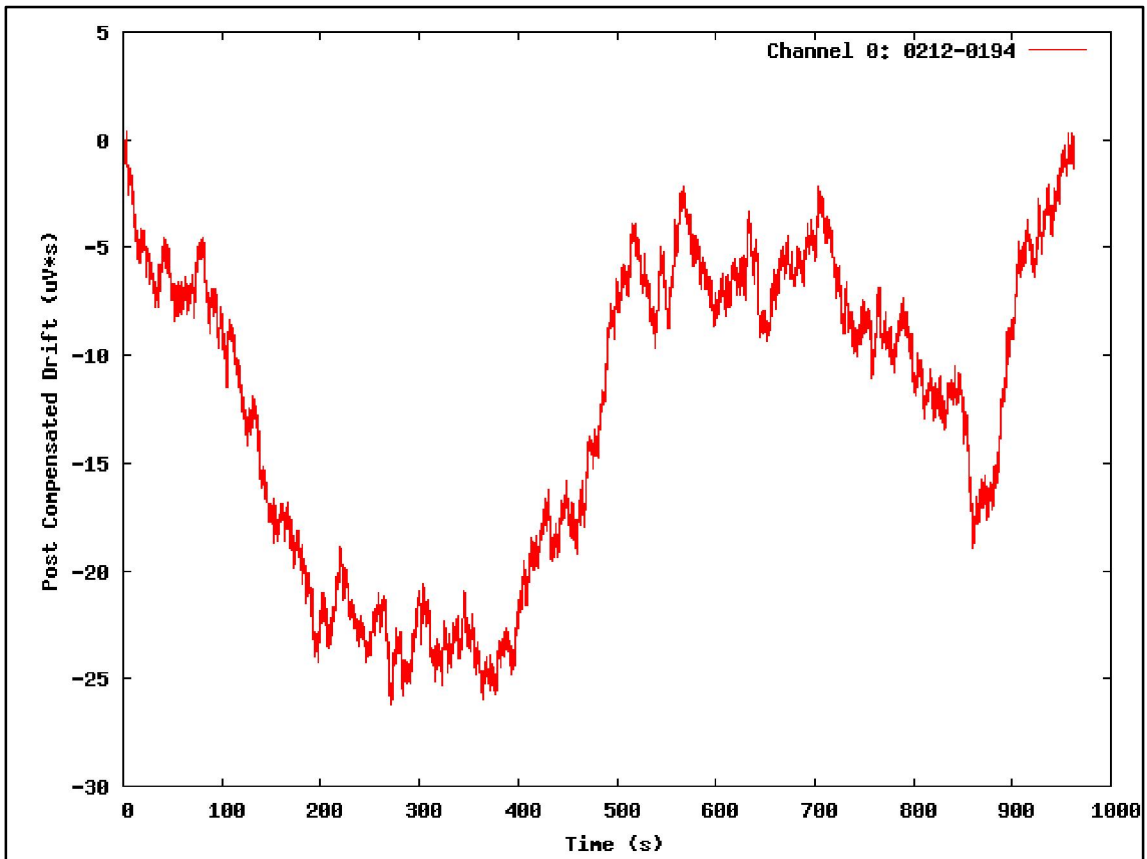


Figure 36 – Post-Compensated Drift of one module (acquisition with constant temperature)

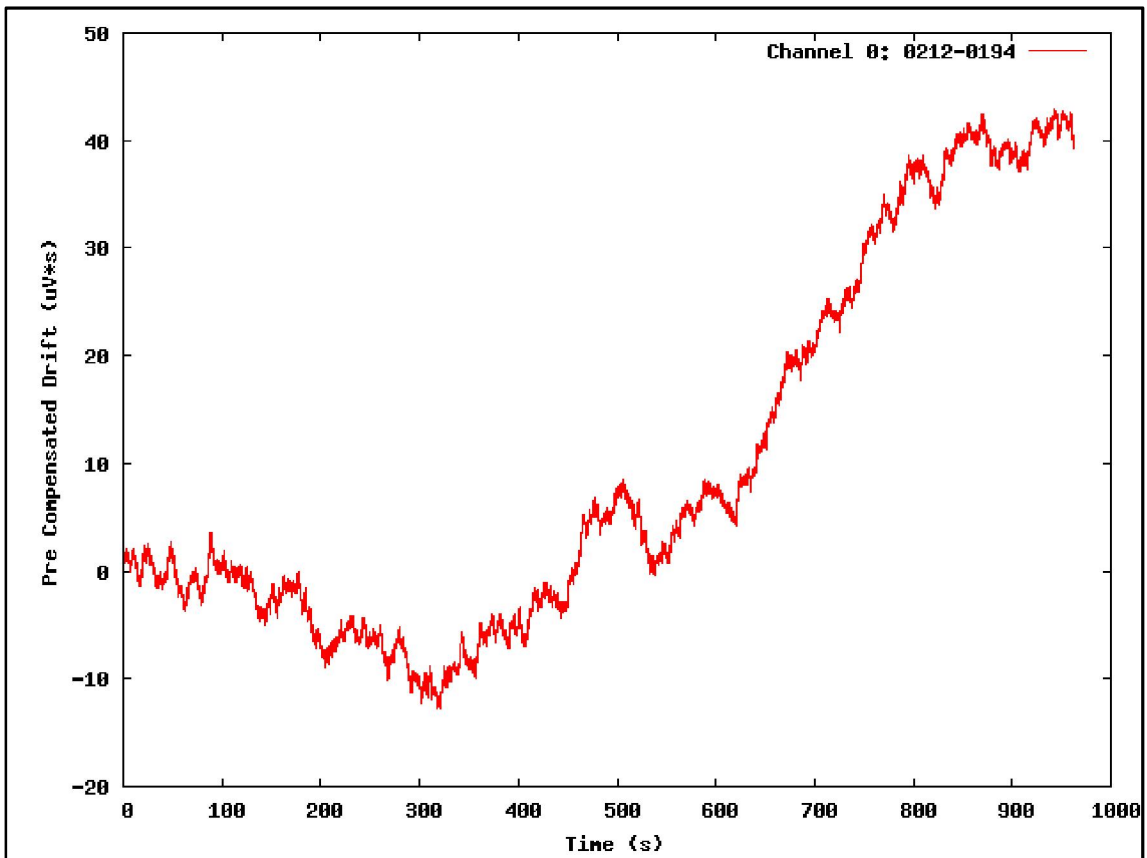


Figure 37 – Pre-Compensated long duration Drift of one module (acquisition with constant temperature)

One of the results presented is the drift obtain from acquisitions that lasted 1000 s with the input short-circuited and constant temperature. With a post-compensated analysis (after the total acquisition the final valor is set to zero) it was obtain a maximum drift of 25 $\mu\text{V}\times\text{s}$. With a pre-compensated analysis of 100 seconds (the parameter to adjust the incoming data is calculated after 100s) it was obtain a maximum of 50 $\mu\text{V}\times\text{s}$ after 900 seconds of sampling.

In Figure 38 and Figure 39 is graphically presented some of the parameters that are afterwards referred.

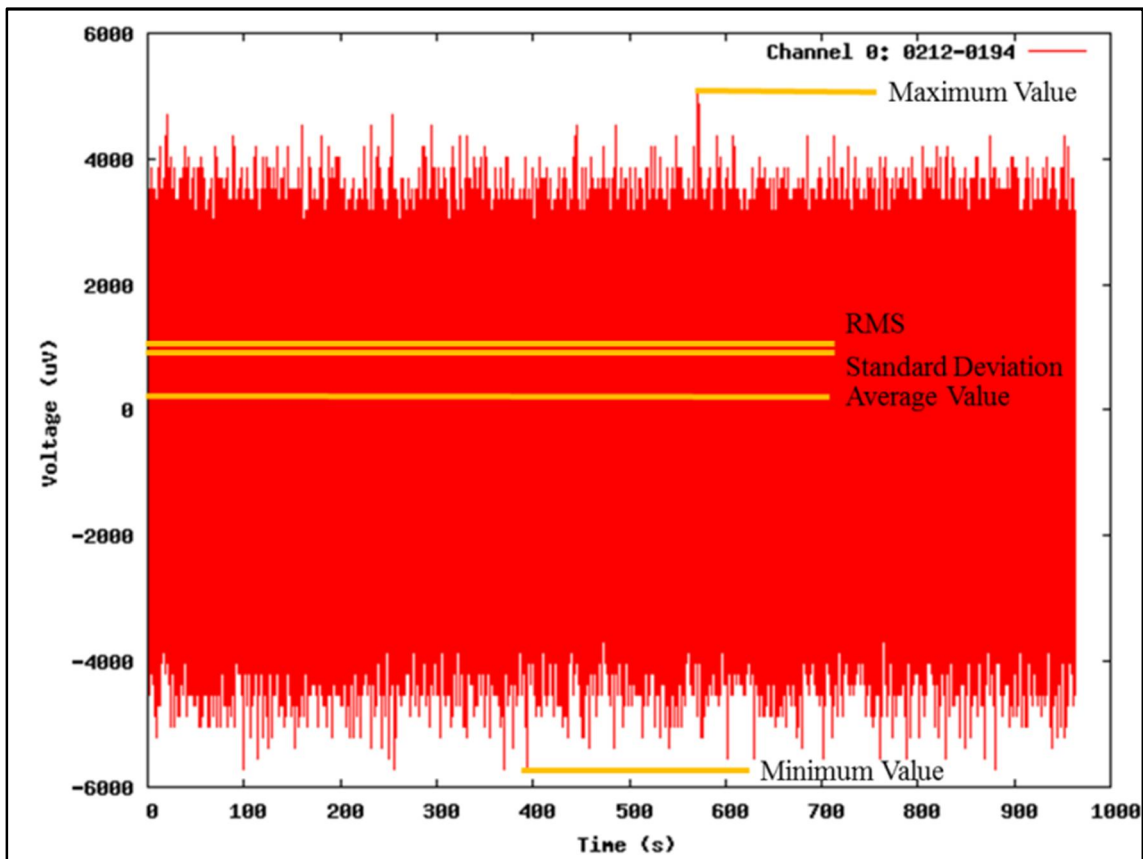


Figure 38 - Raw data from a long acquisition of 1000s, it is shown in the image some important values as the Average value and the RMS

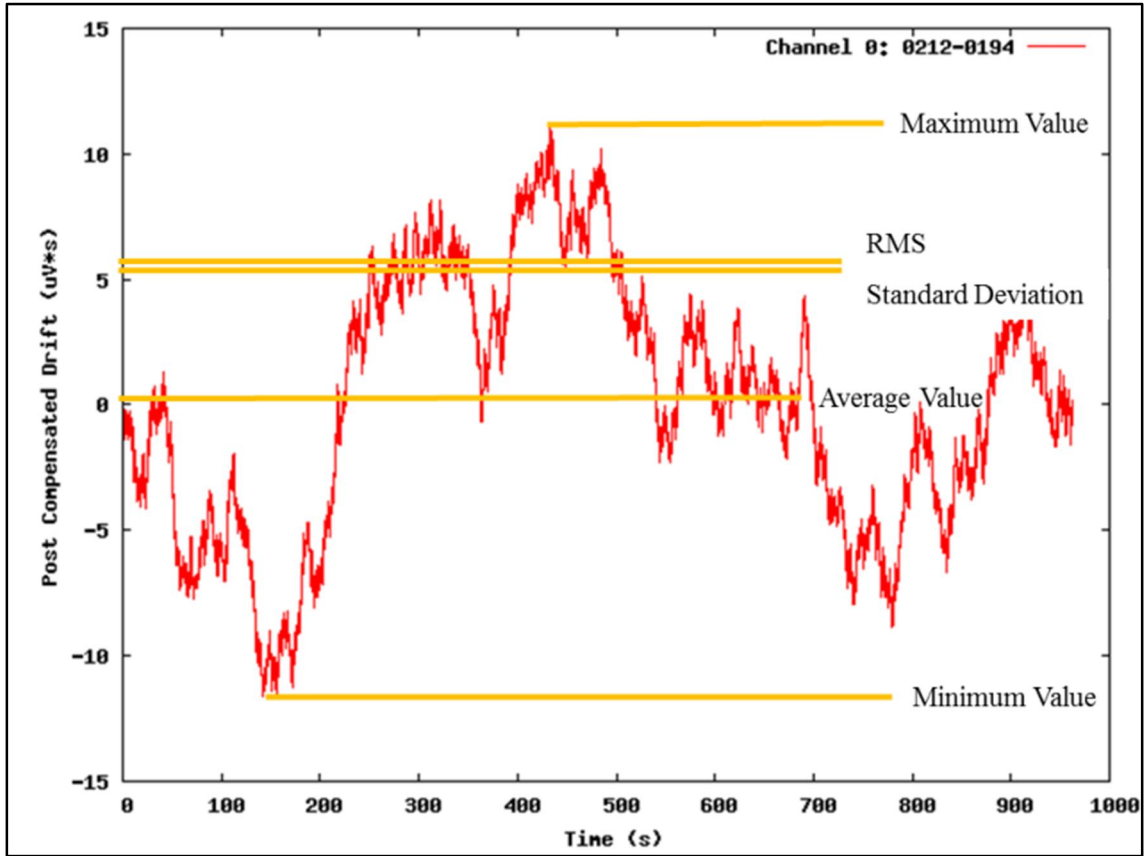


Figure 39 - Post compensated Integral from a long acquisition of 1000s, it is shown in the image some importante values as the Average Value and the RMS value

On the presented tables below to obtain the parameter EO in LSB it was done the average of the points presented by the ADC during an acquisition of 1 second. For EO in uV the used equation is below (Equation (9))

$$EO (\mu V) = EO(LSB) \times Conversion (LSB \rightarrow V) \times Conversion (V \rightarrow \mu V) \quad (9)$$

The conversion between LSB and Volt it was measured and it is equal to 1.729×10^{-4} V/LSB. And the conversion between V and μV is a factor of a million.

WO (LSB) shows the increment occurred after 1000 s of integration. To obtain it I have done the integral of the data throw 1000 seconds. The equation used to calculate WO ($\mu V \times s$) with WO(LSB) was (Equation (10)):

$$WO (\mu V \times s) = WO(LSB) \times Conversion (LSB \rightarrow V \times s) \times Conversion (V \rightarrow \mu V) \quad (10)$$

The conversion between LSB and Volt*s is equal to the conversion to LSB to Volt multiplied by the time between each acquisition (5×10^{-7} s, once the acquisition was done at 2 MSPS).

$$WO (\mu V) = \frac{WO (\mu V \times s)}{1000} \quad (11)$$

The presented average value is the average value of the data that was saved, which is a sample of 1 in 100 values of data. It was calculated by the formula:

$$\bar{x} = \frac{1}{N} \sum_{i=1}^N x_i \quad (12)$$

The Root Mean Square (RMS) and the Standard Deviation were calculated also with the saved data. The used formulas were:

$$RMS[x] = \sqrt{\frac{1}{N} \sum_{i=1}^N x_i^2} \quad (13)$$

$$Standard\ Deviation[x] = \sqrt{RMS[x]^2 - \bar{x}^2} \quad (14)$$

The Deviation % was used when there were not many samples, it was calculated by the formula:

$$Deviation\ \% = \text{Max} \left(\frac{Average - Value}{Average} \right) \times 100 \quad (15)$$

4.3.1 - First set of acquisitions: Post Compensated Drift with constant temperature. ADC modules of 100nF capacitor on the input filter

	Offset EO (LSB)	Average Offset EO (uV)	1000 s drift WO (LSB)	1000 s Average Drift WO (uV*s)	Mean WO (uV)
Channel 0 - a	-627	$(-1084 \pm 0) \times 10^2$	418498734	$(3616 \pm 2) \times 10^1$	36,16
Channel 0 - b	-627		418033982		
Channel 1 - a	17	$(3025 \pm 87) \times 10^0$	507920227	$(4379 \pm 12) \times 10^1$	43,79
Channel 1 - b	18		505224903		
Channel 2 - a	-234	$(-4046 \pm 0) \times 10^1$	245198484	$(2096 \pm 24) \times 10^1$	20,96
Channel 2 - b	-234		239787290		
Channel 3 - a	-467	$(-8057 \pm 18) \times 10^1$	216196841	$(1844 \pm 25) \times 10^1$	18,44
Channel 3 - b	-465		210343139		

Table 3 - Resume of Offset EO and Offset WO values

Post Compensated Drift	Average value (uV*s)	Maximum value (uV*s)	Minimum value (uV*s)	Standard Deviation (uV*s)	RMS (uV*s)
Channel 0 - a	-12,87	0,4140	-27,04	7,432	14,86
Channel 0 - b	0,1200	11,51	-12,03	5,193	5,194
Channel 1 - a	-26,49	1,994	-46,10	14,31	30,11
Channel 1 - b	17,44	42,00	-2,663	12,88	21,69
Channel 2 - a	16,44	30,61	-0,2430	7,250	17,97
Channel 2 - b	31,19	52,30	-0,9320	13,67	34,06
Channel 3 - a	-15,13	0,6640	-25,94	6,253	16,37
Channel 3 - b	-15,29	1,789	-24,16	5,733	16,33

Table 4 - Resume of RMS and Deviation values of Post-Compensated Drift

Offset	Average value (uV)	Maximum value (uV)	Minimum value (uV)	Standard Deviation (uV)	RMS (uV)
Channel 0 - a	-37,17	5360	-6224	852,1	852,9
Channel 0 - b	-37,29	5187	-5879	852,1	852,9
Channel 1 - a	-45,37	5014	-4841	895,2	896,4
Channel 1 - b	-45,14	4841	-4668	841,8	843,0
Channel 2 - a	-21,77	6052	-5014	895,9	896,1
Channel 2 - b	-21,69	6397	-6224	914,8	915,0
Channel 3 - a	-20,70	1020×10^1	-6397	901,1	901,3
Channel 3 - b	-20,42	1003×10^1	-6570	899,6	899,8

Table 5 - Resume of RMS and Deviation values of Offset

On the presented tables (Table 3, Table 4 and Table 5): Channel 0 = 0212-0194; Channel 1 = 0512-0160; Channel 2 = 0512-011X; Channel 3 = 0512-0144

The final results of this acquisition can be seen in Figure 40 and Figure 41.

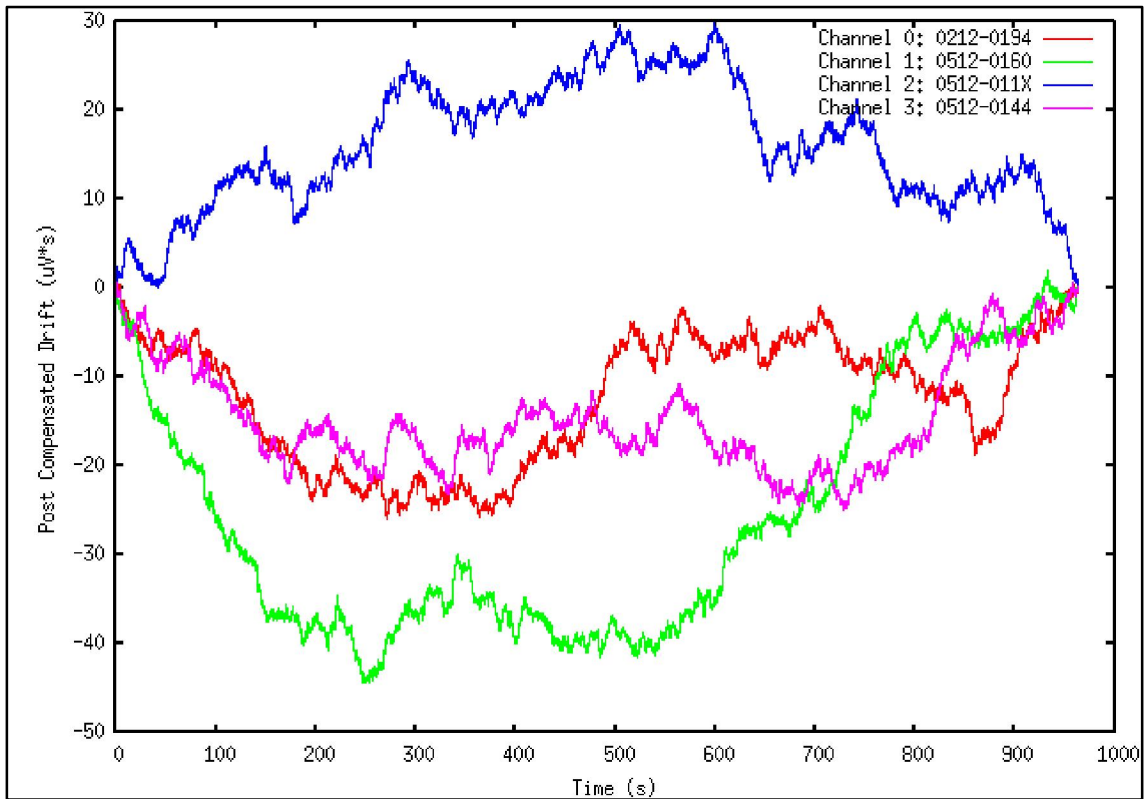


Figure 40 – Multiplot of all Post-Compensated Drift on acquisition 1a, acquisition done with constant temperature

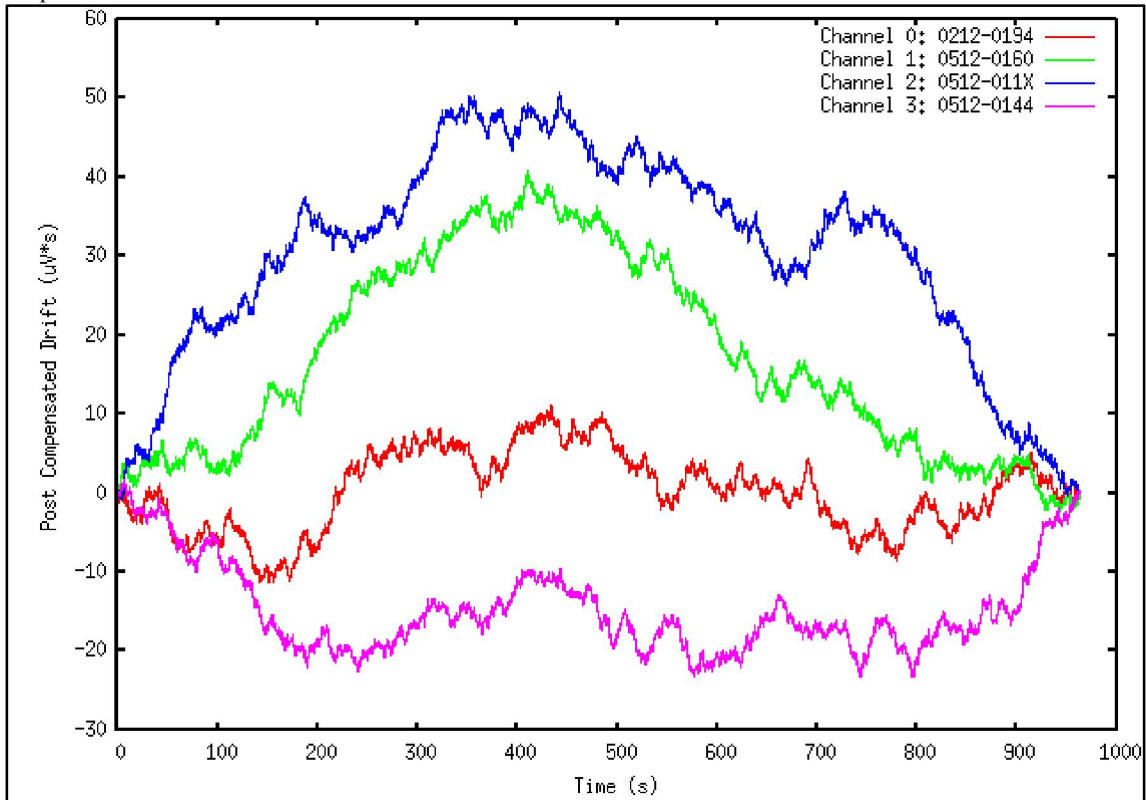


Figure 41 – Multiplot of all Post-Compensated Drift on acquisition 1b, acquisition done with constant temperature

4.3.2 - Second set of acquisitions: Pre Compensated Drift with constant temperature. Modules of 100nF capacitor on the input filter

	Offset EO (LSB)	Average Offset EO (uV)	1000 s drift WO (LSB)	1000 s Average drift WO (uV*s)	1 s Offset WO (uV)
Channel 0 – a	-627	$(-1084 \pm 0) \times 10^2$	418313822	$(3612 \pm 4) \times 10^1$	36,12
Channel 0 – b	-627		417361328		
Channel 1 – a	17	$(2853 \pm 86) \times 10^0$	506464975	$(4381 \pm 3) \times 10^1$	43,81
Channel 1 – b	16		507131126		
Channel 2 – a	-236	$(-4089 \pm 9) \times 10^1$	241543892	$(2087 \pm 1) \times 10^1$	20,87
Channel 2 – b	-237		241266119		
Channel 3 – a	-463	$(-7997 \pm 9) \times 10^1$	211802693	$(1831 \pm 0) \times 10^1$	18,31
Channel 3 – b	-462		211893836		

Table 6 - Resume of Offset EO and Offset WO values

Pre Compensated Drift	Average value (uV*s)	Maximum value (uV*s)	Minimum value (uV*s)	Standard Deviation (uV*s)	RMS (uV*s)
Channel 0 – a	10,02	44,24	-13,16	17,75	20,38
Channel 0 – b	24,06	62,24	-8,280	16,83	29,36
Channel 1 – a	-48,72	7,096	-81,33	25,51	55,00
Channel 1 – b	-5,472	23,15	-29,75	13,05	14,15
Channel 2 – a	43,70	76,16	-6,945	25,98	50,84
Channel 2 – b	16,73	45,46	-6,489	14,50	22,14
Channel 3 – a	55,01	113,5	-3,776	39,49	67,72
Channel 3 – b	-14,00	5,748	-41,46	11,12	17,88

Table 7 - Resume of RMS and Deviation values of Pre Compensated Drift

Offset	Average value (uV)	Maximum value (uV)	Minimum value (uV)	Standard Deviation (uV)	RMS (uV)
Channel 0 – a	-36,77	5187	-6052	860,5	861,3
Channel 0 – b	-37,17	5014	-6052	860,3	861,1
Channel 1 – a	-45,00	4668	-4841	840,1	841,3
Channel 1 – b	-45,60	4668	-4841	843,6	844,8
Channel 2 – a	-21,78	6052	-5187	888,3	888,5
Channel 2 – b	-21,55	5879	-5879	887,5	887,7
Channel 3 – a	-20,22	1037×10^1	-6570	891,7	891,9
Channel 3 – b	-20,61	1020×10^1	-6570	890,2	890,4

Table 8 - Resume of RMS and Deviation values of Offset

On the presented tables (Table 6, Table 7 and Table 8): Channel 0 = 0212-0194; Channel 1 = 0512-0160; Channel 2 = 0512-011X; Channel 3 = 0512-0144

The final results of this acquisition can be seen in Figure 42 and Figure 43.

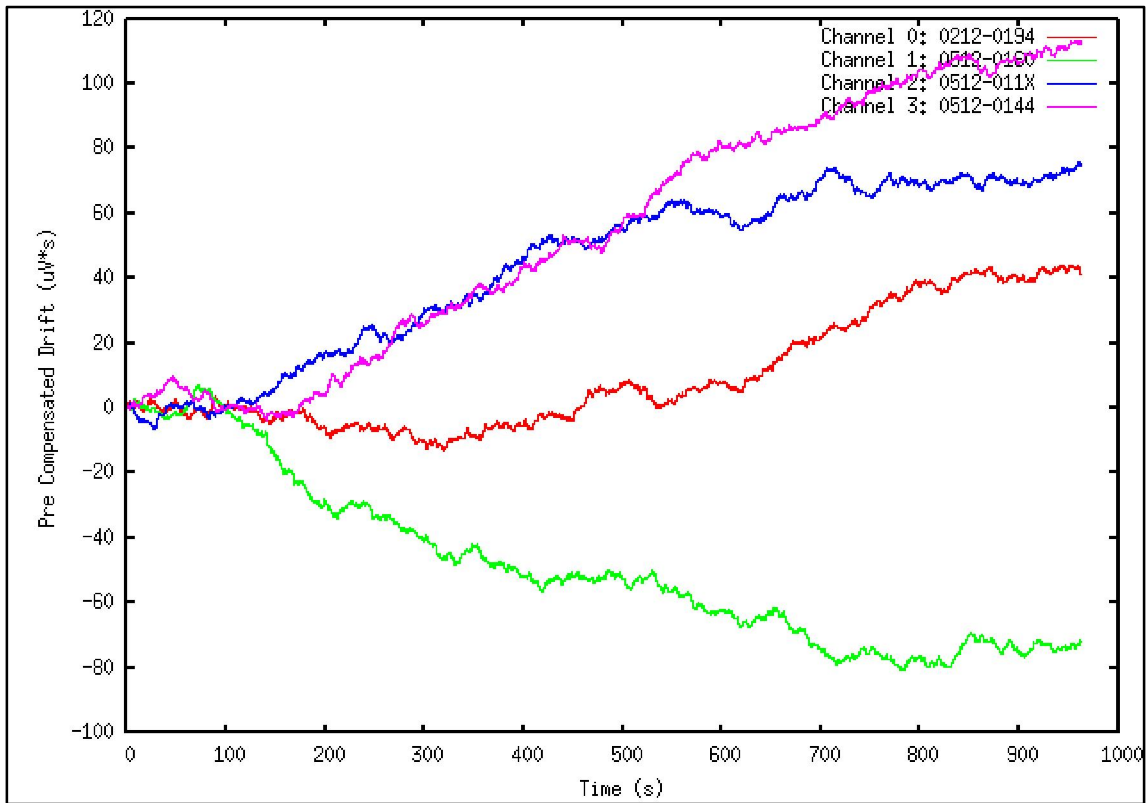


Figure 42 - Multiplot of all Pre Compensated Drift on acquisition 2a, acquisition done with constant temperature

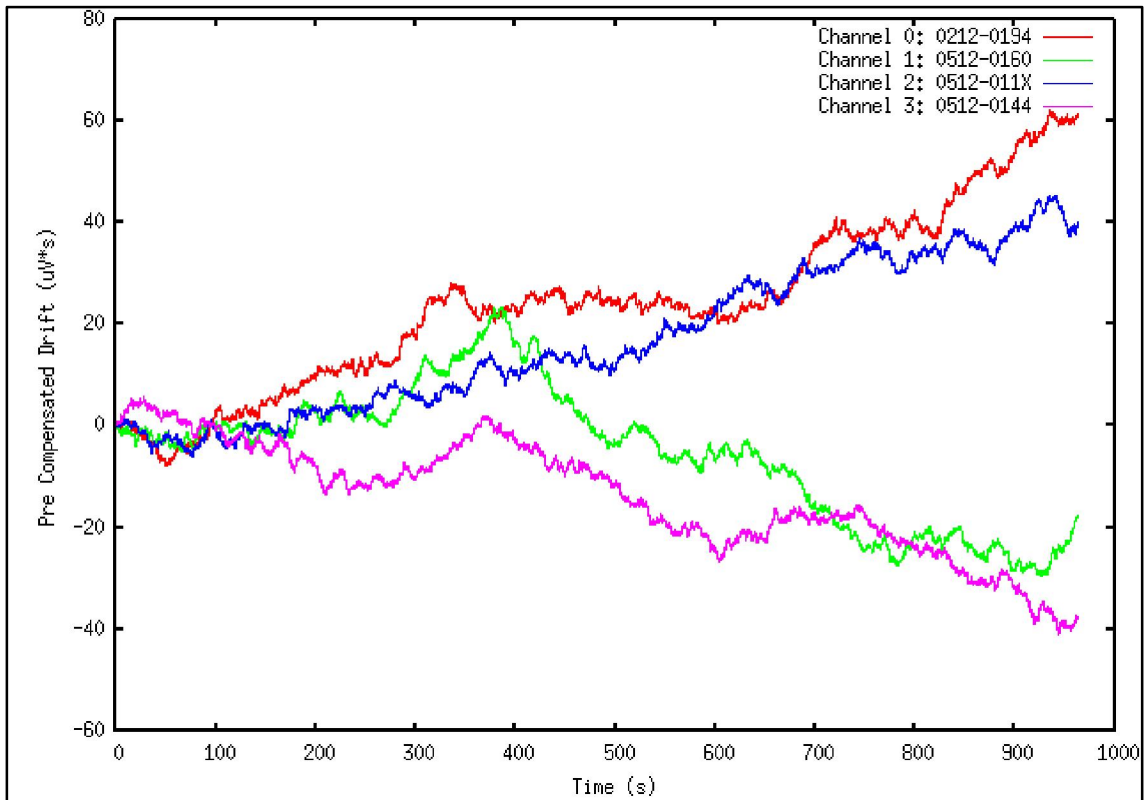


Figure 43- Multiplot of all Pre Compensated Drift on acquisition 2b, acquisition done with constant temperature

4.3.3 - Third set of acquisitions: Pre Compensated Drift of 100s with temperature variation and maximum temperature of 43°C. Modules of 100nF capacitor on the input filter.

During the tests in some acquisition the temperature of the modules were changed, by carefully heating the module with a hot air gun until temperatures of ~43°C.

	Offset EO (LSB)	Average Offset EO (uV)	1000 s drift WO (LSB)	1000 s Average drift WO (uV*s)	1 s Offset WO (uV)
Channel 0 – a	-627	$(-1085 \pm 1) \times 10^2$	426252777	$(3693 \pm 8) \times 10^1$	36,93
Channel 0 – b	-628		428095106		
Channel 1 – a	-237	$(-4098 \pm 0) \times 10^1$	253057974	$(2187 \pm 0) \times 10^1$	21,87
Channel 1 – b	-237		252986344		
Channel 2 – a	-461	$(-7971 \pm 0) \times 10^1$	213306867	$(1854 \pm 10) \times 10^1$	18,54
Channel 2 – b	-461		215565224		

Table 9 - Resume of EO and WO values with temperature variation

Pre Compensated Drift	Average value (uV*s)	Maximum value (uV*s)	Minimum value (uV*s)	Standard Deviation (uV*s)	RMS (uV*s)
Channel 0 – a	560,0	947,3	-19,76	381,4	677,5
Channel 0 – b	522,7	897,2	-15,63	362,4	636,0
Channel 1 – a	746,2	1073	-1,666	406,3	849,6
Channel 1 – b	775,3	1129	-5,778	437,1	890,0
Channel 2 – a	141,3	245,8	-4,703	90,01	167,6
Channel 2 – b	216,1	361,9	-8,818	140,1	257,6

Table 10 - Resume of RMS and Deviation values of Pre Compensated Drift with temperature variation

Offset	Average value (uV)	Maximum value (uV)	Minimum value (uV)	Standard Deviation (uV)	RMS (uV)
Channel 0 – a	-37,92	6397	-7435	1022	1023
Channel 0 – b	-37,25	6224	-7262	989,1	989,8
Channel 1 – a	-22,74	6397	-7089	1340	1340
Channel 1 – b	-21,81	6397	-6570	1250	1250
Channel 2 – a	-20,40	9855	-6916	938,7	939,0
Channel 2 – b	-17,86	1003×10^1	-6916	956,6	956,7

Table 11 - Resume of RMS and Deviation values of Offset with temperature variation

On the presented tables (Table 9, Table 10 and Table 11): Channel 0 = 0212-0194; Channel 1 = 0512-011X; Channel 2 = 0512-0144

As it can be seen bellow (Figure 44) between 120 s and 300 s the modules were heated to a temperature of 43°C.

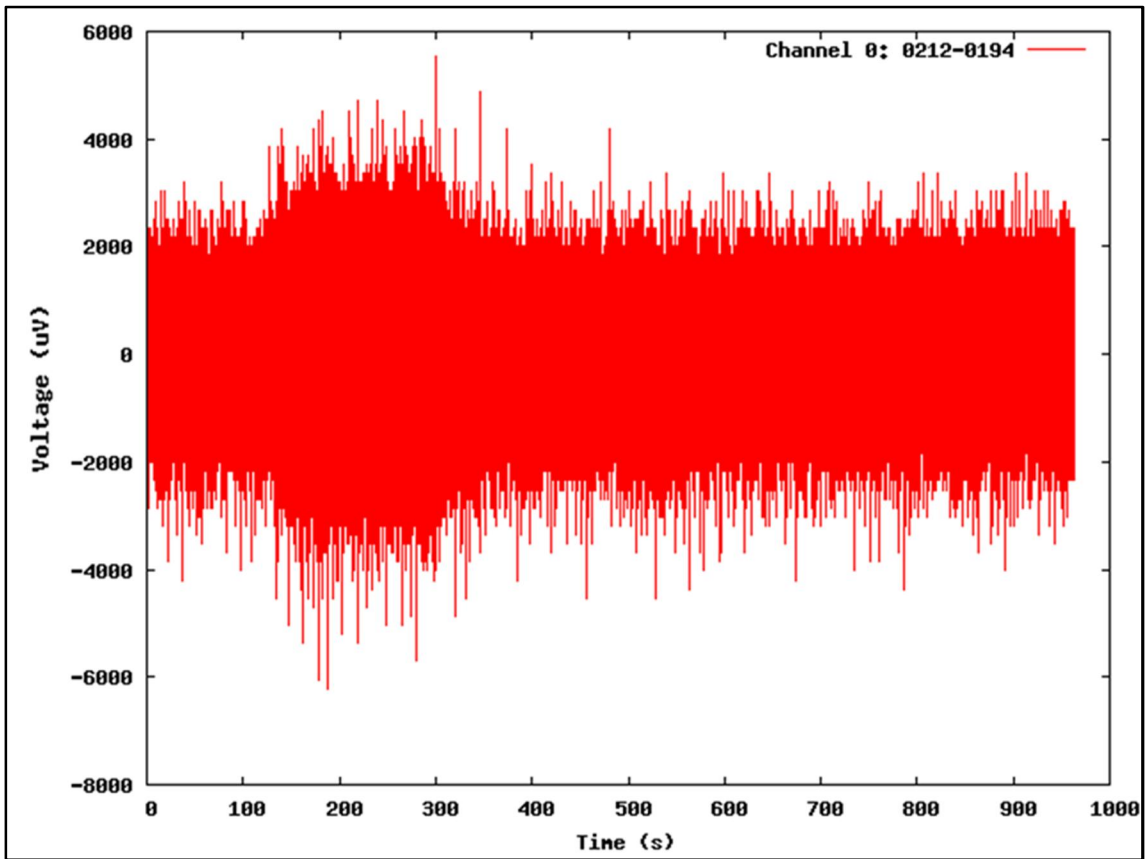


Figure 44 - Offset of one module (acquisition with temperature variation)

The final results of this acquisition can be seen in Figure 45 and Figure 46. It is seen that the short-circuited signal (electronic noise) was influenced by the changes of temperature that were induced.

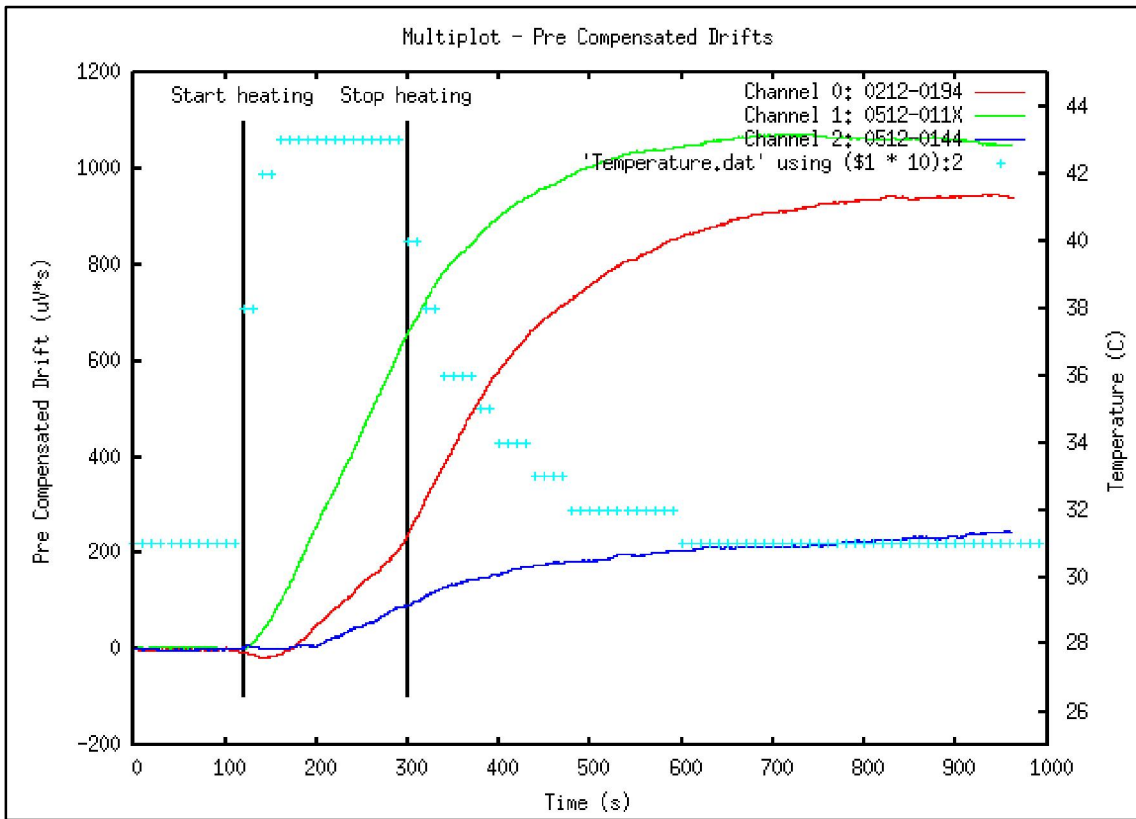


Figure 45 - Multiplot of all Pre Compensated Drift on acquisition 3a, (acquisition with module heating)

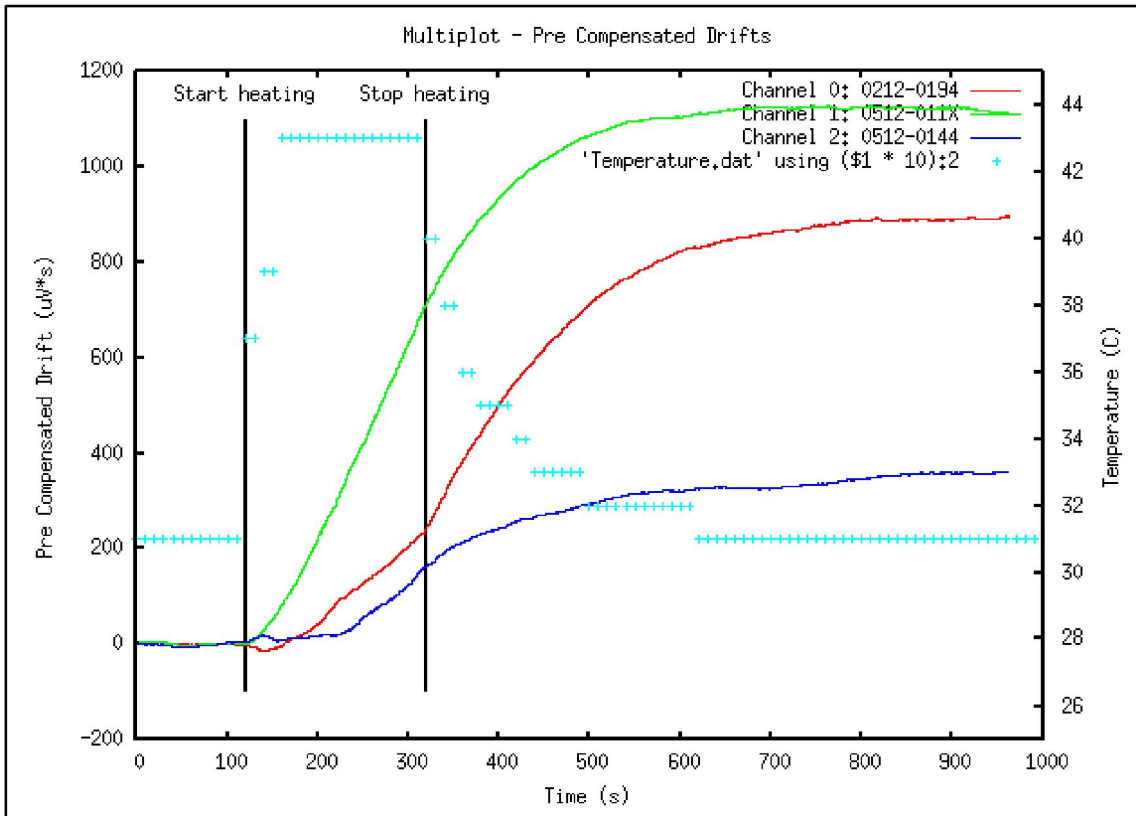


Figure 46 - Multiplot of all Pre Compensated Drift on acquisition 3b, (acquisition with module heating)

4.3.4 – Fourth set of acquisitions: Pre Compensated Drift of 60s with temperature variation and maximum temperature of 43°C. Modules of 100pF capacitor on the input filter.

	Offset EO (LSB)	Average Offset EO (uV)	1000 s drift WO (LSB)	1000 s Average drift WO (uV*s)	1 s Offset WO (uV)
Channel 0 – a	-14	$(-2421 \pm 0) \times 10^0$	407493840	$(3526 \pm 3) \times 10^1$	35,26
Channel 0 – b	-14		408113614		
Channel 1 – a	-373	$(-6449 \pm 0) \times 10^1$	233596854	$(2017 \pm 2) \times 10^1$	20,17
Channel 1 – b	-373		233047462		
Channel 2 – a	-467	$(-8057 \pm 18) \times 10^1$	210670257	$(1825 \pm 4) \times 10^1$	18,25
Channel 2 – b	-465		211479321		

Table 12 - Resume of EO and WO values with temperature variation

Pre Compensated Drift	Average value (uV*s)	Maximum value (uV*s)	Minimum value (uV*s)	Standard Deviation (uV*s)	RMS (uV*s)
Channel 0 – a	373,7	642,1	-38,81	231,8	439,8
Channel 0 – b	302,0	464,2	-28,86	182,8	353,0
Channel 1 – a	350,4	474,4	-5,500	168,8	389,0
Channel 1 – b	373,7	523,6	-4,241	184,9	416,9
Channel 2 – a	164,1	314,9	-18,84	100,5	192,4
Channel 2 – b	192,8	318,4	-26,18	116,0	225,0

Table 13 - Resume of RMS and Deviation values of Pre Compensated Drift with temperature variation

Offset	Average value (uV)	Maximum value (uV)	Minimum value (uV)	Standard Deviation (uV)	RMS (uV)
Channel 0 – a	-47,16	6743×10^0	-8299	1354	1354
Channel 0 – b	-47,32	6224×10^0	-8126	1276	1277
Channel 1 – a	-19,45	1089×10^1	-7781	1191	1191
Channel 1 – b	-19,21	1141×10^1	-7435	1116	1116
Channel 2 – a	-18,51	9855×10^0	-6916	967,6	967,7
Channel 2 – b	-18,32	1037×10^1	-6224	973,0	973,2

Table 14 - Resume of RMS and Deviation values of Offset with temperature variation

On the presented tables (Table 12, Table 13 and Table 14): Channel 0 = 0512-0101; Channel 1 = 0512-0012; Channel 2 = 0512-0144

The final results of this acquisition can be seen in Figure 47 and Figure 48. It is seen that the short-circuited signal (electronic noise) was influenced by the changes of temperature that were induced.

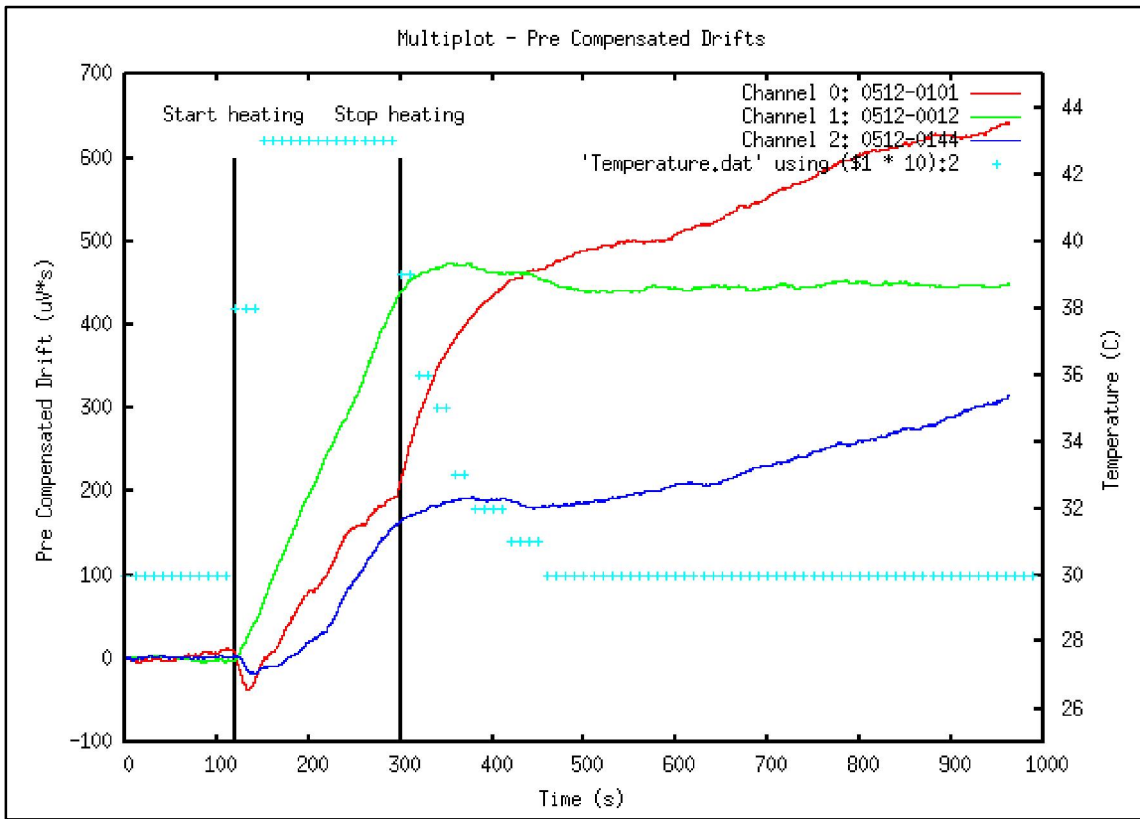


Figure 47 - Multiplot of all Pre Compensated Drift on acquisition 4a (acquisition with module heating)

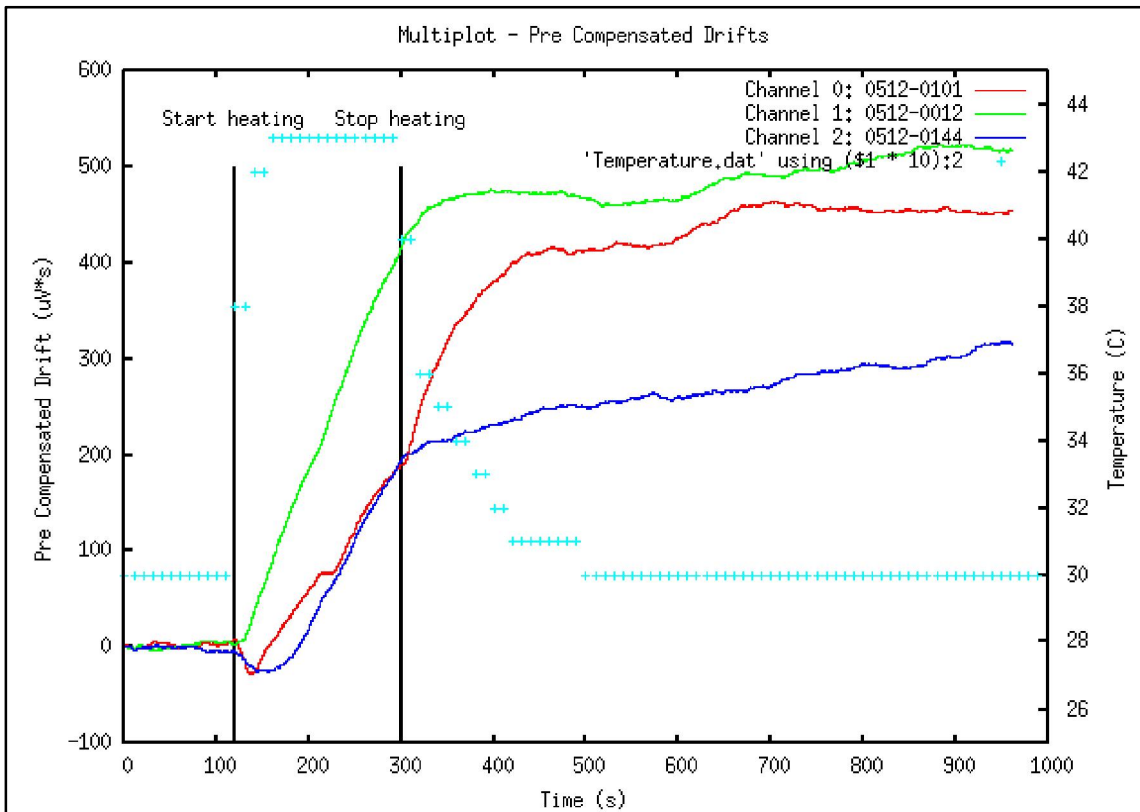


Figure 48 - Multiplot of all Pre Compensated Drift on acquisition 4b (acquisition with module heating)

4.4 - Acquisition of signals from ISTTOK's Mirnov coils

This sub-chapter is about the acquisition of signals coming from 12 Mirnov coils at 2MSPS with digital ADC modules with galvanic isolation developed by IPFN. Photographs of ISTTOK and the crate can be seen in Figure 49.



Figure 49 – Pictures from ISTTOK's room, at the left is the plug from the signals coming from the Mirnov coils of the tokamak, at the right in the used ATCA crate

This sub-chapter is divided in two sections, the first is about pulsed plasma acquisition and the second is about AC plasmas at ISTTOK. A pulsed plasma during the operation of a tokamak is a shot discharge in which the plasma goes one direction. An AC Plasma Discharge is a plasma discharge in which the tokamak's magnetic field generated by the primary is inverted (by inverting the current on the primary), and with this inversion the plasma current is inverted so that the time in the tokamak that we can have plasma can be much larger.

To measure the current of the plasma in a tokamak it can be used a Rogowski Coil due to the Ampère Law: The line integral of the magnetic \vec{B} -field around a closed curve is proportional to the total current I passing through a surface enclosed by the curve (Equation (16))

$$\oint \vec{B} \cdot d\vec{l} = \mu I \quad (16)$$

Instead of one helical coil of wire around a section of the tokamak (a Rogowski coil) it can be used several coils around that same section (Mirnov Coils) to measure the plasma current. On the sections below the current of the plasma was obtained by using Mirnov Coils.

4.4.1 – Pulsed Plasma at ISTTOK

On these tests it was used two types of modules with different filters, modules that have a filter with a 100nF capacitor and the modules that have a filter of 100pF. The phase-modulating frequency used was 40 kHz and 1 kHz.

Position Number	Reference	Type
1	0212-0194	100nF
2	0512-0160	100nF
3	0512-011X	100nF
4	0512-0144	100pF
5	0512-0101	100pF
6	0512-0020	100pF
7	0512-0128	100pF
8	0512-0152	100nF
9	0512-0179	100pF
10	0512-0187	100pF
11	0512-008X	100pF
12	0512-0098	100pF

Table 15 – Used ADC modules

During the acquisitions it was detected that one of the board channels was not working well. It was channel number 5 that was not previously tested. This board channel was substituted by channel 13 from the board (the terminals of the coil at position 5 are connected to channel 13 of the board).

Before the discharge happened it was needed to acquire 10 s for the calculations of EO (After Chop Offset). The acquisition took another 10s, the data coming from the 12 channels are first recorded in the computer's RAM and at the end of acquisition placed in memory, taking the time required.

At the end of the acquisition it was needed some data manipulation, due to noise integration, to have a compensated integral. After 1s from the start of the data's integration WO was calculated (the increment that the integration suffers).

To calibrate the data from the signal Intensity Vs Time graphics the peaks caused by the plasma current from the 12 different positions of the coils were sum and this value has to have 4kA, so it calculated then this conversion factor. The conversion constant was then divided by the number of the coils and multiplied to the values of the data from the graphics.

Below is shown the results from two acquisitions, one with the chop frequency equal to 1kHz and a time of discharge of 25 ms. The other with the chop frequency equal to 40 kHz and a time of the discharge of 28 ms.

One of the integrals from a Mirnov coils is shown in Figure 51. The signal caused by the plasma occurred at second ~6.2 and is shown in a blue rectangle. The coils are influenced also by the toroidal field, the instants when the field is being generated are limited by the black pointers. The last statement can be explained by the possibility that during the installation of the Mirnov Coils on a line section of ISTTOK it was unintentionally implemented a deviation relatively to this line section, causing the coils to be influenced by the toroidal field.

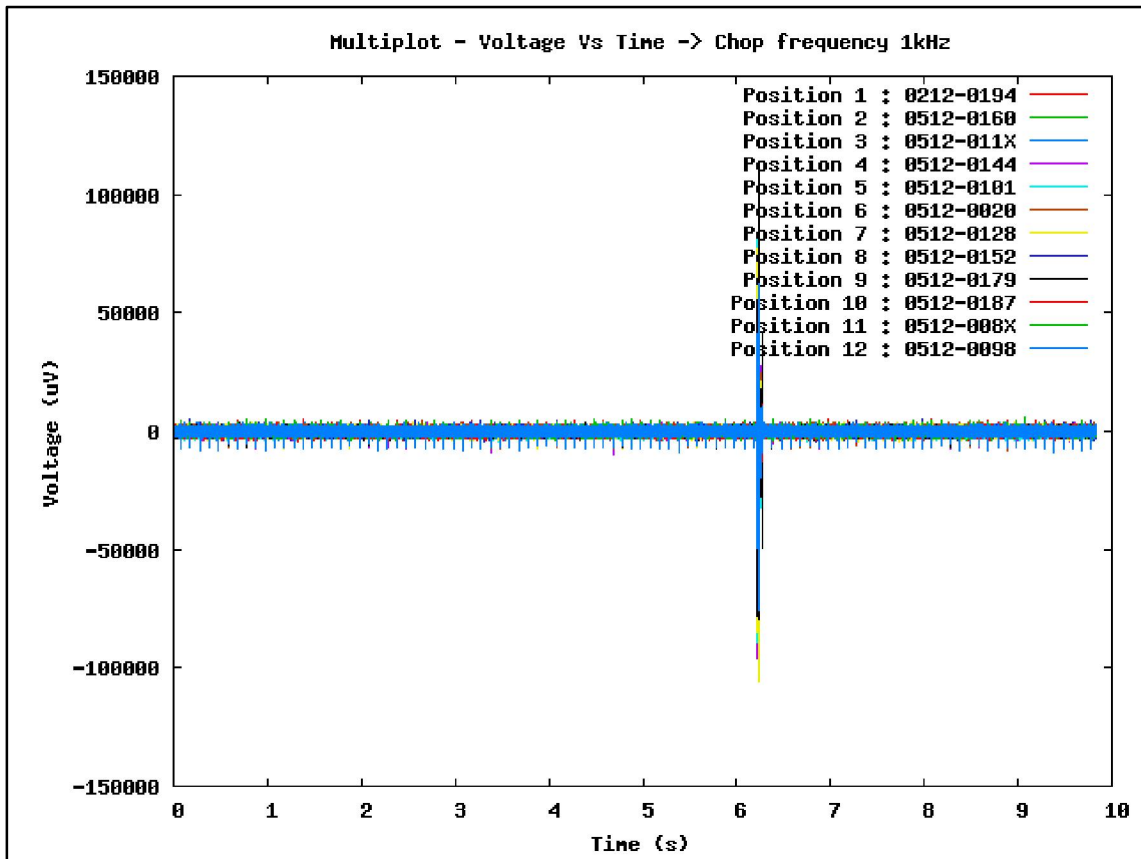


Figure 50 – Raw signals from all the Mirnov coils

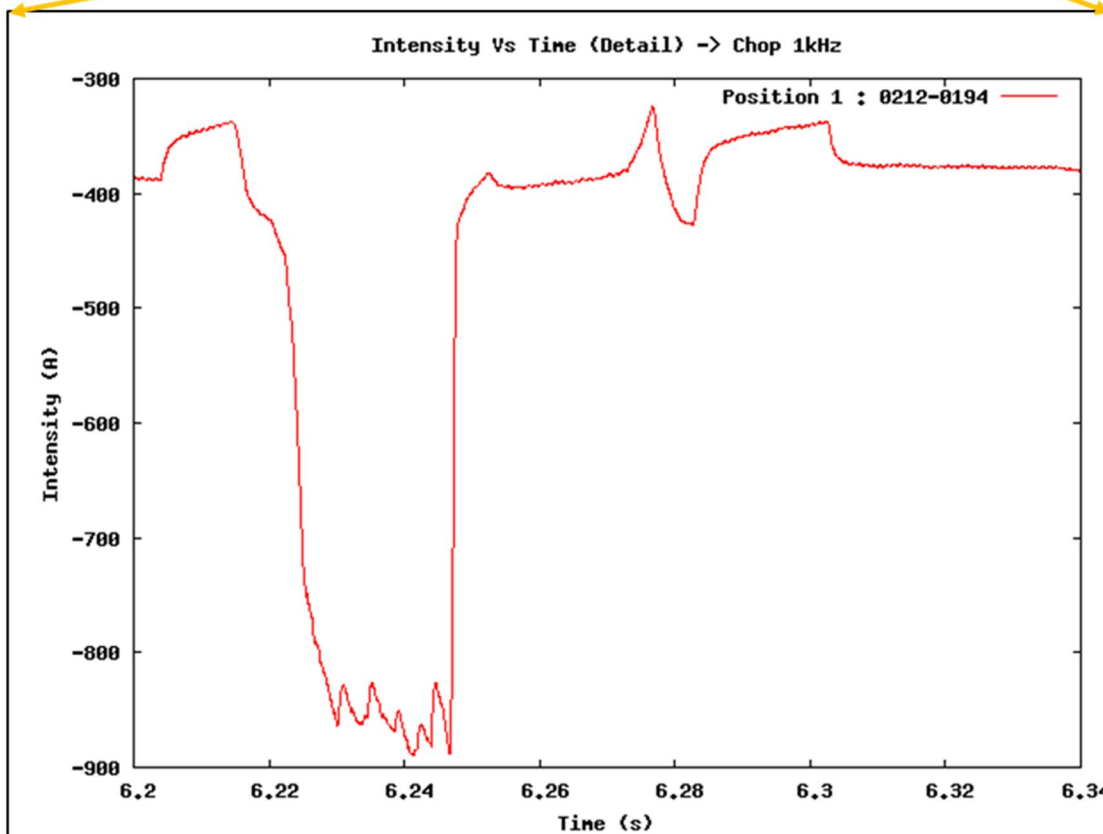
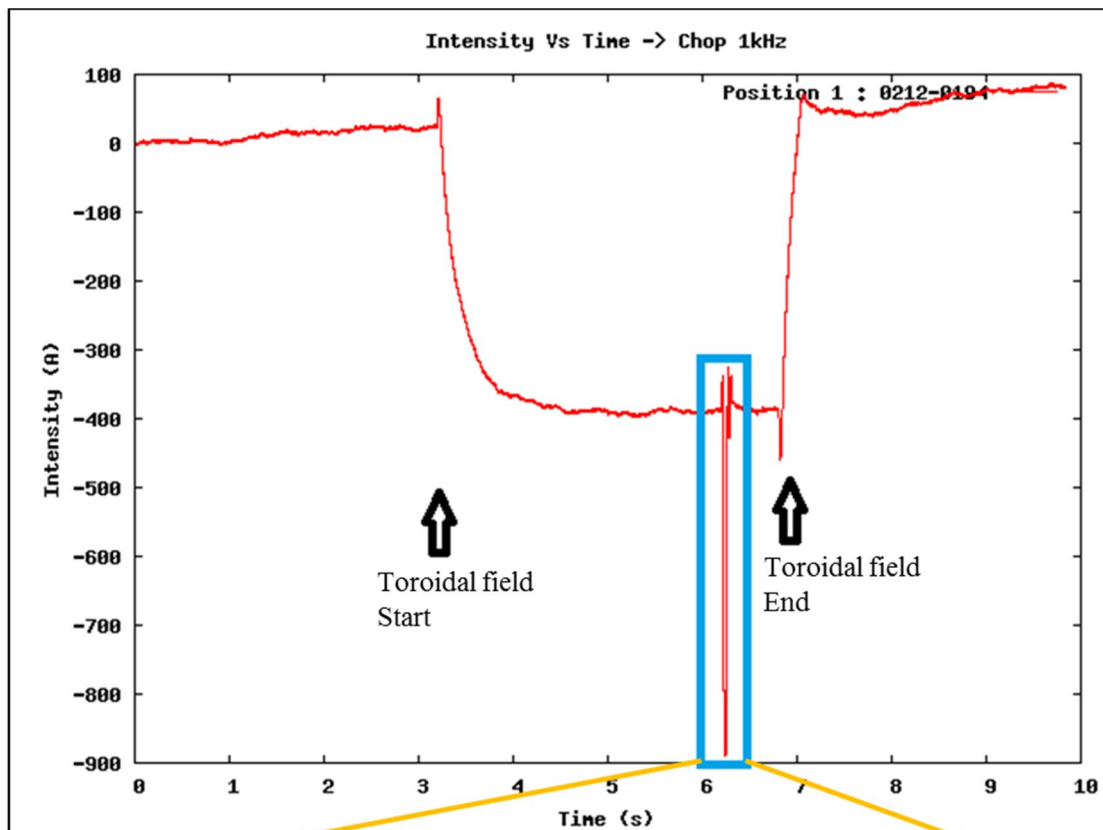


Figure 51 - Integral of the signal from one Mirnov coil during the whole ISTTOK operating sequence (top), and from the plasma discharge (bottom)

By analyzing Figure 52 it can be said that the signals occurred in the same instant (as expected).

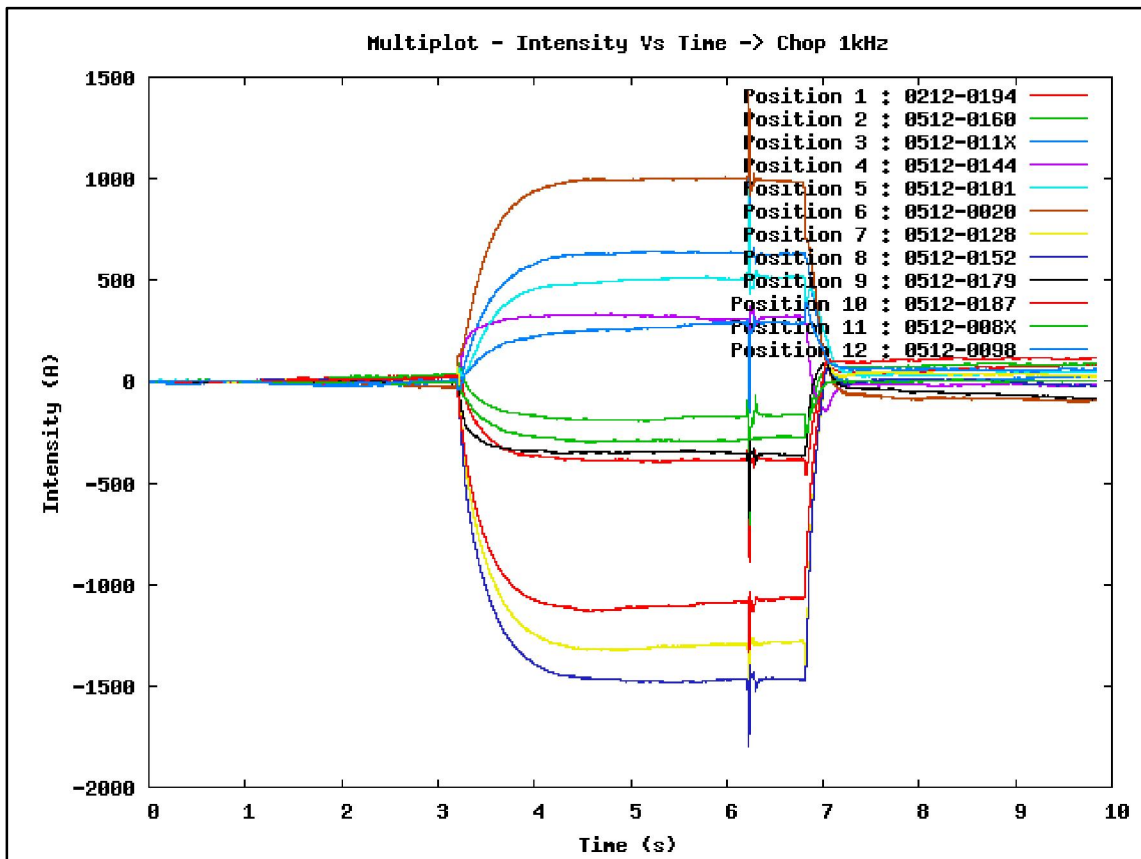


Figure 52 – Integral of the signal from all coils during the whole ISTTOK operating sequence

It can be seen in Figure 53 the intensity of the signal showing the plasma discharge contribution around 6,2 seconds. Some of signals are inverted (channel 1, 2, 4, 7, 8, 9, 10 and 12), a plausible explanation from this fact is that during the installation on the ISTTOK of the Mirnov coils it is possible that some of the coils were connected reversed comparing to others.

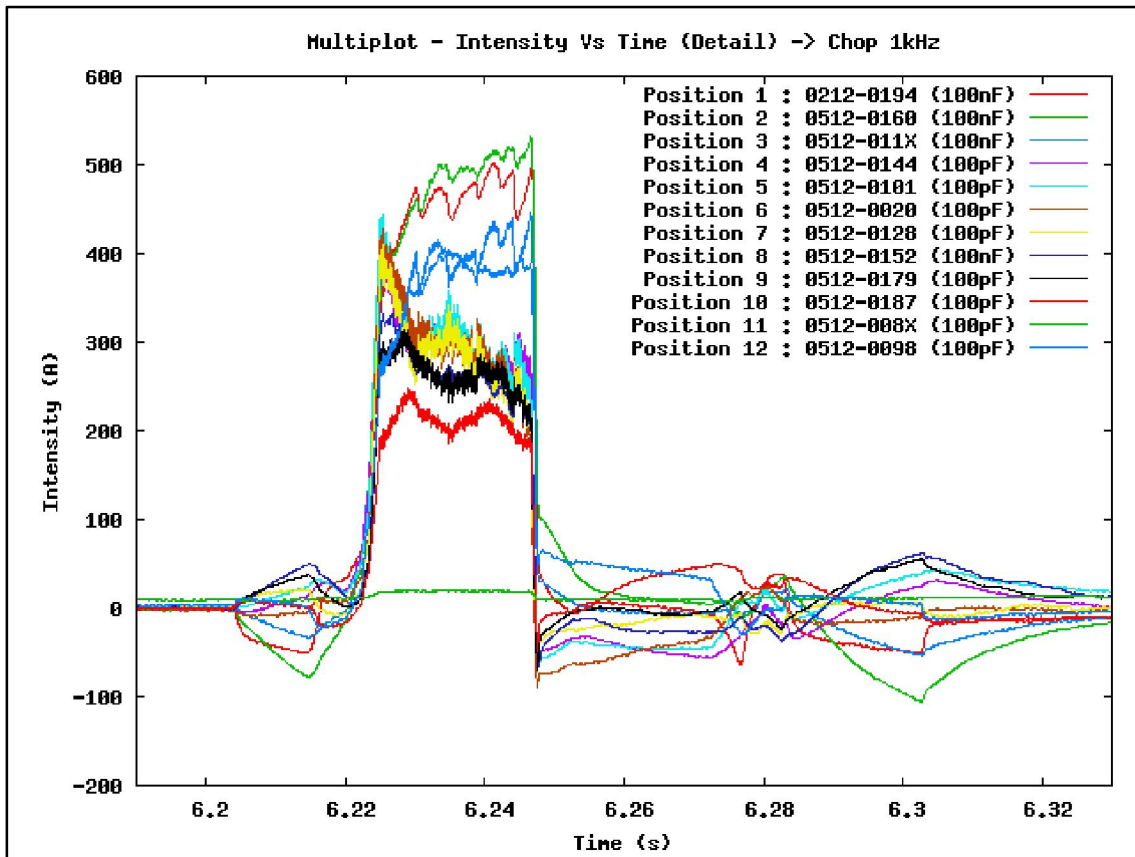


Figure 53 - Integral of the signal from all coils in detail, on the beginning this graphic the values of the integral were set to zero and some of the signals were inverted

One of the signals, the signal that comes from the coil in position number 11, is much smaller than the other signals. This fact that the signal from coils number 11 is smaller can be explained by the fact that there could be some deviation during the installation so that the axes are not centered with the poloidal section of the plasma column.

The difference that is seen between different coils is mainly due to different distances from the plasma column to the coils. (The plasma is not centered vertically or horizontally). Also the coil calibration factors might differ.

The final results of acquisitions with the chop frequency equal to 40kHz is listed below (Figure 54). The shown results are very similar with the ones obtained with a chop frequency equal to 1kHz (Figure 53), as expected.

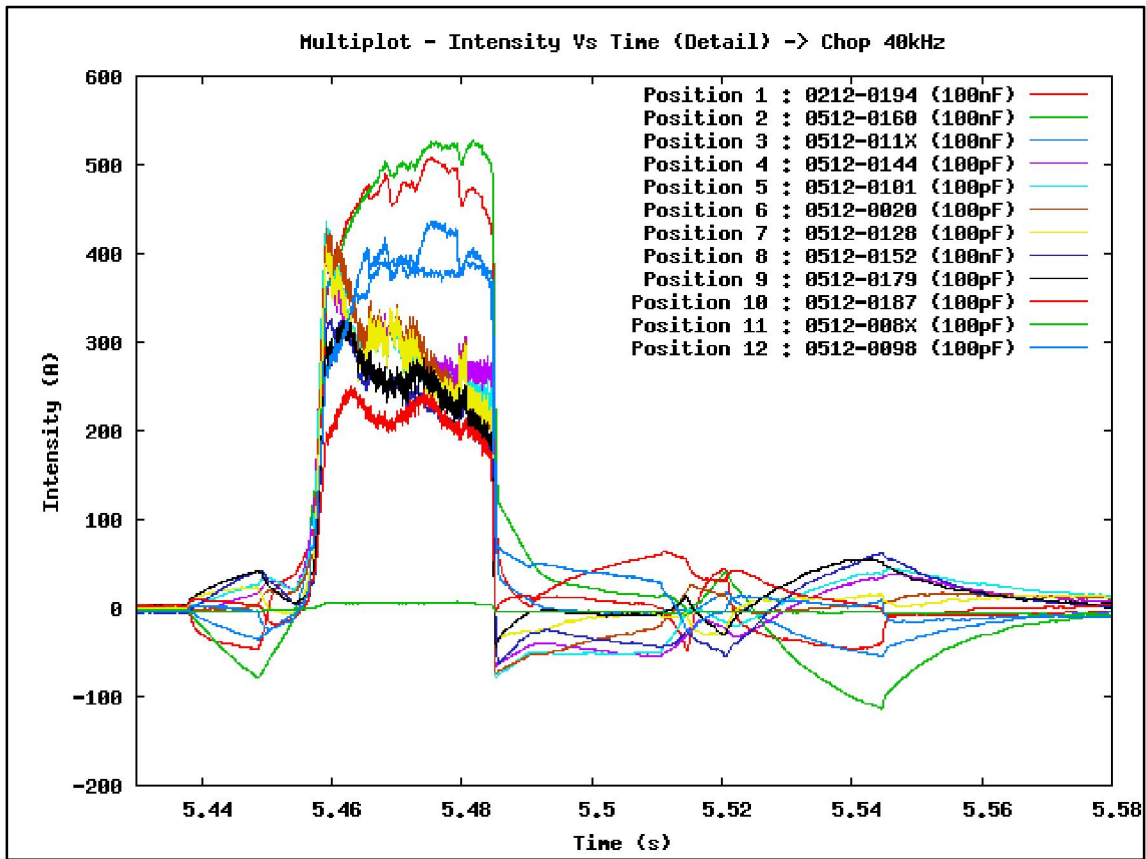


Figure 54 - Integral of the signal from all coils in detail, on the beginning this graphic the values of the integral were set to zero

The resume of the Offset values can be seen at Table 16 and Table 17, they are similar to the values obtained with the short-circuited acquisitions.

Channel	Chop frequency 40 Hz		Chop frequency 1 Hz	
	EO (LSB)	EO (uV)	EO (LSB)	EO (uV)
1	-628	$-1,086 \times 10^5$	-628	$-1,086 \times 10^5$
2	11	$1,902 \times 10^3$	12	$2,075 \times 10^3$
3	-236	$-4,080 \times 10^4$	-235	$-4,063 \times 10^4$
4	-465	$-8,040 \times 10^4$	-464	$-8,023 \times 10^4$
5	-16	$-2,766 \times 10^3$	-15	$-2,594 \times 10^3$
6	175	$3,026 \times 10^4$	176	$3,043 \times 10^4$
7	-8	$-1,383 \times 10^3$	-5	$-8,645 \times 10^2$
8	-656	$-1,134 \times 10^5$	-657	$-1,136 \times 10^5$
9	-787	$-1,361 \times 10^5$	-786	$-1,359 \times 10^5$
10	-733	$-1,267 \times 10^5$	-733	$-1,267 \times 10^5$
11	-585	$-1,011 \times 10^5$	-586	$-1,013 \times 10^5$
12	43	$7,435 \times 10^3$	44	$7,608 \times 10^3$

Table 16 – EO parameter values

Channel	Chop frequency 40 Hz			Chop frequency 1 Hz		
	WO (LSB)	WO (1s drift LSB)	WO (1s drift uV*s)	WO (LSB)	WO (1s drift LSB)	WO (1s drift uV*s)
1	$1,194 \times 10^0$	$2,348 \times 10^6$	$2,030 \times 10^2$	$1,685 \times 10^{-1}$	$3,312 \times 10^5$	$2,863 \times 10^1$
2	$1,571 \times 10^0$	$3,089 \times 10^6$	$2,670 \times 10^2$	$2,118 \times 10^{-1}$	$4,164 \times 10^5$	$3,600 \times 10^1$
3	$-2,652 \times 10^{-1}$	$-5,214 \times 10^6$	$-4,507 \times 10^1$	$1,178 \times 10^{-1}$	$2,317 \times 10^5$	$2,003 \times 10^1$
4	$-2,097 \times 10^{-1}$	$-4,123 \times 10^6$	$-3,565 \times 10^1$	$1,510 \times 10^{-1}$	$2,969 \times 10^5$	$2,566 \times 10^1$
5	$3,467 \times 10^{-1}$	$6,816 \times 10^6$	$5,893 \times 10^1$	$1,847 \times 10^{-1}$	$3,632 \times 10^5$	$3,140 \times 10^1$
6	$3,155 \times 10^{-1}$	$6,203 \times 10^6$	$5,363 \times 10^1$	$1,456 \times 10^{-1}$	$2,862 \times 10^5$	$2,474 \times 10^1$
7	$4,065 \times 10^{-1}$	$7,991 \times 10^6$	$6,909 \times 10^1$	$1,624 \times 10^{-1}$	$3,193 \times 10^5$	$2,760 \times 10^1$
8	$-7,687 \times 10^{-1}$	$-1,511 \times 10^6$	$-1,306 \times 10^2$	$1,103 \times 10^{-1}$	$2,169 \times 10^5$	$1,875 \times 10^1$
9	$8,433 \times 10^{-1}$	$1,658 \times 10^6$	$1,433 \times 10^2$	$1,537 \times 10^{-1}$	$3,022 \times 10^5$	$2,612 \times 10^1$
10	$2,989 \times 10^{-1}$	$5,876 \times 10^6$	$5,080 \times 10^1$	$1,891 \times 10^{-1}$	$3,719 \times 10^5$	$3,215 \times 10^1$
11	$9,269 \times 10^{-1}$	$1,822 \times 10^6$	$1,575 \times 10^2$	$1,855 \times 10^{-1}$	$3,648 \times 10^5$	$3,153 \times 10^1$
12	$9,419 \times 10^{-1}$	$1,852 \times 10^6$	$1,601 \times 10^2$	$1,192 \times 10^{-1}$	$2,344 \times 10^5$	$2,027 \times 10^1$

Table 17 - WO parameter values

4.4.2 – AC Plasmas at ISTTOK

Initially the number of semi-cycle that was tested was 10 (Figure 55), but then the number was expanded till 40 (Figure 56 and Figure 57).

The signals acquired and integrated are due to AC Plasmas, as it can be seen by the figure below.

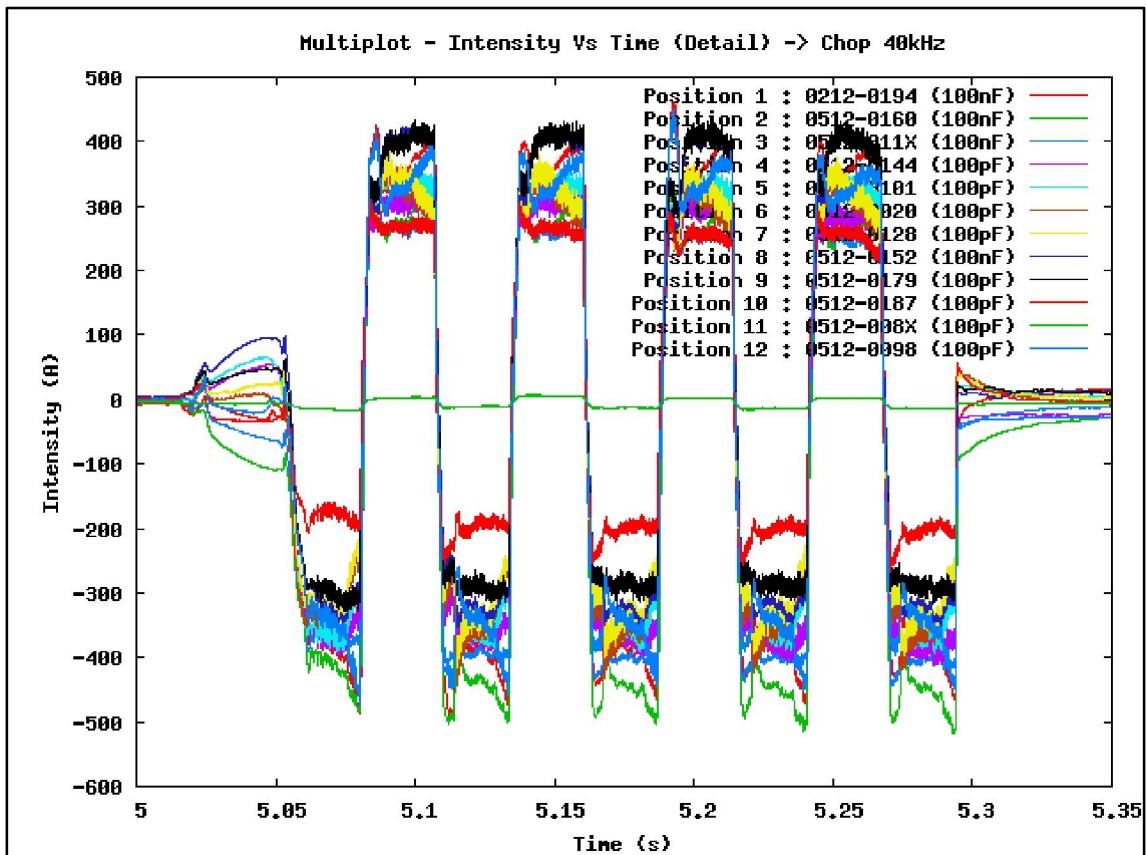


Figure 55 - Intensity of the signal from all coils in detail, on the beginning this graphic the values of the integral were set to zero

In Figure 55 it is seen that there are 10 semi-cycles during the experiment, the first semi-cycle is not well defined because it was not successfully gathered all the needed conditions to have the normal ionization of the gas but the following semi-cycles were successful. This can happen because each time

one field inversion (the start of a new semi-cycle) is not done successfully it is tried that the gas within the tokamak is re-ionized again.

The time of the discharge was extended comparing with the last sub-chapter, passing from a duration of about 25-30 ms to 250 ms. But recently the ISTTOK fast control system was updated in order to improve the AC discharges performance. Below is presented the results of an AC plasma discharge that lasted more than 1s, with 40 semi-cycles without apparent degradation of the plasma parameters (Figure 56 and Figure 57).

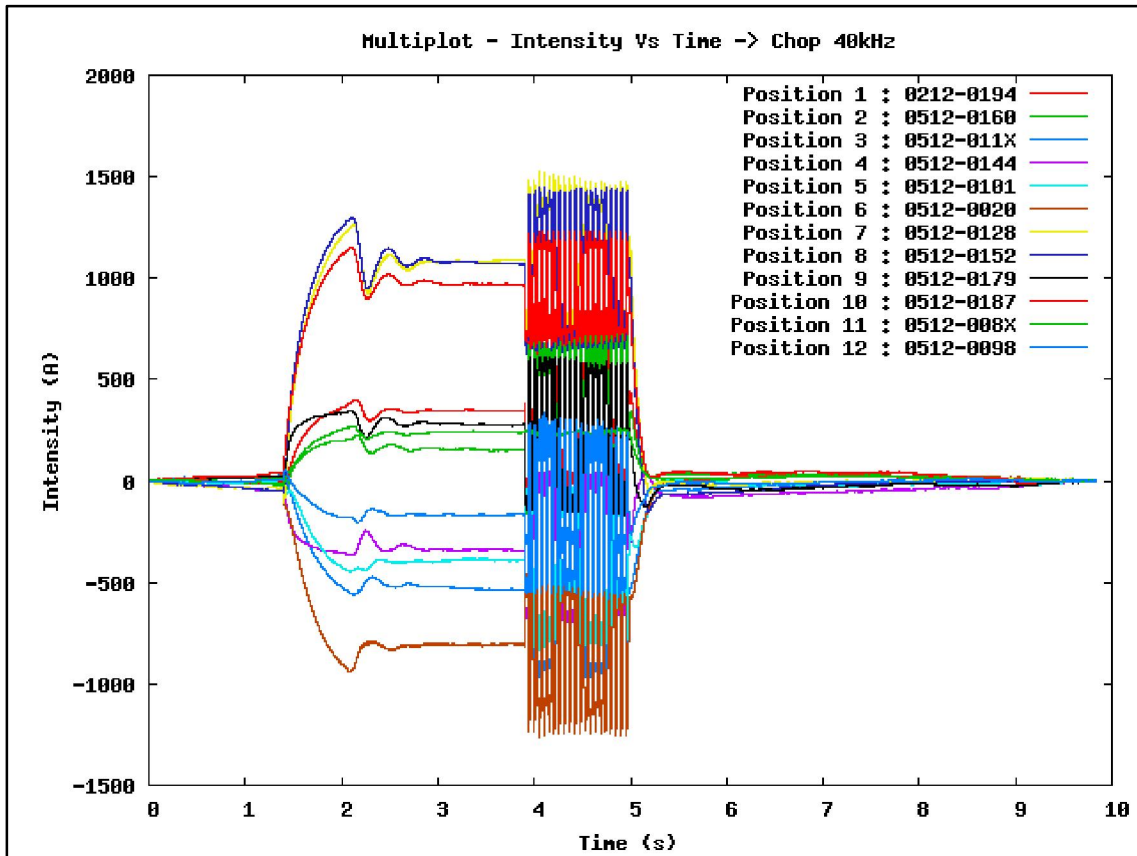


Figure 56 - Intensity of the signal from all coils, for the full ISTTOK cycle

Figure 56 shows that the AC plasma discharge had been done for the most time that was allowed because the end of the AC discharge almost matched with the instant that the toroidal field stopped being produced.

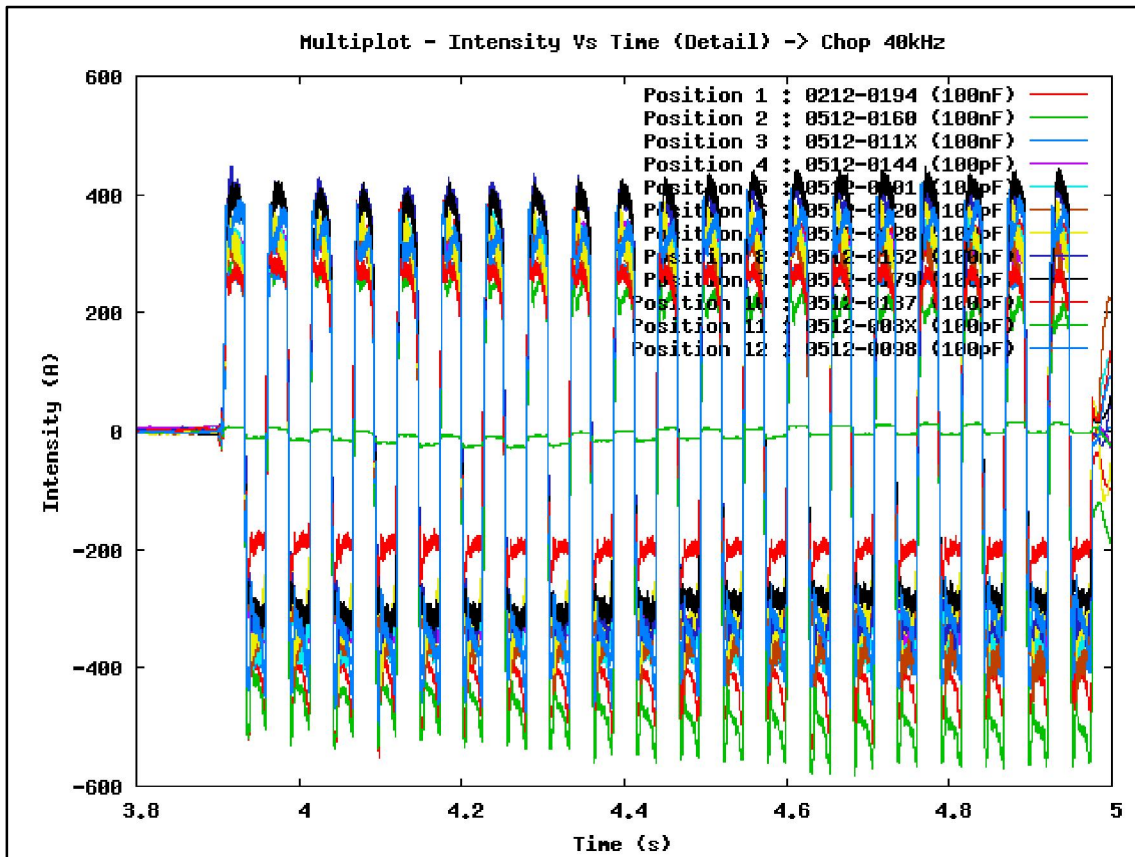


Figure 57 - Intensity of the signal from all coils in detail, on the beginning this graphic the values of the integral were set to zero and the some of the signals were inverted

The average time of each semi-cycle discharge is about 28 ms and the total duration is above 1s.

4.5 – Acquisition tests at IPP, Greifswald

The objective was to demonstrate the performance of the ADC digital modules developed by the Instituto de Plasmas e Fusão Nuclear (IPFN) through tests in the Max-Planck-Institut für Plasmaphysik (IPP) at Greifswald, Germany.

Several tests were made as the integration of electronic noise and long acquisitions of 1000s of different signals from generators and from assemblies made. An assembly that was done in Germany had the purpose to simulate as real as possible the signals that would come from fusion devices. The performance of the modules and obtained results were as expected.

4.5.1 - First set of acquisitions: Acquisition of a short-circuited signal

Below are shown the obtained results of the noise integration during an acquisition of 1000 seconds of a short-circuited signal (Table 18).

	module	Offset EO (LSB)	Offset EO (uV)	1000 s drift WO (LSB)	1000 s drift WO (uV*s)	1 s Offset WO (uV)	Used Conversion (uV/LSB)
Channel1	0212-016X	-236	$-4,168 \times 10^4$	461687607	$4,077 \times 10^4$	40,77	176,619
Channel2	0212-0208	-180	$-3,166 \times 10^4$	431414022	$3,794 \times 10^4$	37,94	175,868
Channel3	0212-0054	-106	$-1,870 \times 10^4$	467295377	$4,123 \times 10^4$	41,23	176,441
Channel4	0212-0151	109	$1,916 \times 10^4$	232533783	$2,044 \times 10^4$	20,44	175,794
Channel5	0212-0070	-74	$-1,300 \times 10^4$	497652567	$4,370 \times 10^4$	43,70	175,620
Channel6	0212-0119	-601	$-1,058 \times 10^5$	491176349	$4,322 \times 10^4$	43,22	175,992
Channel7	0212-0097	-460	$-8,100 \times 10^4$	370767962	$3,264 \times 10^4$	32,64	176,088
Channel8	0512-0160	19	$3,353 \times 10^3$	462701747	$4,083 \times 10^4$	40,83	176,472
Channel9	0212-0194	-621	$-1,094 \times 10^5$	344891988	$3,037 \times 10^4$	30,37	176,103
Channel10	0512-011X	-239	$-4,200 \times 10^4$	257677878	$2,264 \times 10^4$	22,64	175,727
Channel11	0512-0152	-656	$-1,144 \times 10^5$	237742548	$2,072 \times 10^4$	20,73	174,348
Channel12	0512-0020	177	$3,089 \times 10^4$	393830408	$3,523 \times 10^4$	34,37	174,518
Channel13	0512-0179	-783	$-1,386 \times 10^5$	264708996	$3,528 \times 10^4$	23,43	177,011

Table 18 - Resume of EO and WO values

The obtained results are very similar to the ones obtained in Portugal, as it would be expected.

4.5.2 - Second set of acquisitions: Tests with a made assembly, simple voltage integration

Afterwards was implemented a simple assembly, using coils and a generator (Figure 58 and Figure 59). The specially purpose made coil had 20 loops of copper wire and a resistance of $\sim 0.12 \Omega$.

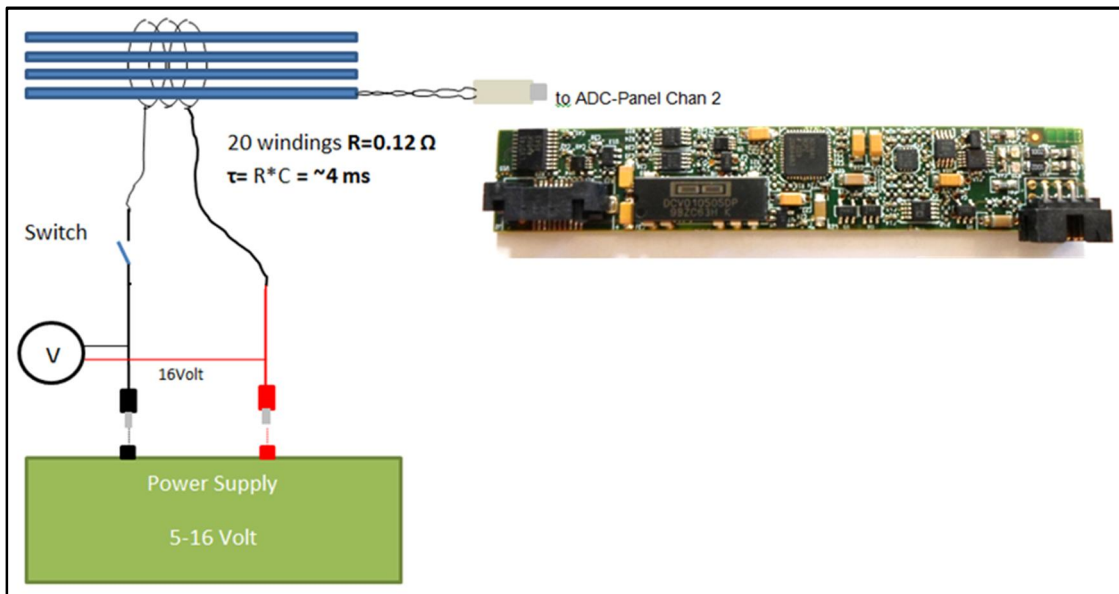


Figure 58 – Schematic of the first used assembly to test the performance of the module by generating a magnetic field with a DC generator

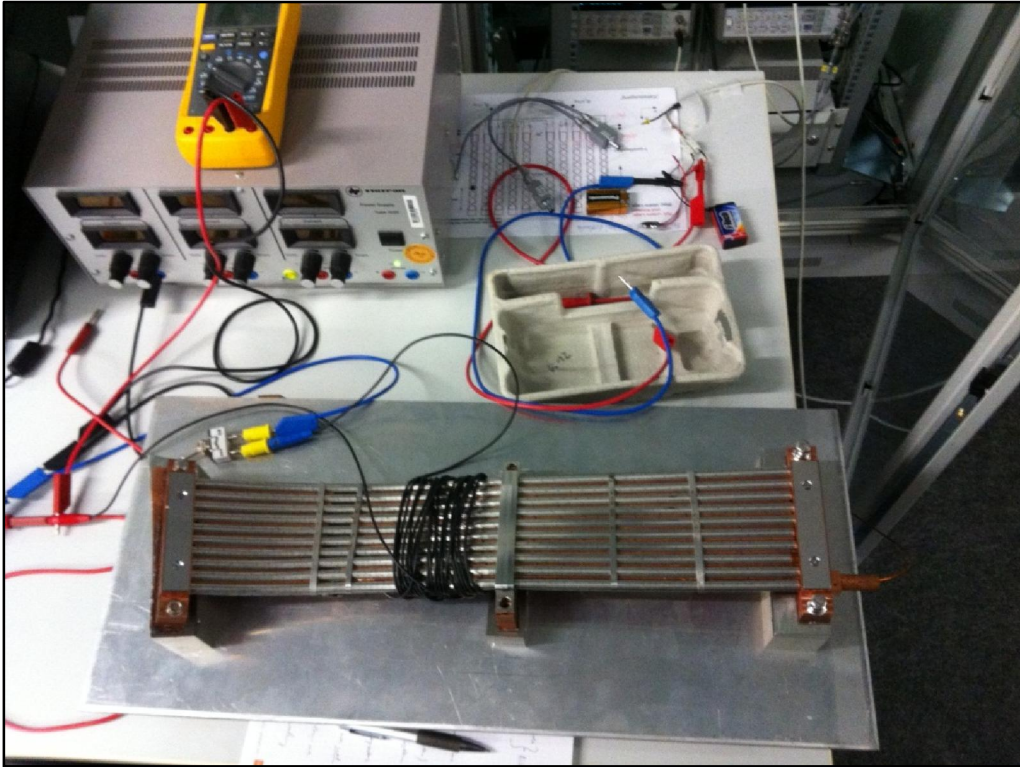


Figure 59 - First used assembly

By turning on and off a constant voltage from the DC generator with a simple switch the signal of the integrator should come nearby zero again. This is because the magnetic field is proportional to the current that is passing and if the current is zero then the magnetic field is zero also. The graphics Figure 60 (bellow) and Figure 86 (of the appendices) show good results about this first test.

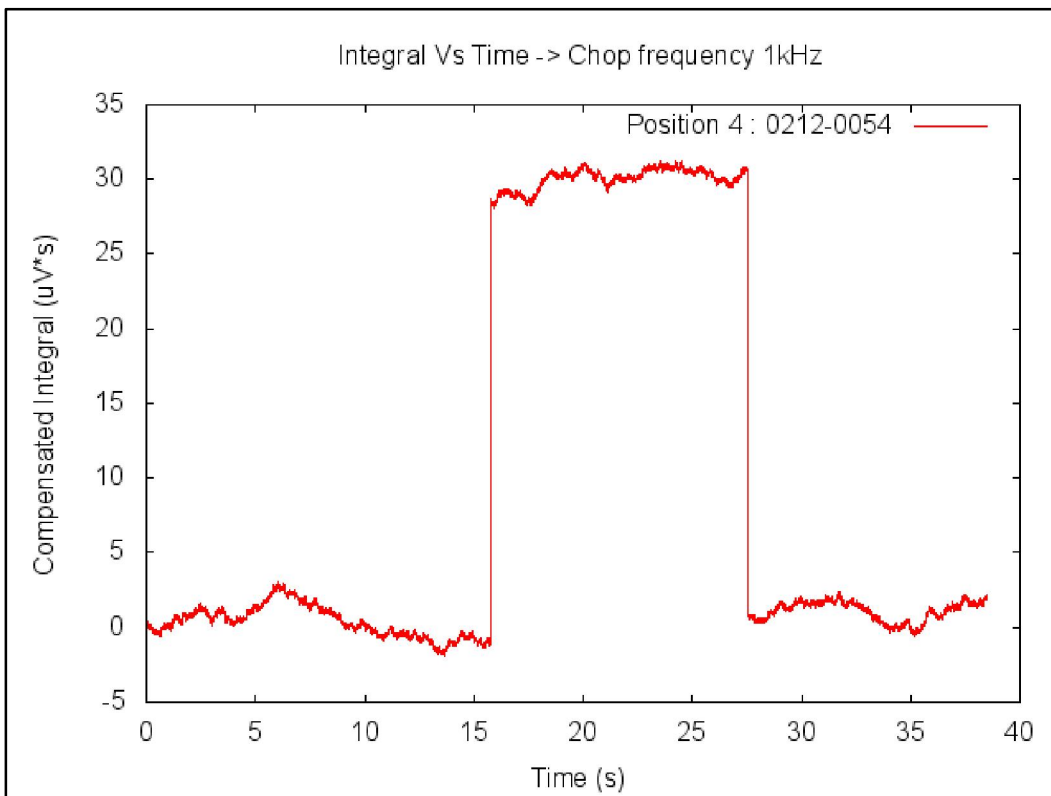


Figure 60 - Pre-Compensated Integral, the acquisition was during 40 seconds and the pre-compensation was done at 10 seconds

4.5.3 - Third set of acquisitions: Tests with a made assembly, integration of a capacitor discharge

The assembly was then changed and it was implemented a capacitor of 33mF with the coil of 20 loops and a resistance of 0.12 Ω, time constant about 4 ms (Figure 61).

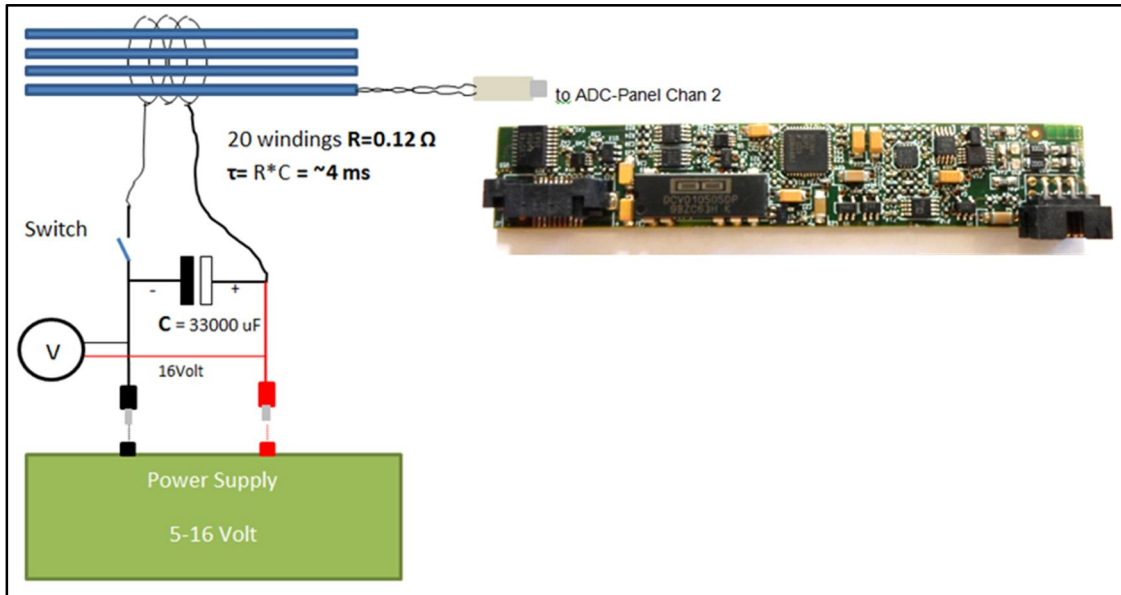


Figure 61 – Second used Assembly

The results of these acquisitions are shown, below is Figure 62 and at the appendices is Figure 87. The acquisition was a Pre-Compensated Integral at 10s. The total acquisition was of 40s.

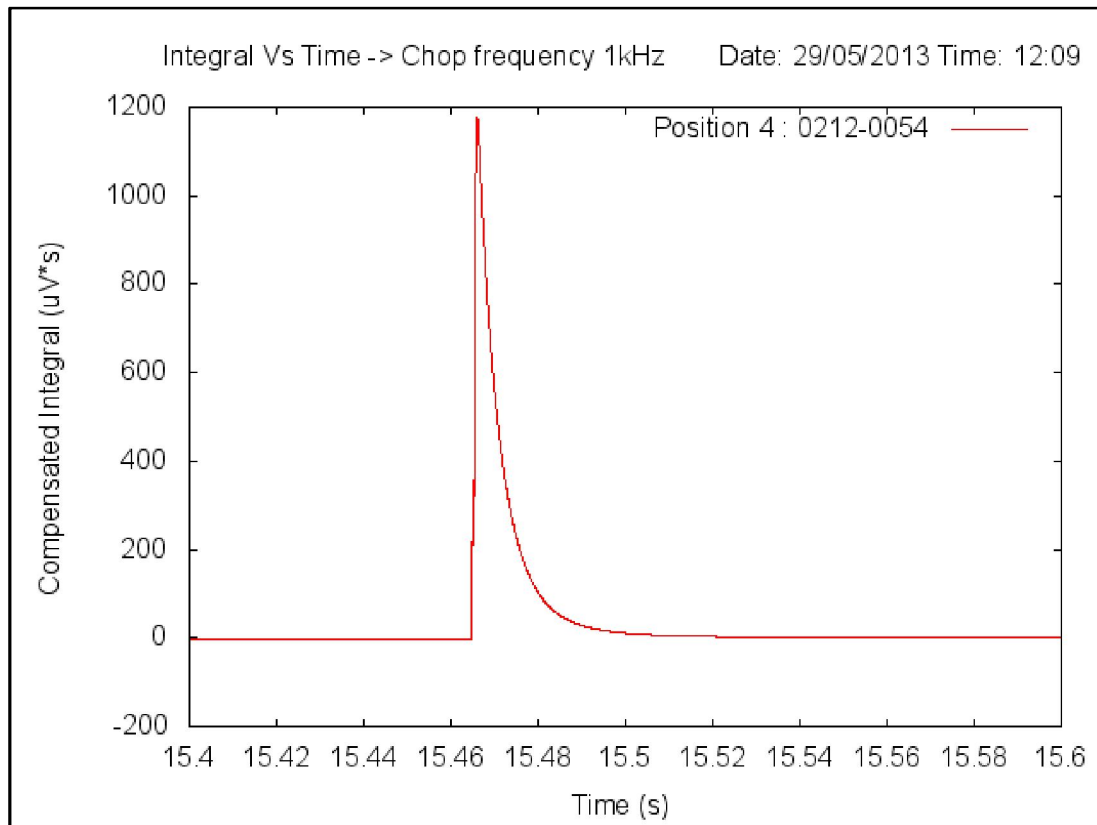


Figure 62 – Detail of a Pre-Compensated Integral, the acquisition was during 40 seconds and the pre-compensation was done at 10 seconds

With the data from the acquisition of the signal resulted from the capacitor discharge shown in Figure 62 was done a function adjustment using the program Origin Pro 8. It can be seen in Figure 63 that the obtained function parameters are similar to the calculated.

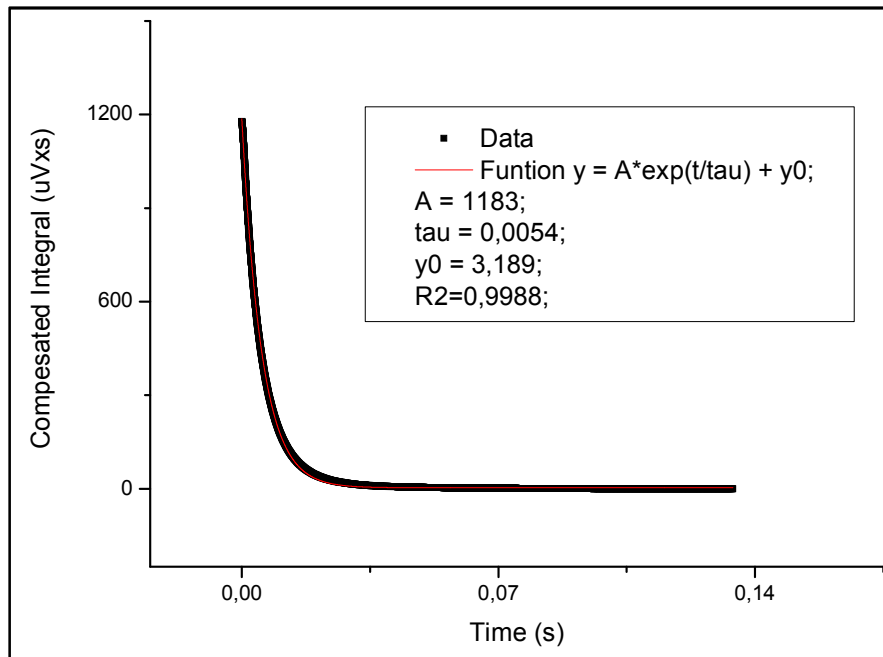


Figure 63 – Adjustment of an exponential function to the data presented in Figure 62

4.5.4 - Forth set of acquisitions: Tests with a made assembly, integration of a large number of capacitor discharge (>40), long acquisition of 1000s

A test during 1000 seconds was done, to see the response of the modules to a long Pre-Compensated Integration of 1000s (Figure 64).

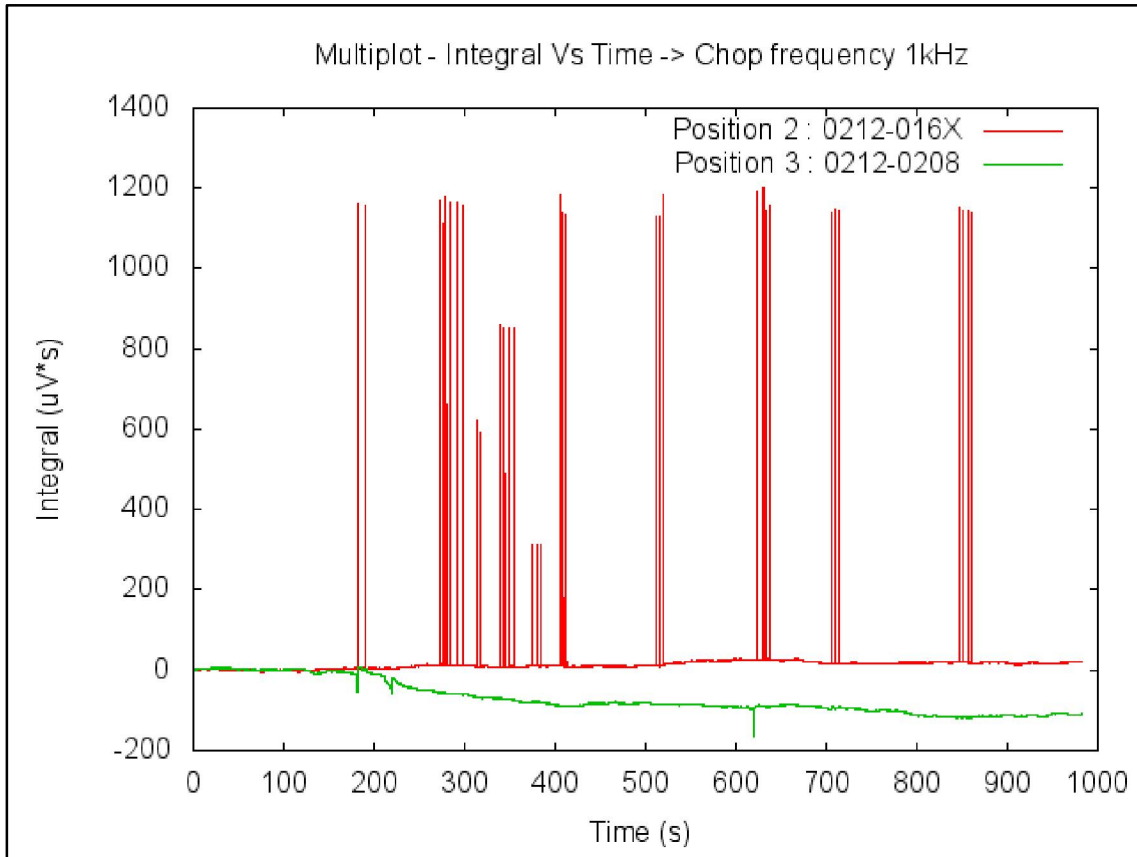


Figure 64 - Multiplot of Pre-Compensated Integral, the acquisition was during 1000 seconds and the pre-compensation was done at 100 seconds

Each red spike is a discharge of the capacitor, it can be seen that the last value of the integral is very small, less than 50 uV*s. This means that the long acquisition and integration during the capacitor discharges spikes went well and no data was lost.

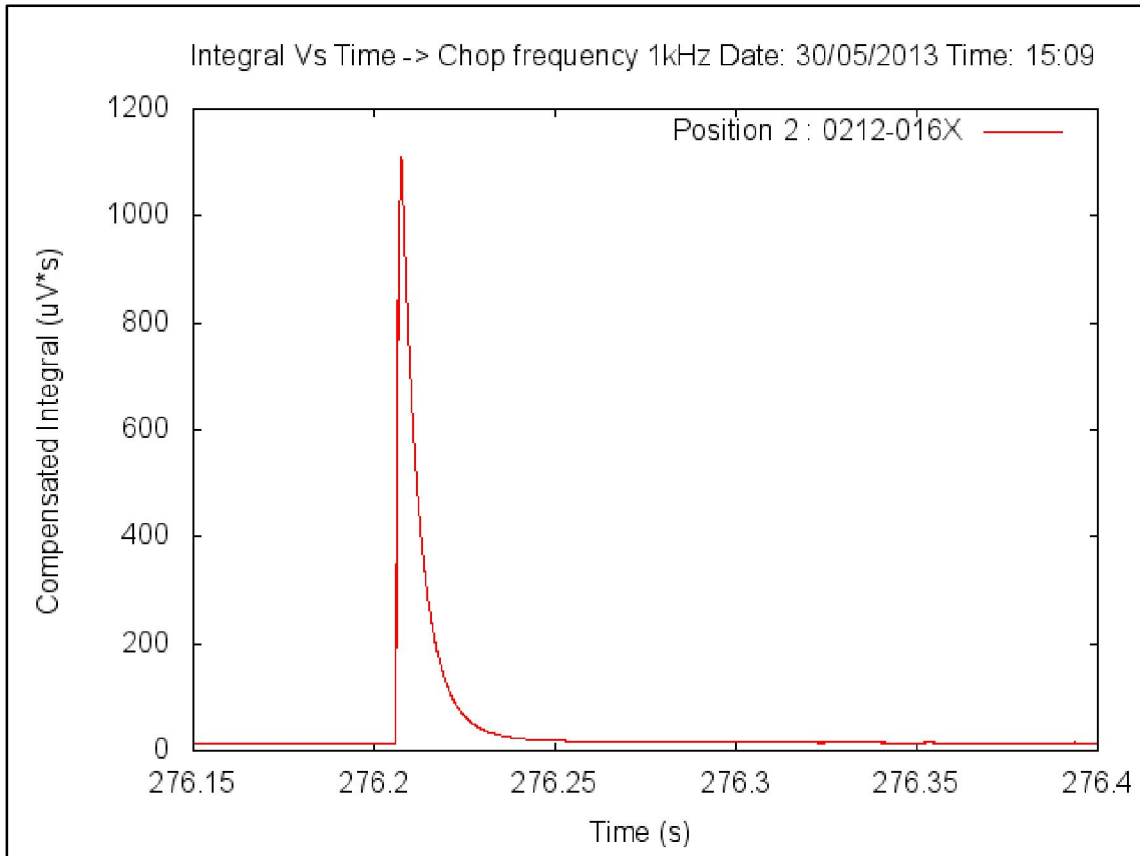


Figure 65 - Pre-Compensated Integral (detail), the acquisition was during 1000 seconds and the pre-compensation was done at 100 seconds

This test was done also to verify if there was a crosstalk between the modules, as it can be seen in Figure 64 there is no relation between peaks from the consecutive modules. The module in position 2 (0212-016X) was connected to the assembly while the module in position 3 (0212-0208) is short-circuited.

4.5.5 - Fifth set of acquisitions: Test performed in Portugal

Other test was asked to do in Portugal, an acquisition during 1000 s of a short-circuited signal but with a chop frequency of 10kHz. The results can be seen in Figure 66.

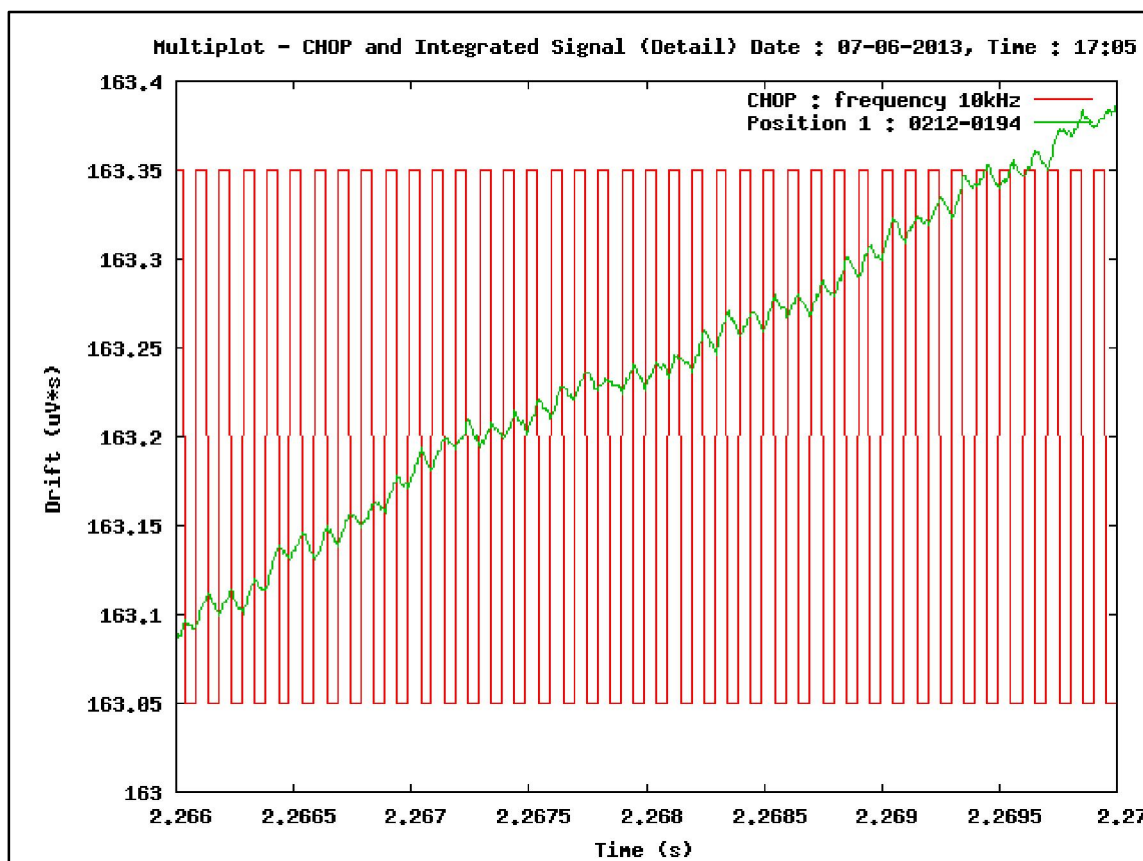


Figure 66 - Multiplot, detail of the Drift with the Chop signal

The Resume of the values for the Offsets can be seen below:

	module	Offset EO (LSB)	Offset EO (uV)	1000 s drift WO (LSB)	1000 s drift WO (uV*s)	1 s Offset WO (uV)	Used Conversion (uV/LSB)
Channel 1	0212-0194	-620	$-1,092 \times 10^5$	796955628	$7,017 \times 10^4$	70,17	176,103

Table 19 - Resume of EO and WO values

4.5.6 - Sixth set of acquisitions: Test performed remotely in Greifswald

A last test was done, a remote test at IPP, Germany. The acquisition was during 1000 s of a short-circuited signal, with a chop frequency of 10kHz. The results can be seen in Figure 67.

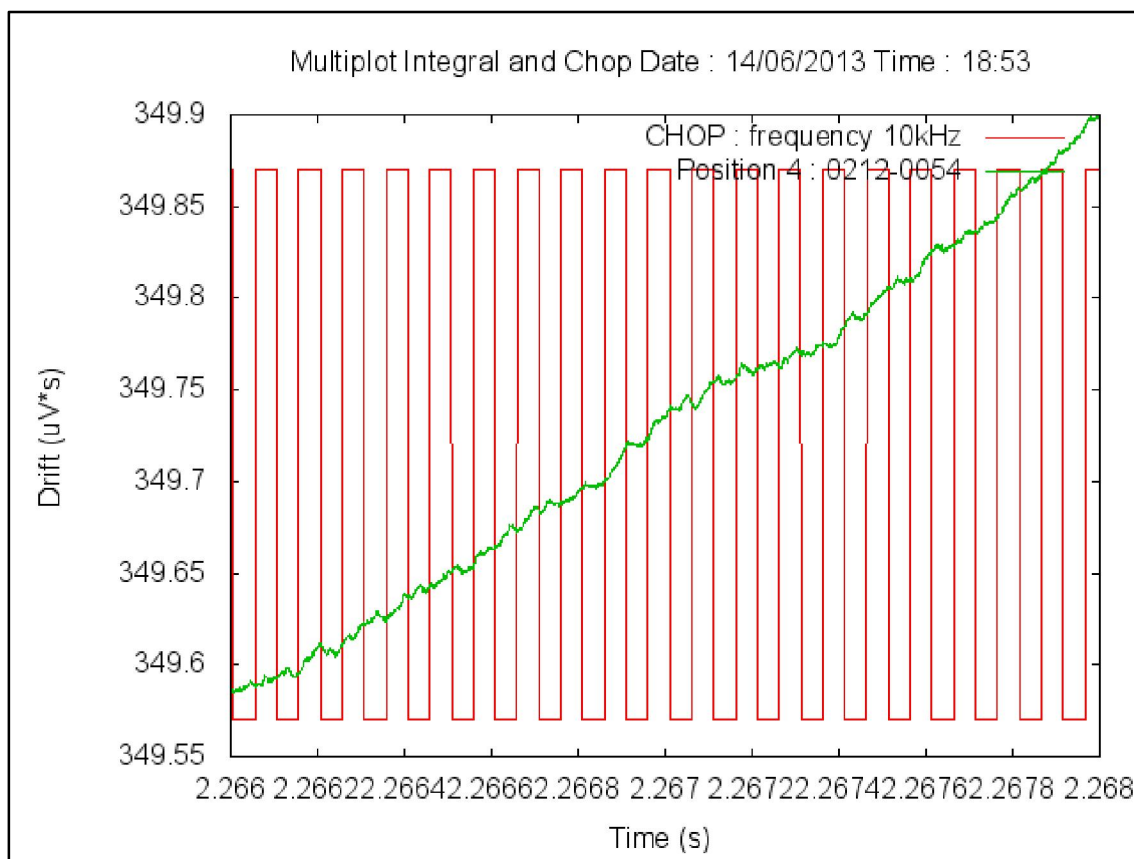


Figure 67 – Multiplot, detail of the Drift with the Chop signal

The Resume of the values for the Offsets can be seen below:

	module	Offset EO (LSB)	Offset EO (uV)	1000 s drift WO (LSB)	1000 s drift WO (uV*s)	1 s Offset WO (uV)	Used Conversion (uV/LSB)
Channel4	0212-0054	-112	$-1,976 \times 10^4$	1726715179	$1,523 \times 10^5$	152,3	176,441

Table 20 - Resume of Offset EO and Offset WO values

5 - Results and Discussion

5.1 – Introduction

On this chapter is presented the analysis and discussion of the results obtained and presented on the last chapter. It is first analyzed the EO and WO parameters values obtained in different acquisitions tests as well the drifts values. Afterwards is analyzed the effected of temperature on the integrated signals and suggested an algorithm to compensate this contribution. At last is analyzed the performance of the modules during the acquisitions in ISTTOK comparing with results from ISTTOK's Rogowski coil and during the tests at IPP, Greifswald.

5.2 – Noise acquisition and integration

In section 4.2 was seen that having the input of the ADC short-circuited there is undesired electronic noise, which will induce the integrals value to error. It was also shows that the result of a post compensated integration usually has less drift than a pre compensated integration.

The set of acquisitions with constant temperature have shown that the EO parameter it can be considered as being constant throw all the acquisitions, it has a variation of only 1 or 2 LSB. WO on acquisitions like this one, done consequently have not shown much difference as well, as it can be seen in Figure 68. It can be seen that the average value of the noise voltage is always smaller than one LSB.

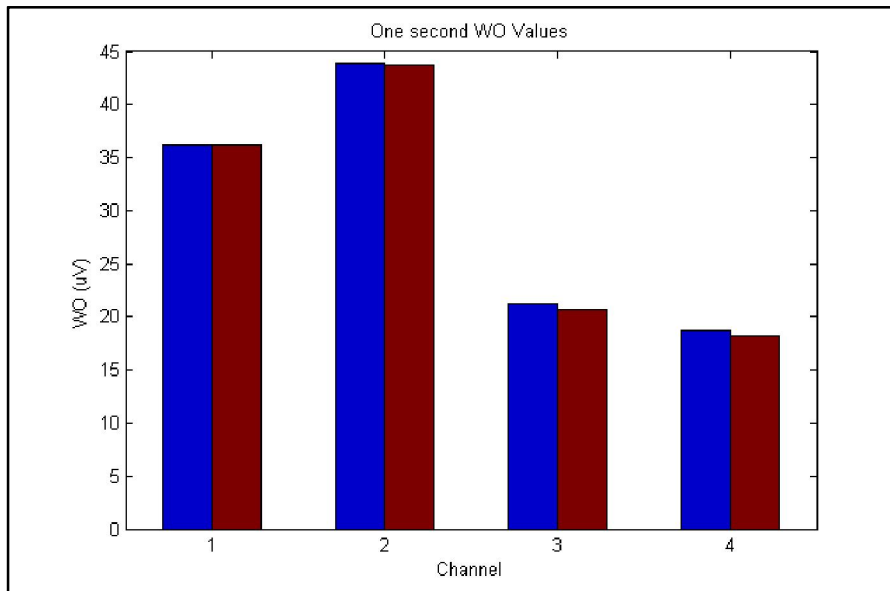


Figure 68 - Comparison between WO (or Before Chop Offset) values from different channels in two post compensated acquisitions with constant temperature

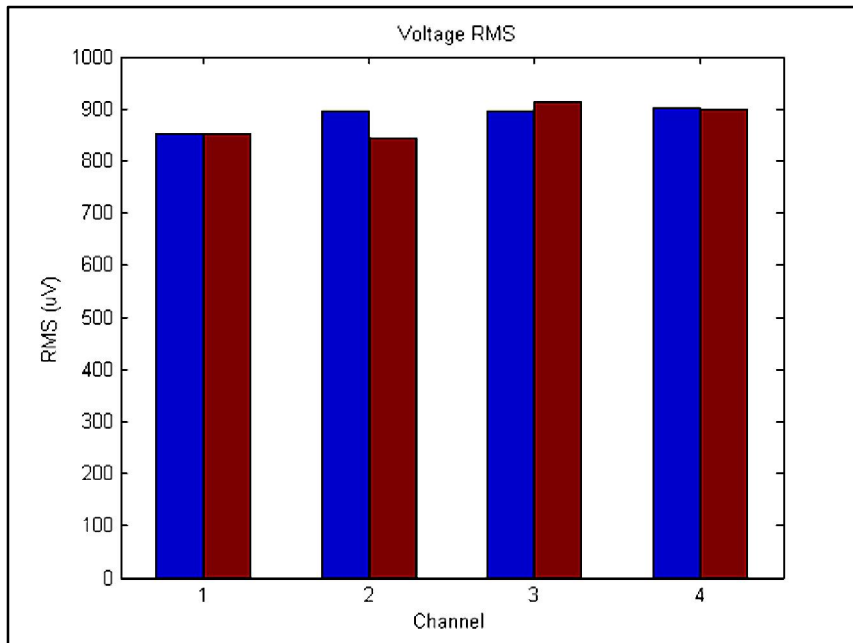


Figure 69 - Comparison between Offset's RMS from different channels in two post compensated acquisitions with constant temperature.

The best obtained values with acquisitions at constant temperature were less than 25 $\mu\text{V}\cdot\text{s}$ for a 1000s acquisition with post compensated drift and less than 50 $\mu\text{V}\cdot\text{s}$ with pre compensated drift.

The obtained results of this part were very similar with the results presented in the poster entitled as Implementation and test of a long-term phase-modulated input digital integrator for magnetics using an ATCA data acquisition system, which was presented in the 27th Symposium on Fusion Technology – SOFT 2012, Belgium.

Comparing with some articles of the area [3] [4], it can be seen that obtained results are better than the results demonstrated by the analog symmetric integrators of Tore Supra ($< 135\mu\text{Vs}@1000\text{s}$). And they are similar to the ones obtained in W7-X ($\sim 30\mu\text{Vs}@1000\text{s}$).

It was done a study about the correlation of the noise integration, the results can be seen in the appendices at Figure 89, Figure 90 and Figure 91. These results show that there does not seem to be a pattern that is repeated from acquisition to acquisition (the distribution of the integral of a short-circuited acquisition noise is aleatory).

To study the temperature effect on the integral it was only used pre compensated acquisitions. The temperature variation performed during the acquisition had a tremendous effect on the integral and the obtained results by repeating the experiment are similar, as it can be seen in Figure 70 and Figure 71.

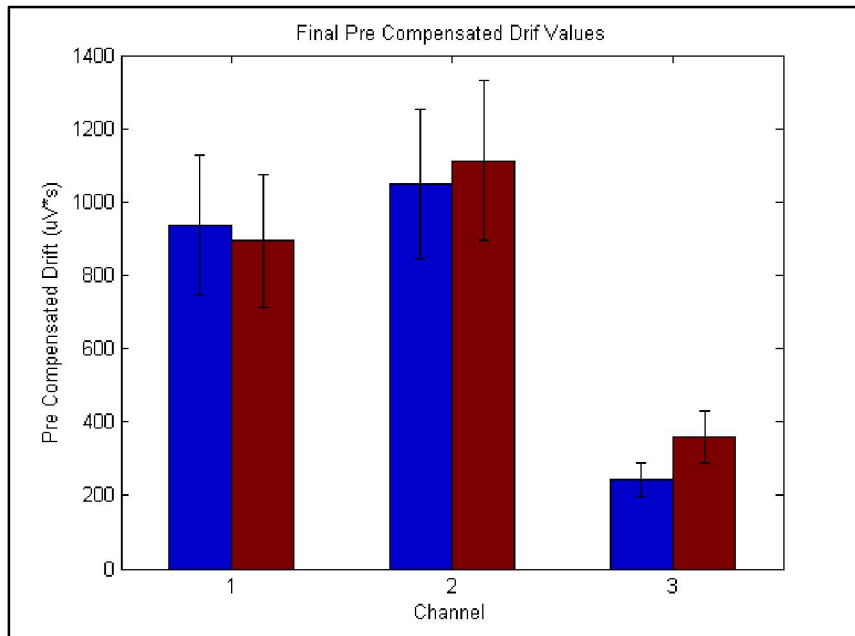


Figure 70 - Final Pre Compensated Drift Values of acquisition 3a and 3b (acquisition with temperature variation)

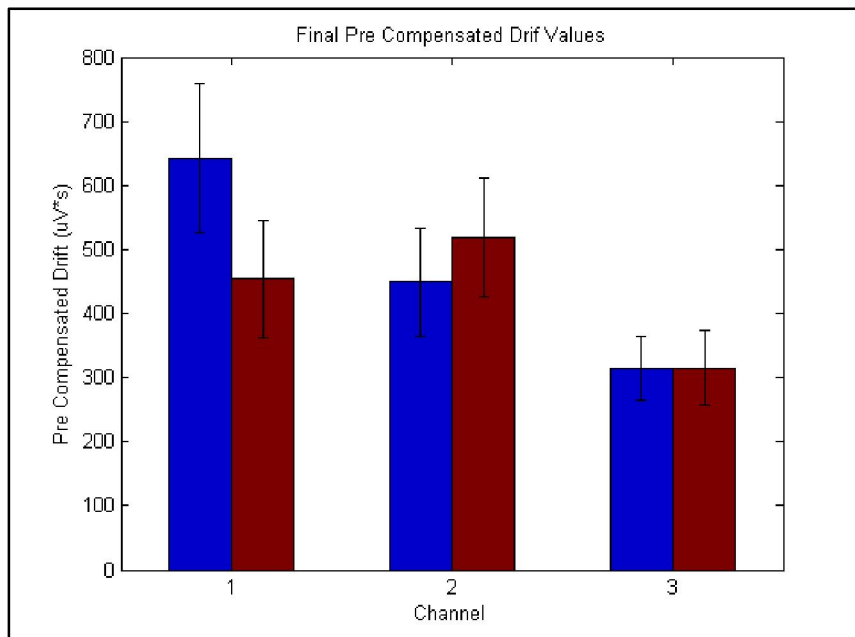


Figure 71 - Final Pre Compensated Drift Values of acquisition 4a and 4b (acquisition with temperature variation)

The final values of the long pre-compensated integrals with temperature change that are shown can differ in some cases, a possible explanation for this is that the conditions that were induced during the acquisition process were not the same. The local where the tests were made was not an isolated area and there were more people working and with the constant opening and closing of doors the temperature of the room could be changed. Another factor that could influence the results is that the ATCA crate has a cooling system and during the heating with the air gun it tries to compensate the elevation of the temperature. The way that the module were heated may not have been the best due to the directing of the heat to the modules might not have been the same leading perhaps to a contribution to the small variation of the final integration that was obtained as well.

The similar final value of the integration drift of pre-compensated acquisitions from several modules suggests that there is a relation between the temperature and the noise that can be predictable. One of the possible ways to continue this work is by studying a way to make real time corrections on the integration based on temperature sampling. A study for a first algorithm to compensate the influence of the temperature on these modules was made.

5.2.1 – Temperature tests and analysis

In Section 4.3 was seen the effect that the temperature variation could have in the electronic noise (in Figure 44 is visible the change in the Voltage values presented by the modules during the heat). To analyze better the temperature effect was done the RMS Evolution through time (Figure 72 and Figure 88). It is seen that during the heating the data send by the modules, whose terminals are short-circuited, are more dispersed (higher values are presented), the electronic noise is bigger.

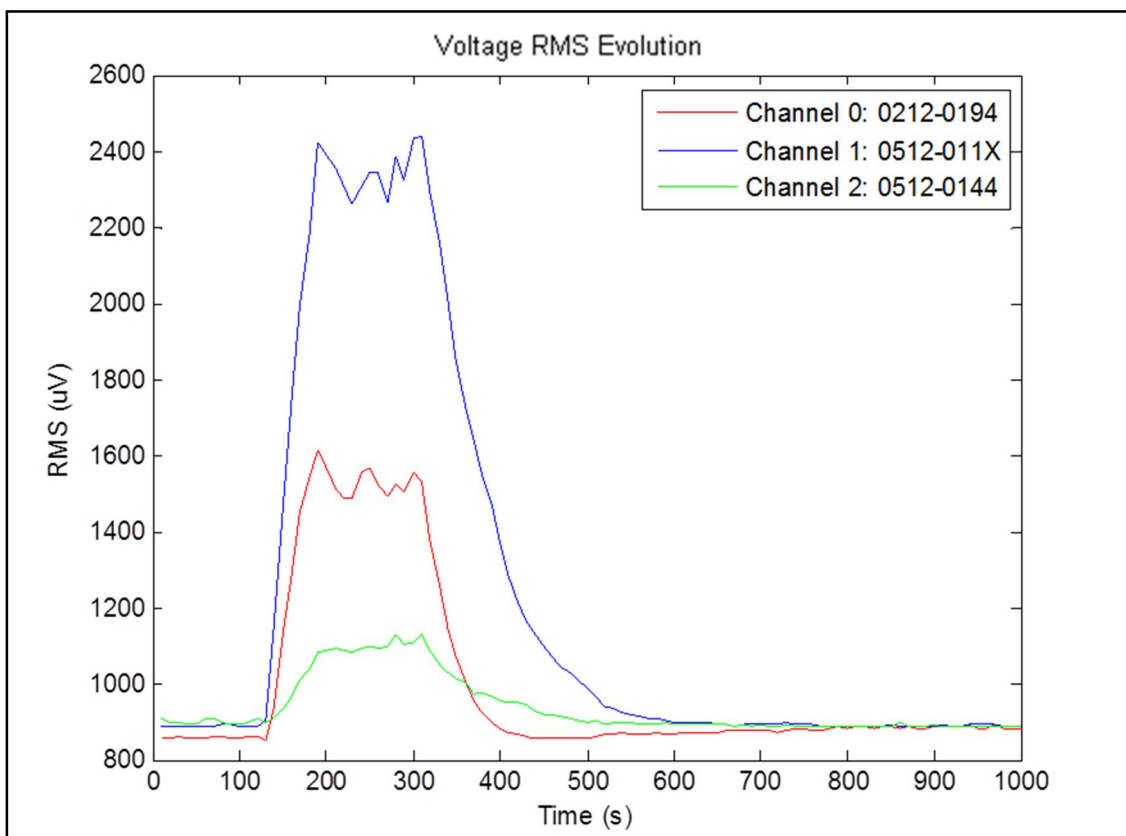


Figure 72 - Values of the voltage RMS through the acquired data during acquisition 3a, (acquisition with temperature variation)

As it was seen in Chapter 4.3, in this work it is suggested that there is a relation between the temperature and the noise that can be predictable. It was done the integral of the temperature values and the scale of the integral of the temperature was set so it could better adjust to the compensated integral of one the modules, as it can be seen in Figure 73 and Figure 74.

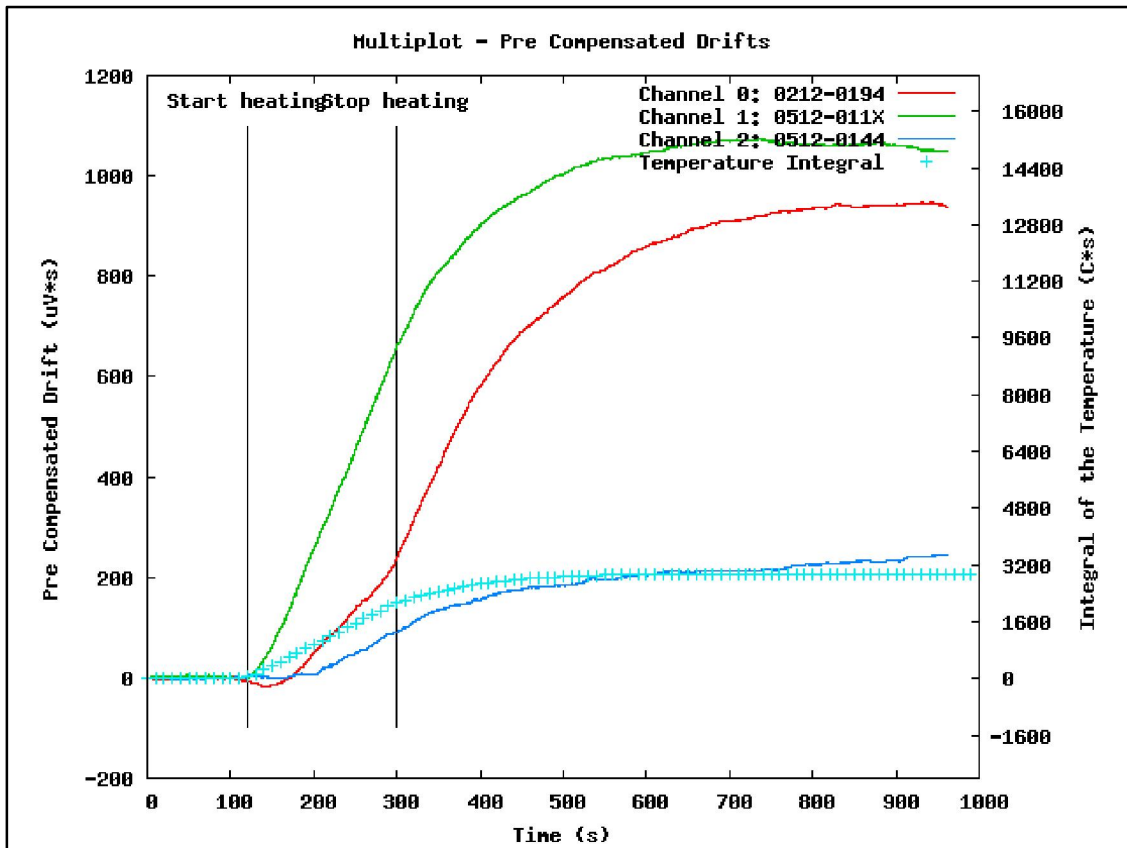


Figure 73 - Multiplot of all Pre Compensated Drift on acquisition 3a with the integral of the temperature

On the above figure the module 0512-0144 (blue line) is a different module of the other two modules, the main difference is a capacitor on the first low filter, instead of been a capacitor of 100nF is a capacitor of 100pF. The rest of the graphics related these tests can be seen in the Appendices, from Figure 92 to Figure 103.

It can be seen, in Figure 73, that there is a delay between the times in which the influence of the temperature start being shown on the different modules. This initial temperature impact is seen by the early rise of the integral drifts after the modules being heated.

An explanation for the time delay that is verified on the integral drift between different integrators is that some of the used components are not the same from module to module. They have also different casing that uses distinct materials. These differences might delay the influence of the temperature on the modules causing the shift in time that is seen. Other factor that may explain these results is that the used method to warm the modules was not the best. The flux of air could be more intense in different points of the ATCA board due to the positioning of the hot air gun and so distinct modules were influenced by the hot air gun differently.

It is being planned in the next future to repeat some tests using different methods to heat the modules to try to have a more homogeneous heating of the modules and so some of the these hypothesis will be tested.

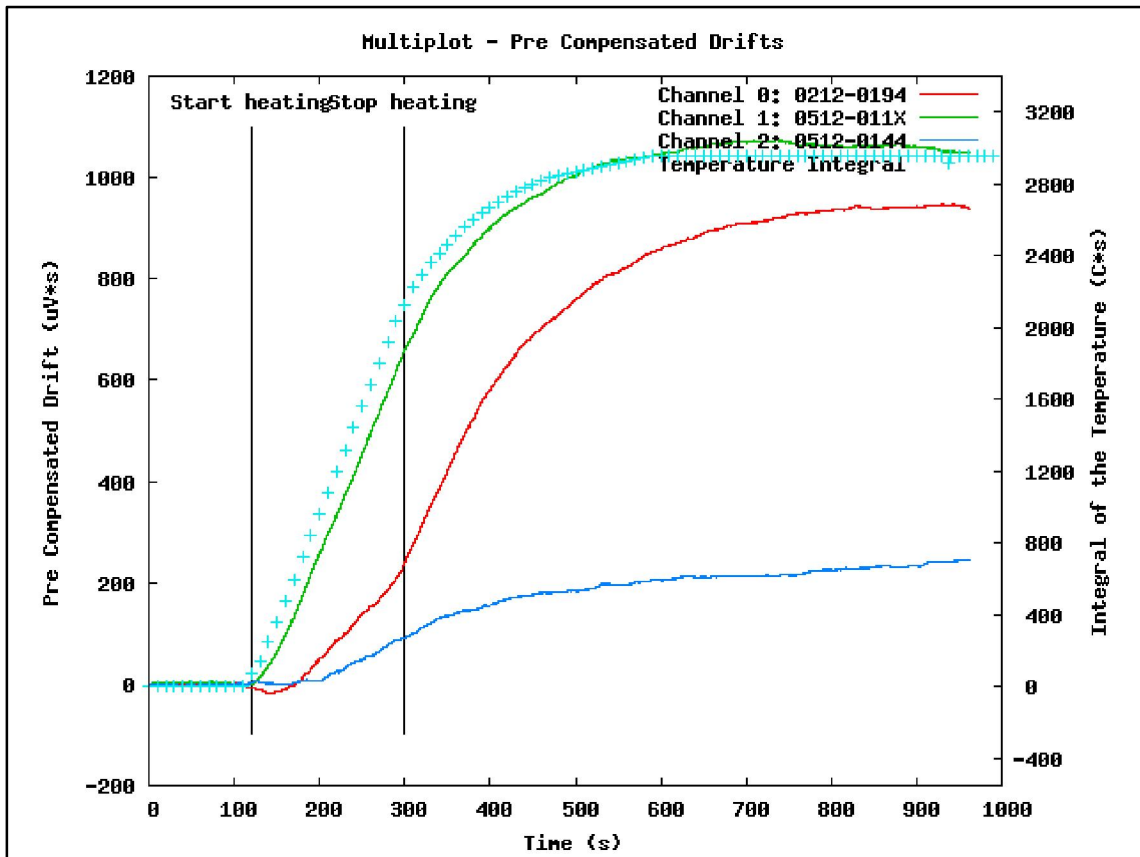


Figure 74 - Multiplot of all Pre Compensated Drift on acquisition 3a with the integral of the temperature

It could be implemented in the FPGA a correction that would be applied directly on the values before they entered in the integral.

The correction factor needed due to the temperature influence could be calculated by the final values of the noise integral and the final values of the temperature integral. For example using the data presented by Figure 74:

$$\int \text{Signal} / \int \text{Temperature} = 1048 [\text{uV} * \text{s}] / 2960 [^{\circ}\text{C} * \text{s}] \quad (17)$$

$$\int \text{Signal} / \int \text{Temperature} = 0.3541 [\text{uV}/^{\circ}\text{C}] \quad (18)$$

Or

$$\int \text{Signal} / \int \text{Temperature} = 2.048 \times 10^{-3} [\text{LSB}/^{\circ}\text{C}] \quad (19)$$

A summary of the calculated correction factors can be seen in Table 21 and in Table 22:

Aquisition	Module	Channel	Integral Final (uV*s)	Temperature Integral Final(°C*s)	uV/°C	LSB/°C
3a	0212-0194	0	938	2960	0,3169	$1,833 \times 10^{-3}$
	0512-011X	1	1048	2960	0,3541	$2,048 \times 10^{-3}$
	0512-0144	2	244	2960	0,08243	$4,770 \times 10^{-4}$
3b	0212-0194	0	895	3080	0,2906	$1,681 \times 10^{-3}$
	0512-011X	1	1112	3080	0,3610	$2,088 \times 10^{-3}$
	0512-0144	2	360	3080	0,1169	$6,760 \times 10^{-4}$
4a	0512-0101	0	642	2770	0,2318	$1,340 \times 10^{-3}$
	0512-0012	1	450	2770	0,1625	$9,400 \times 10^{-4}$
	0512-0144	2	314	2770	0,1134	$6,560 \times 10^{-4}$
4b	0512-0101	0	454	2900	0,1566	$9,050 \times 10^{-4}$
	0512-0012	1	518	2900	0,1786	$1,033 \times 10^{-3}$
	0512-0144	2	316	2900	0,1090	$6,300 \times 10^{-4}$

Table 21 – Resume of the calculated temperature correction factors

Module	Type of Module	Average correction factor (uV/°C)	Average correction factor (LSB/°C)	Deviation %
0212-0194	100nF	$3,038 \times 10^{-1}$	$1,757 \times 10^{-3}$	4,33
0512-011X	100nF	$3,576 \times 10^{-1}$	$2,068 \times 10^{-3}$	0,97
0512-0144	100pF	$1,054 \times 10^{-1}$	$6,098 \times 10^{-4}$	21,77
0512-0101	100pF	$1,942 \times 10^{-1}$	$1,123 \times 10^{-3}$	19,38
0512-0012	100pF	$1,706 \times 10^{-1}$	$9,865 \times 10^{-4}$	4,71

Table 22 - Resume of the calculated temperature correction factors and its deviation

With this result (Table 21 and Table 22) and with the results that are shown in the Appendices it is suggested that the modules with the 100nF capacitor are more sensible to the temperature variation, once the average correction factor is higher. The tables above show also that the deviation of the temperature correction factor for the modules of 100nF is less than for the modules of 100pF.

The results that are presented in the Appendices from Figure 92 to Figure 103 suggest that the data from the temperature integral is more easily adjustable to the drift curve of the modules with the 100nF capacitor. Using the last statement and the ones from the last paragraph it could be said that the best modules to work with the temperature adjustments would be the modules with the 100nF capacitor.

IPFN has currently a project with new ADC modules designed for the new ATCA board [25] that include a temperature sensor with a resolution of 1/4 of a Celsius degree. This can compensate online the temperature effect on the modules during long integrations.

5.3 - Acquisition of signals from ISTTOK's Mirnov coils

5.3.1 – Plasma current results

The plasma current from an AC discharge of 40 semi-cycles that lasted more than one second is represented in Figure 75. It was obtained by adding the signals from the Mirnov coils of a section of ISTTOK and multiplying by a conversion constant. The value of the integral at the end of the discharge is nearly 0, as at the beginning of the discharge, this means that the “integration problem” was well compensated.

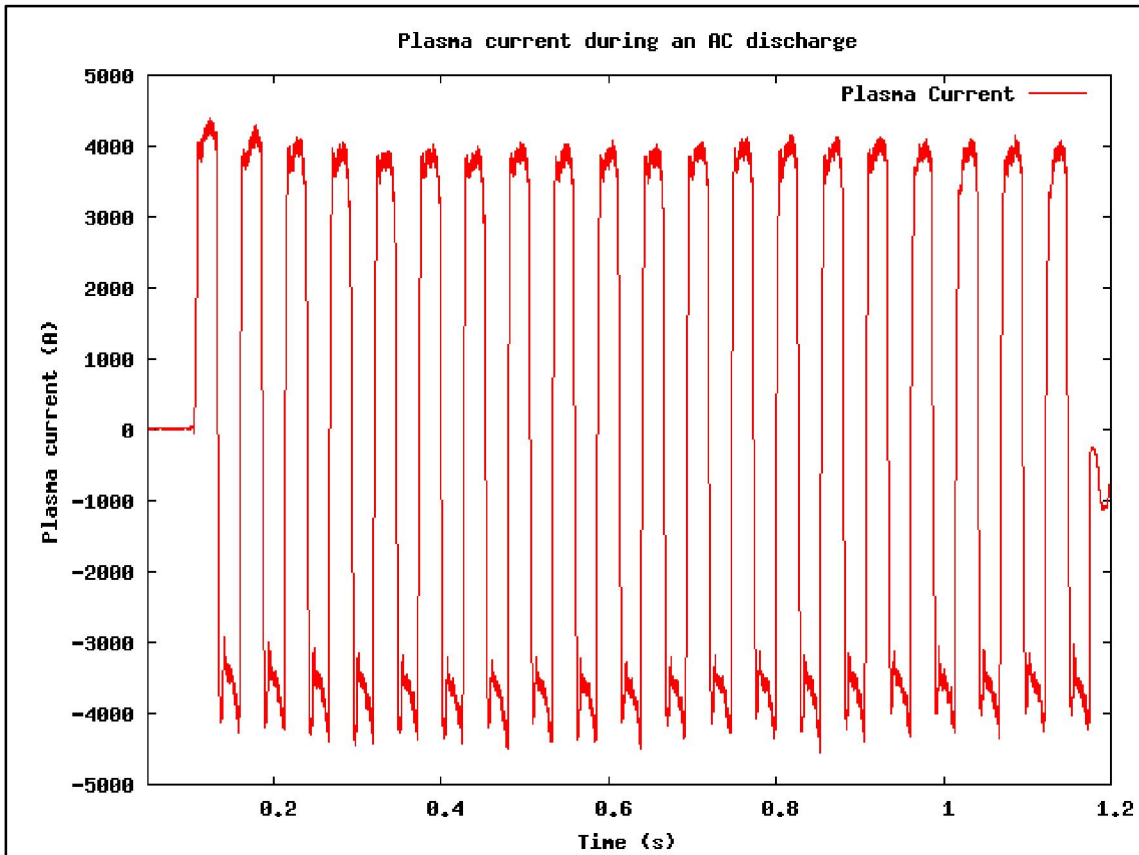


Figure 75 - Plasma current along time from ISTTOK measured by the Mirnov Coils, shot number 34531

In Figure 76 is shown the plasma current from the same shot of Figure 75, designed as shot number 34531, but obtained by the integration of the signals coming from a Rogowski Coil by an analog integrator. Comparing the figures it is seen that there is a higher drift at the measurements done by the Rogowski Coil, due to the used digital modules and used algorithm. The main difference between the modules is that the modules connected to the Rogowski coil are not digital integrators with chopper mode and do not use the algorithm related to two offset (EO and WO) to clear the signal.

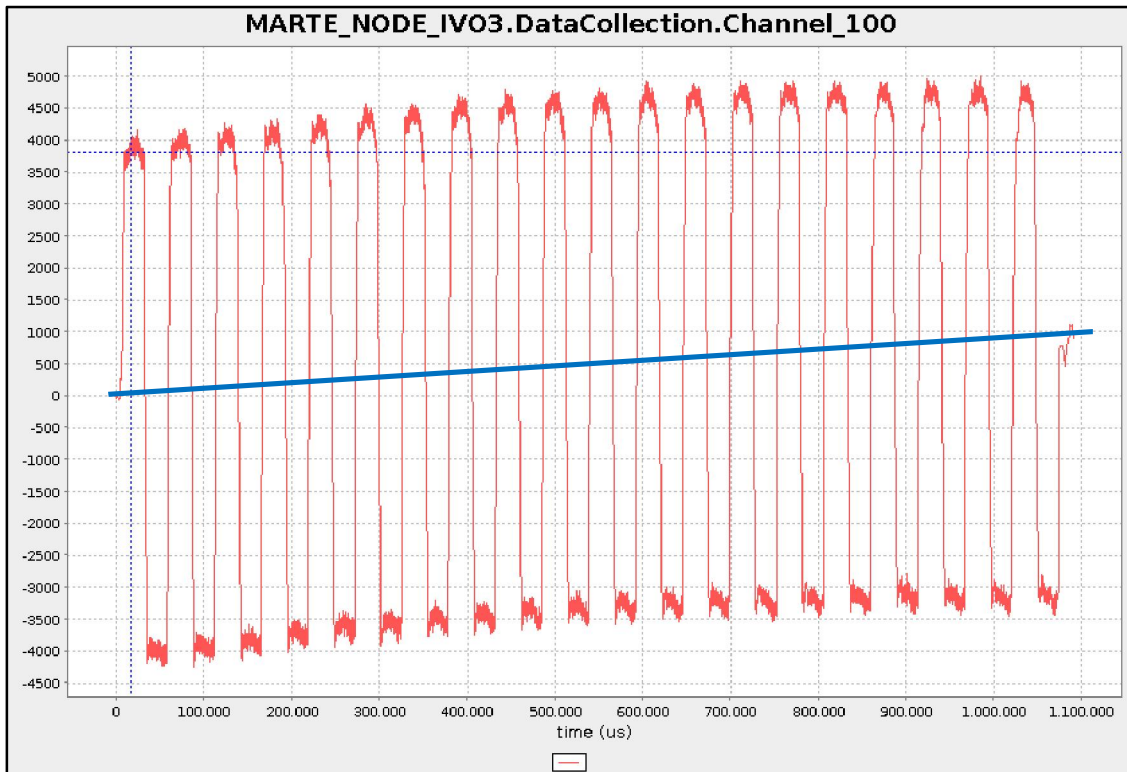


Figure 76 – Plasma current along time from ISTTOK measured by the Rogowski Coil, shot number 34531. The offset drift trend is shown in blue.

5.3.2 – Testing different Firmware Architectures

Different firmware architectures were used for this set of acquisitions, as mentioned in Chapter 3.

The first used FW version sent the signal voltage to the PC and the integration was done on a developed software application. The EO parameter was calculated by the Software using the first moments of the acquisition and then sent to the FPGA to be compensated. WO was calculated after the acquisition (post-compensation) or at the beginning using the first seconds of the test (pre-compensation) on the computer.

The best obtained results were with this FW architecture with a post-compensation integration, once it was used the first values and the last of the integration to calculate WO. The bigger is the integral sample to do the WO correction, the best will be the results. In this case with a post-compensated correction the drift will be minimum, because the final value of the integral would be set to zero.

The second FW architecture developed to ISTTOK had an algorithm which made the integration on the FPGA, the parameters EO and WO were sent by the Software at the beginning of the acquisitions. EO and WO they could be calculated using two methods:

On the SW, the first time interval was used to calculate EO, then the integral (at the FPGA) suffered a reset and it was done the calculations necessary to WO for a few seconds;

The software application would send at the beginning of the acquisition the values of EO and WO that had been previously calculated by using a post-compensated integration using the first FW architecture.

This FW has a flag sent by the SW that puts the integrals to zero (initialization), there is also an flag send from the FPGA to indicate if there was an overflow on the integrals.

It was done some acquisition with the module's input short-circuited as a test. The best results are represented below (Figure 77 and Figure 78), it can be seen that the values of integrated noise are small.

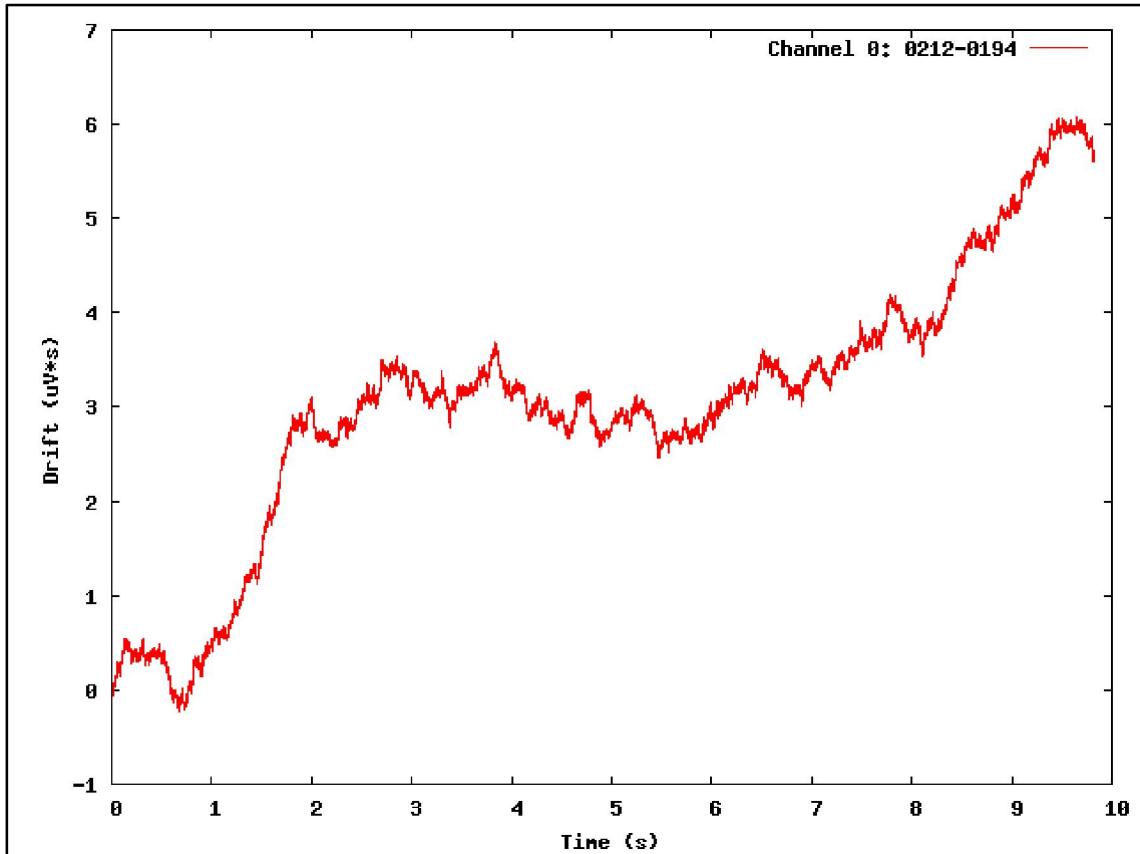


Figure 77 - Drift of a channel after the corrections of EO and WO

Figure 77 shows an acquisition that was done using the Software codes that put the EO and WO values previously obtained at the beginning of the integration acquisition, it shows the best results of the two figures. In Figure 78 the used Software calculated EO and WO, the calculation of the parameters ended after 0.5 s (at that time a flag from the developed software application put the integrals to zero as it can be seen).

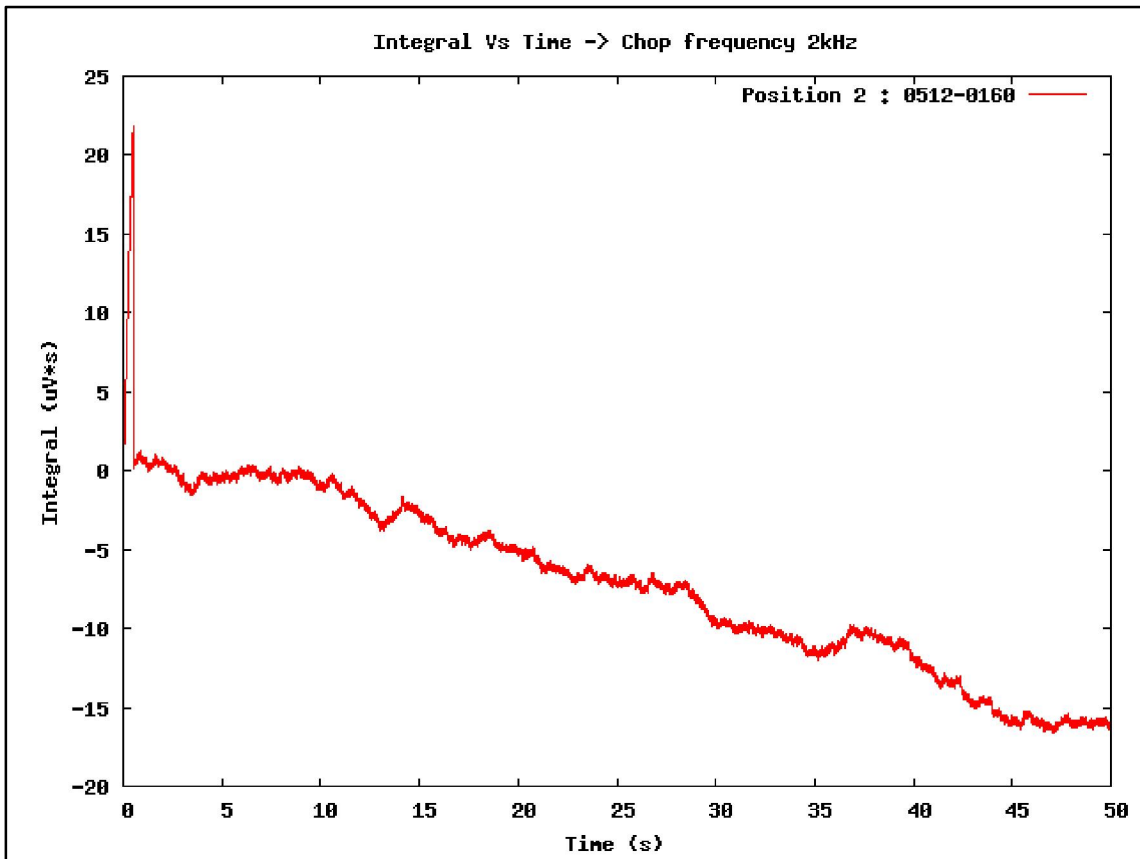


Figure 78 - Integral from a short-circuited signal
With this Firmware some acquisitions from AC discharges at ISTTOK were done, as it can be seen below (Figure 79):

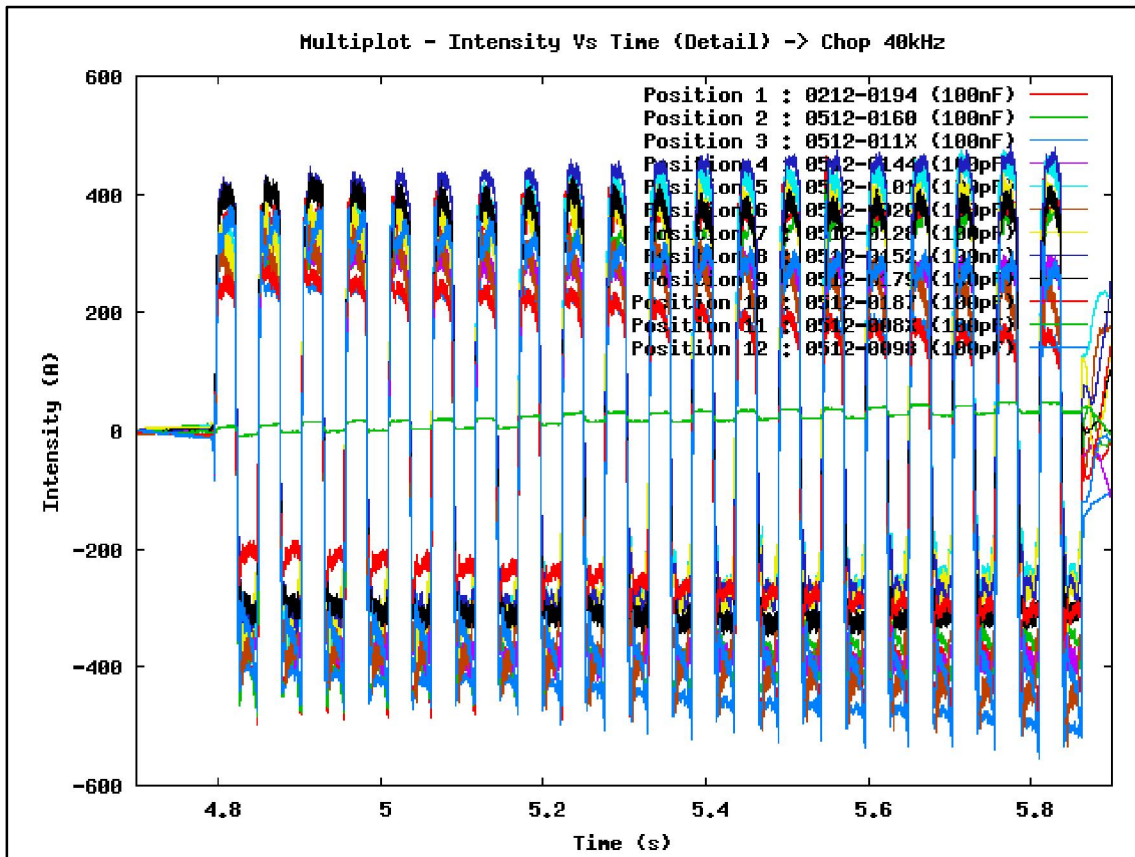


Figure 79 - Integrated Signal coming from the Mirnov coils, during an AC discharge (detail)

As it can be seen in Figure 79 these results obtained with the Firmware that calculates the integral in the FPGA are not as good as the previously shown (in Chapter 4.3.2), with a post-compensated integration calculated in Software, once the drift is bigger. This is because with the first architecture we do the data manipulation related to WO usually after the acquisition ended, it would be guaranteed that the final value of the integral would be set to zero.

With this second FW architecture and using the technique of calculating the parameter EO and WO at the beginning of the acquisition it could not be ensure that the integral drift would be minimum at its last values. And using the previous values of EO and WO earlier tests has the inconvenience that WO is influenced by several factors such a temperature (as proven before), once the calibration was done in a different time the temperature will be different so WO may be different.

There is another factor that might contribute to these results, the trigger used to start the acquisition was manually. I would press the key board at a certain time, which could induce a certain delay when to start the acquisition. This fact could induce error in the WO parameter, because the calculation could end after the action of the fields had begun (if using the last architecture and calculating EO and WO at the beginning of the acquisition).

There is an ongoing project to incorporate the needed with the MARTe [23] Framework (Multi-threaded Application Real-Time executor), there would not be any delay that compares with the one that was used (manually). The last referred problem that could happen using the second FW architecture, with the integral calculation inside of the FPGA, would not happen.

5.4 - Acquisition tests at IPP, Greifswald

Some of the tests performed in Germany had been done previous in Portugal. These tests that were repeated are the acquisition related to the acquisitions of short-circuited signals and it was presented very similar results to the ones obtained before, as it can be compared in Chapter 4.2.

The assembly was to simulate a magnetic environment for the acquisitions, it produced the wanted purpose and the results obtained were as expected and was demonstrate a good performance of the ADC digital modules. In Portugal these tests were not previously made and it was tested other aspects such as the crosstalk absence between modules.

The last performed tests were with different chop frequencies and it shows that the parameters of WO and EO were changed. In Table 23 can be seen the values comparison.

	EO (uV)	Average EO (uV)	Deviation EO %	WO (uV)	Average WO (uV)	Deviation WO %
Portugal (Chop 10k)	$-1,092 \times 10^5$	$-1,088 \times 10^5$	0,36	70,17	53,17	31,99
Portugal (Chop 1k)	$-1,084 \times 10^5$			36,16		
Greifswald (Chop 10k)	$-1,976 \times 10^4$	$-1,923 \times 10^4$	2,75	152,33	96,78	57,40
Greifswald (Chop 1k)	$-1,870 \times 10^4$			41,23		

Table 23 – EO and WO comparison, acquisitions with different Chop frequency

Above is seen that the EO parameter did not changed much with the increase of the Chop frequency (the deviation maximum is 2,75%), while WO had a big change (a maximum of 57,40 % of deviation). The results show that a big change on the Chop frequency it will certainly induce a WO change, as it suggests that WO will increase with a chop frequency increase.

The IPP team focused on the DAQ in magnetic diagnostics was satisfied with the performance of the modules from IPFN with the tests that were performed. Another visit was planned to the IPP to do tests with the ADC modules on a more realistic magnetic environment, with other assemblies. It was shown interest in testing as well another Firmware that was developed in the scope of this thesis, the Firmware were the integral is done inside of the FPGA.

6 - Conclusions

Nuclear fusion is a promising source of energy to support the increasing world demand. The development a new form of energy that is secure, non-polluting and sustainable is a huge scientific challenge. Several international and non-international projects have been done to study the necessary conditions to have nuclear fusion. The progress in the study of plasma confinement is so remarkable that the next generation device has a great potential to reach the ignition condition (with the ITER project).

Control and data acquisition systems are the set of the hardware and software that enables to do measurements and control processes, they are fundamental for the operation of fusion devices as tokamaks and stellarators. They constitute one of the most important fields to show the energetic viability that nuclear fusion has to offer.

In this thesis it was characterized several techniques and algorithms to have a clear signal of a magnetic diagnostic and it is described the performed tests and obtained results. The used modules were galvanic isolated digital modules developed by IPFN with signal chopper mode and a sampling at 2 MSPS (18-bit full precision data) and the used data acquisition architecture was ATCA. Some of the tests were done with simple made assemblies others with signals coming from tokamak ISTTOK.

A mission took place in the IPP at Greifswald (Germany), its objective was to demonstrate the performance of ADC digital modules developed by IPFN. The performed tests give the expected results.

There is a temperature dependency factor that influences the integrator drift. One of the possible ways to continue this work is by studying and implementing ways to make real time corrections on the integration based on temperature sampling. There are modules at the end of the development phase at IPFN that have incorporated temperature sensors with a resolution of 0.25 °C.

A second visit to the IPP at Greifswald was done in September 2013 to make new tests on the ADC modules with other assemblies, for testing their performance during the acquisitions on a more realistic external magnetic field environment.

As a final comment I would like to refer that this thesis with the results shown and with the mentioned involvement in projects and missions abroad is a demonstration that medium and small Laboratories from Portugal give important contributes to international projects worldwide. As IPFN has given in JET, IPP and have already agreements to the future participation at the ITER project.

7 - References and Bibliography

[1] B. Carvalho, “Controlo em Tempo Real do Tokamak ISTTOK”, Tese de Doutoramento, Instituto Superior Técnico, Lisboa, 2003.

[2] S Sudo et al, “Recent diagnostic developments on LHD”, Plasma Physics and Controlled Fusion, Volume 45, Number 7, 2003, doi:10.1088/0741-3335/45/7/307

[3] Pascal Spuig et al, “An analog integrator for thousand second long pulses in Tore Supra”, Fusion Engineering and Design, Volume 66-68, Pages 953-957, September 2003, [http://dx.doi.org/10.1016/S0920-3796\(03\)00382-X](http://dx.doi.org/10.1016/S0920-3796(03)00382-X)

[4] Andreas Werner, “W7-X magnetic diagnostics: Performance of the digital integrator”, Review Scientific Instruments, Volume 77, Issue 10, 2006, <http://dx.doi.org/10.1063/1.2220073>

[5] E. J. Strait, J. D. Broesch, R. T. Snider, and M. L. Walker, “A hybrid digital–analog long pulse integrator”, Review Scientific Instruments, Volume 68, Issue 1, pages 381-384, 1997, doi: 10.1063/1.1147835

[6] Vayakis, G. Et al, “Magnetic diagnostics for ITER/BPX plasmas (invited)”, Review Scientific Instruments, Volume 74, Issue 4, Abril 2003, doi: 10.1063/1.1534388

[7] Seo SH, Werner A, Marquardt M, “Development of a digital integrator for the KSTAR device”, Review Scientific Instruments, Volume 81, 123507, December 2010, doi: 10.1063/1.3519303

[8] W. M. Stacey, “Fusion, An Introduction to the Physics and Technology of Magnetic Confinement Fusion”, WILEY-VCH, 2007

[9] C. Varandas, “TECNOLOGIAS NUCLEARES PARA A PRODUÇÃO DE ENERGIAS ELÉCTRICA”, IST/IPFN, 2011

[10] John Wesson, “Tokamaks”, OXFORD SCIENCE PUBLICATIONS, 1985, first edition

[11] www.picmg.org/ [Acceded 2013/09/02]

[12] Hei Wong, “Low-frequency noise study in electron devices: review and update”, Microelectronics Reliability, Volume 43, Issue 4, Pages 585–599, November 2002, doi: 10.1016/S0026-2714(02)00347-5

[13] C. A. F. Varandas, B. B. Carvalho, C. Correia, H. Fernandes et al.. “A Fully Computerized and Distributed VME System for Control and Data-Acquisition on the Tokamak ISTTOK.” Nuclear

Instruments & Methods in Physics Research Section a-Accelerators Spectrometers Detectors and Associated Equipment, 349(2-3):547, 1994

[14] Ivo S. Carvalho, Paulo Duarte, Horácio Fernandes, Daniel F. Valcárcel, Pedro J. Carvalho, Carlos Silva, André S. Duarte, André Neto, Jorge Sousa, António J. N. Batista, Tiago Hekkert, Bernardo B. Carvalho, “ISTTOK real-time architecture”, Preprint submitted to Elsevier, May 1, 2013

[15] Ivo S. Carvalho, Paulo Duarte, Horácio Fernandes, Daniel F. Valcárcel, Pedro J. Carvalho, Carlos Silva, André S. Duarte, André Neto, Jorge Sousa, António J. N. Batista, Tiago Hekkert, Bernardo B. Carvalho, “Real-time control for long ohmic alternate current discharges”, Poster presented at the 9th IAEA Technical Meeting on Control, Data Acquisition, and Remote Participation for Fusion Research, China

[16] Jorge Sousa, Bernardo B Carvalho, Bruno Gonçalves, João Fortunato, António J N Batista and Carlos Varandas, “Implementation and test of a long-term phase-modulated input digital integrator for magnetics using an ATCA data acquisition system”, Poster presented at the 27th Symposium on Fusion Technology – SOFT 2012, Belgium

[17] Ivo S. Carvalho, Paulo Duarte, Horácio Fernandes, Daniel F. Valcárcel, Pedro J. Carvalho, Carlos Silva, André S. Duarte, André Neto, Jorge Sousa, António J. N. Batista, Tiago Hekkert, Bernardo B. Carvalho, Rui Gomes, “Real-time control for long ohmic alternate current discharges”, Preprint submitted to Elsevier, May 20, 2013

[18] A internal report was written, it can be seen at:
https://metis.ipfn.ist.utl.pt/svn/cdaq/ATCA/ATCA-IO-CONTROL/IPP/ADC_INTEGRATORS/Documentation/Reports

[19] F. Schauer, “Status of Wendelstein 7-X construction”, Fusion Engineering and Design, Volume 82, Pages 443–453, October 2007, doi: 10.1016/j.fusengdes.2007.03.008

[20] https://access.redhat.com/site/documentation/en-US/Red_Hat_Enterprise_MRG/1.3/html-single/Tuna_User_Guide/index.html [Acceded 2013/09/30]

[21] <http://www.gnu.org/software/grub/> [Acceded 2013/10/01]

[22] G. Raupp, R. Cole, K. Behler, M. Fitzek, P. Heimann, A. Lohs, K. Lüddecke, G. Neu, J. Schacht, W. Treutterer, D. Zasche, Th. Zehetbauer, M. Zilker, “A “Universal Time” system for ASDEX Upgrade”, Fusion Engineering and Design, Volume 66-68, September 2003, doi:10.1016/S0920-3796(03)00381-8

[23] <http://www.iop.org/Jet/fulltext/EFDC090102.pdf> [Acceded 2013/09/14]

[24] <http://www.redhat.com/products/mrg/> [Acceded 2013/09/14]

[25] A.J.N. Batista, C. Leong, V. Bexiga, A.P. Rodrigues, A. Combo, B.B. Carvalho, J. Fortunato, M. Correia, J.P. Teixeira, I.C. Teixeira, J. Sousa, B. Gonçalves, C.A.F. Varandas, “ATCA/AXIe compatible board for fast control and data acquisition in nuclear fusion experiments”, *Fusion Engineering and Design*, volume 87, Issue 12, pages 2131-2135, December 2012, <http://dx.doi.org/10.1016/j.fusengdes.2012.05.005>

8 - Appendices

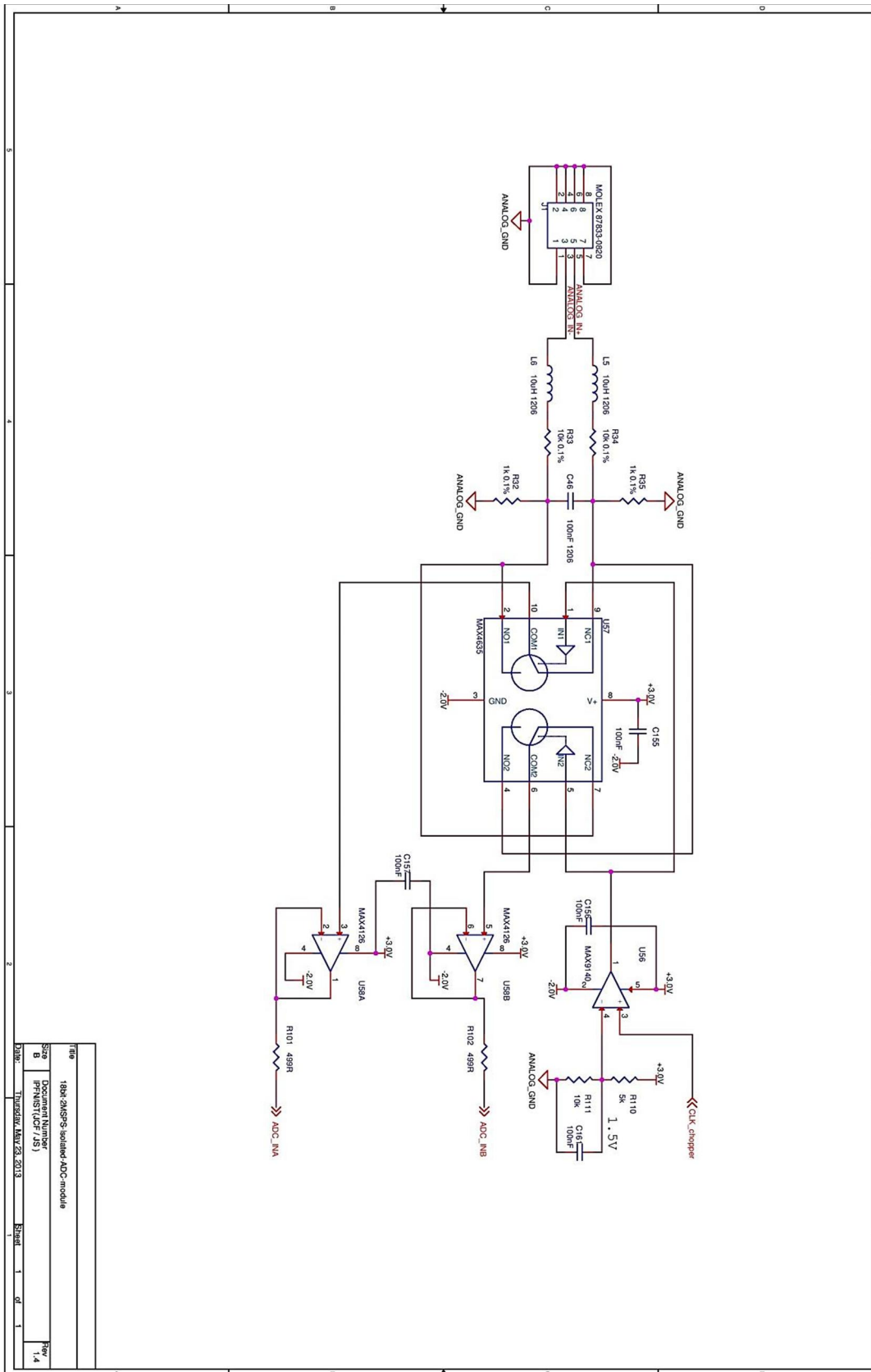


Figure 80 – Schematic of part of the ADC module developed by IPFN

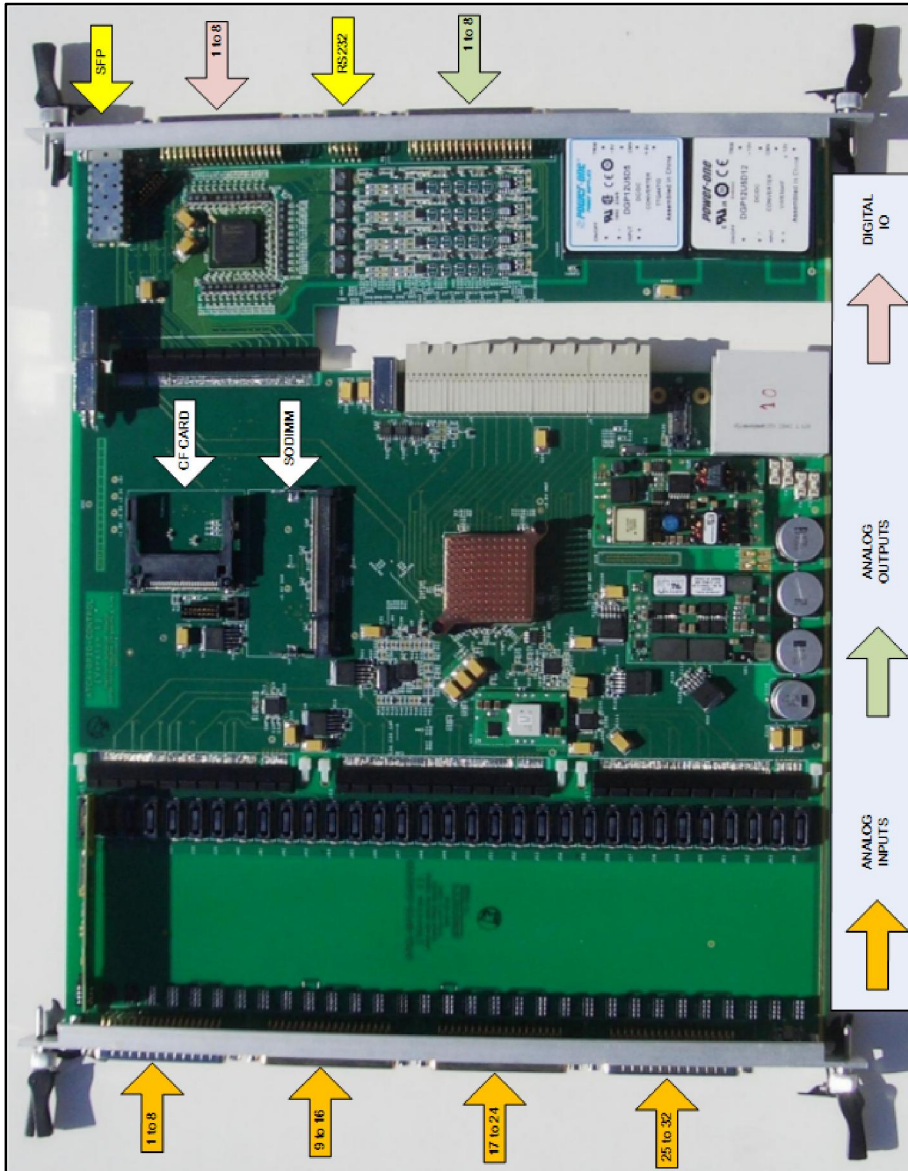


Figure 82 - Used ATCA board

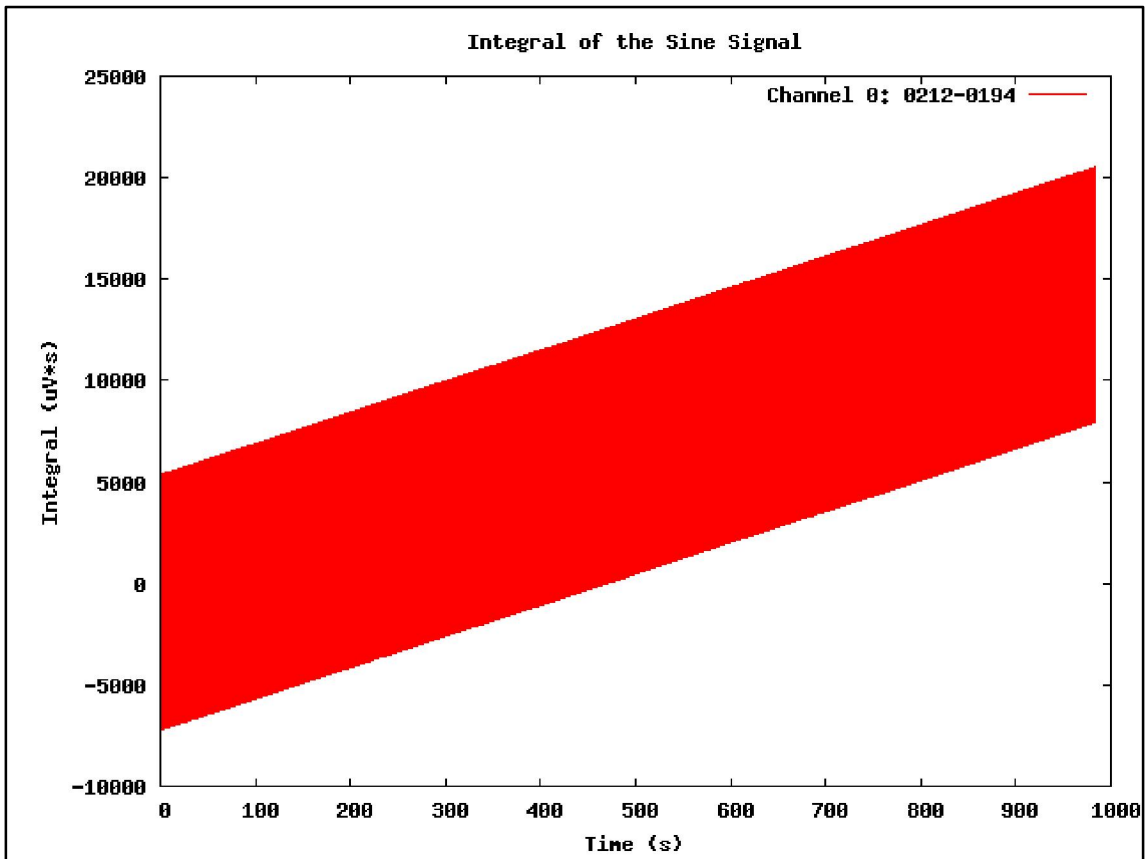


Figure 83 - Integral of Sine signal

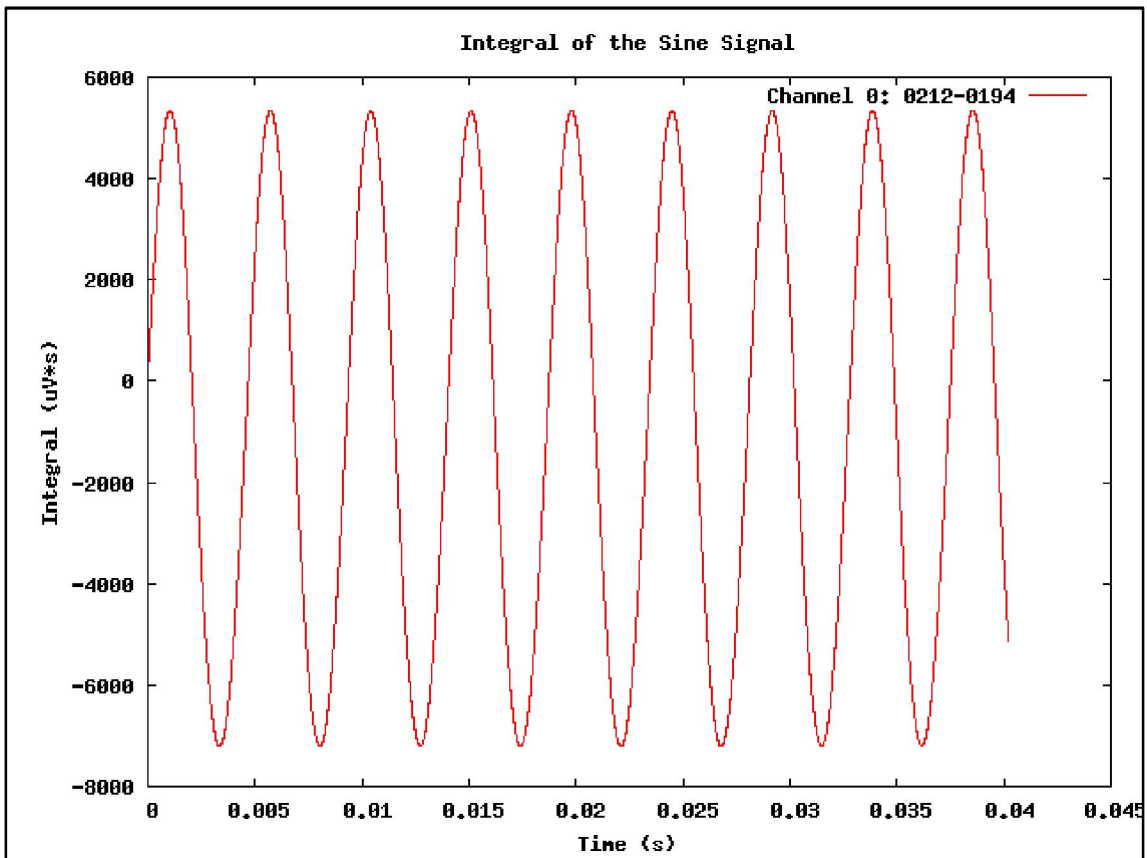


Figure 84 - Detail of Integral of Sine signal

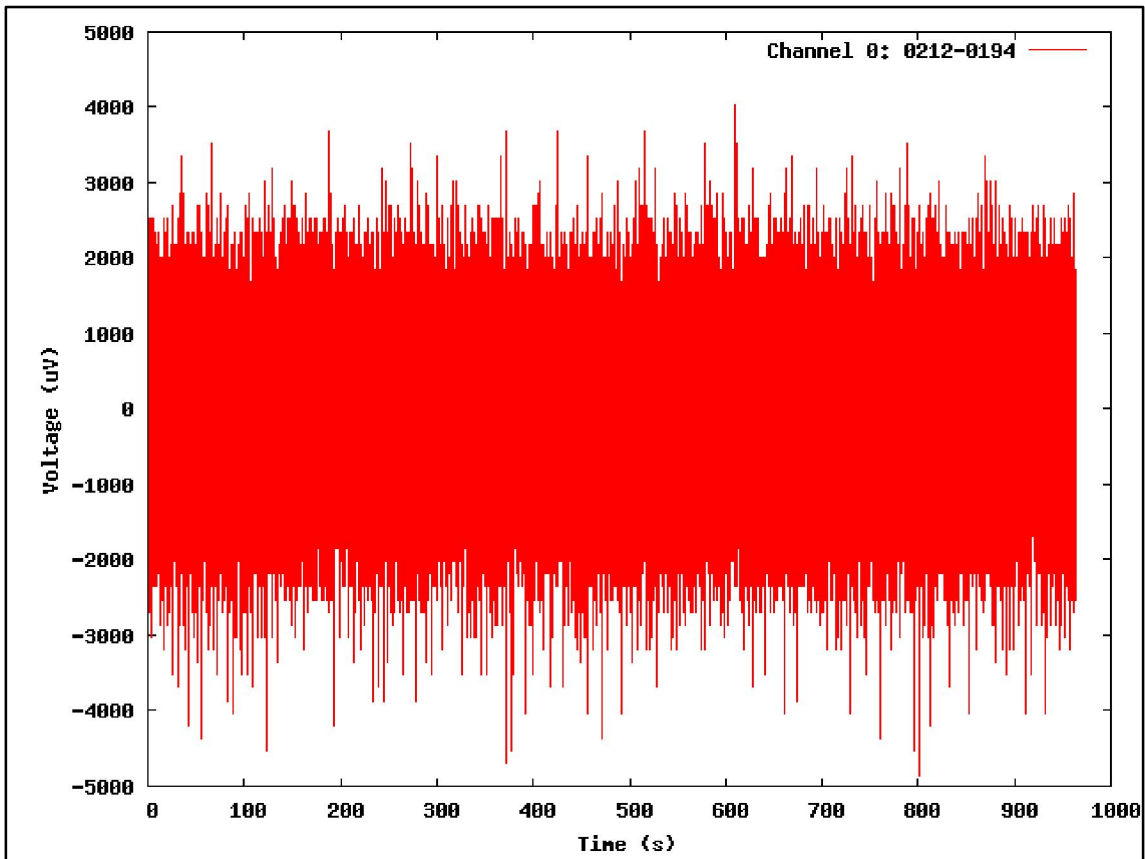


Figure 85 - Offset of one module (acquisition with constant temperature)

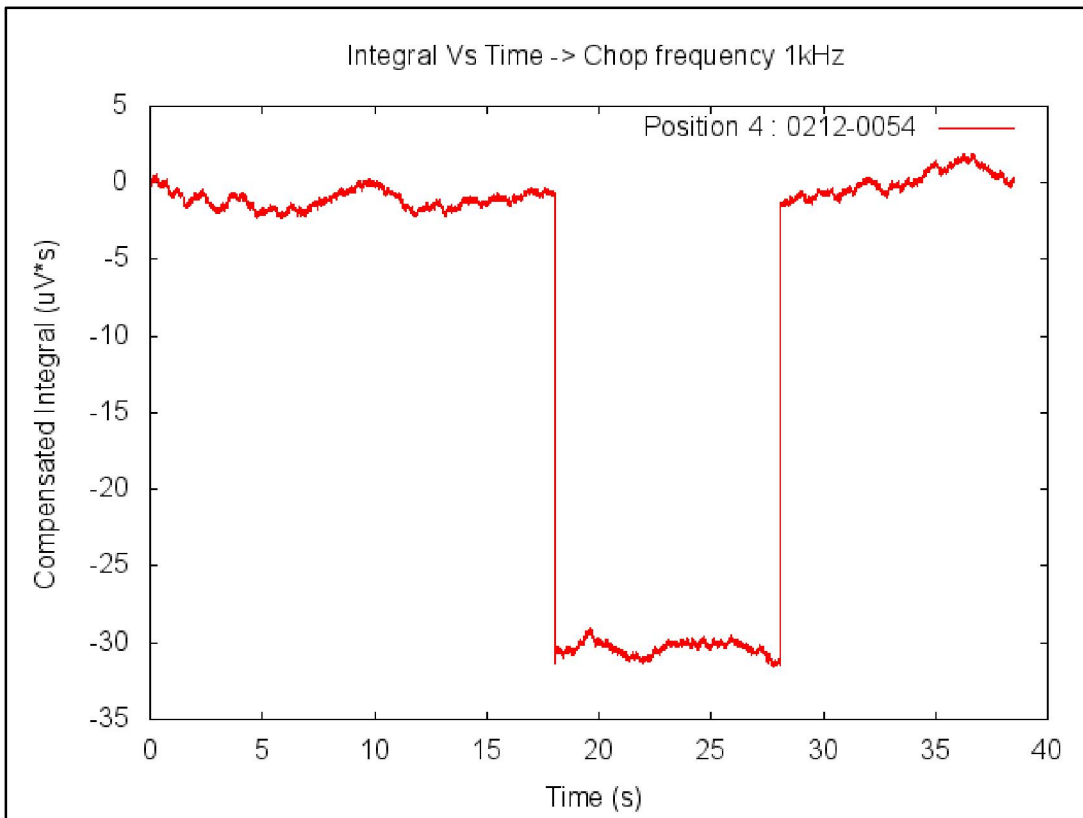


Figure 86 - Pre-Compensated Integral, the acquisition was during 40 seconds and the pre-compensation was done at 10 seconds. The difference from figure Figure 60 is that the terminals of the coil were switch and the signal is shown inverted

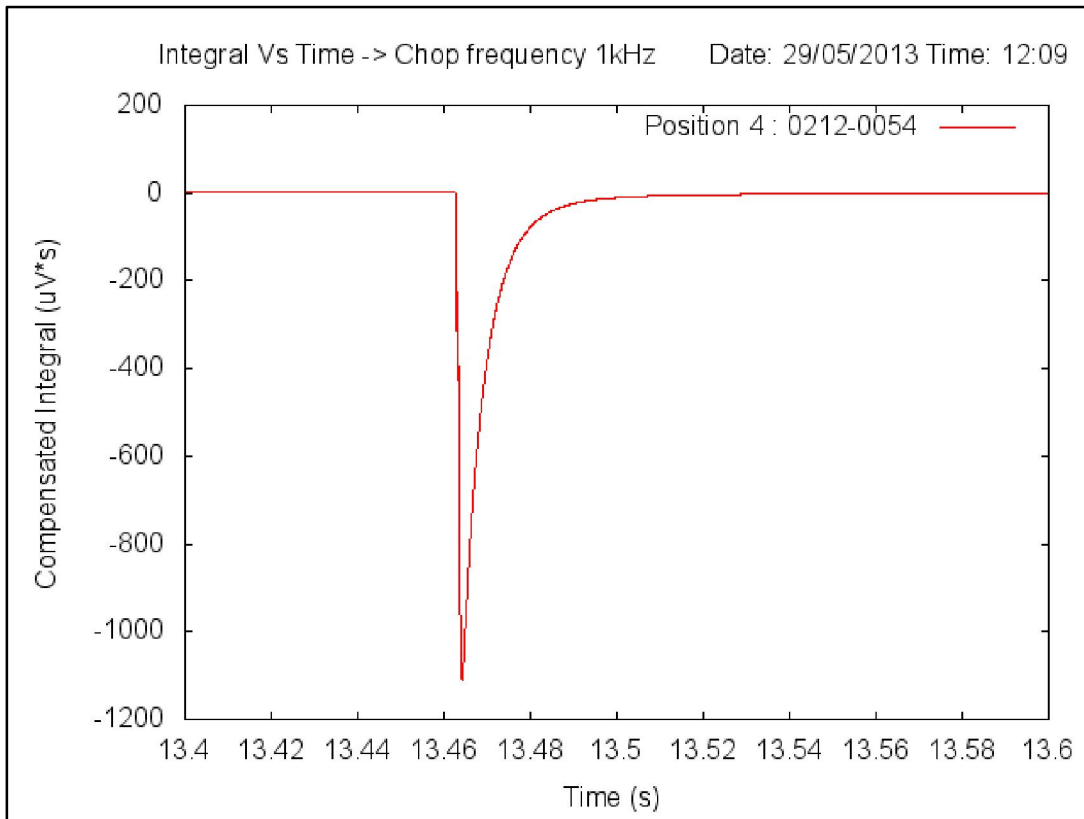


Figure 87 - Detail of a Pre-Compensated Integral, the acquisition was during 40 seconds and the pre-compensation was done at 10 seconds

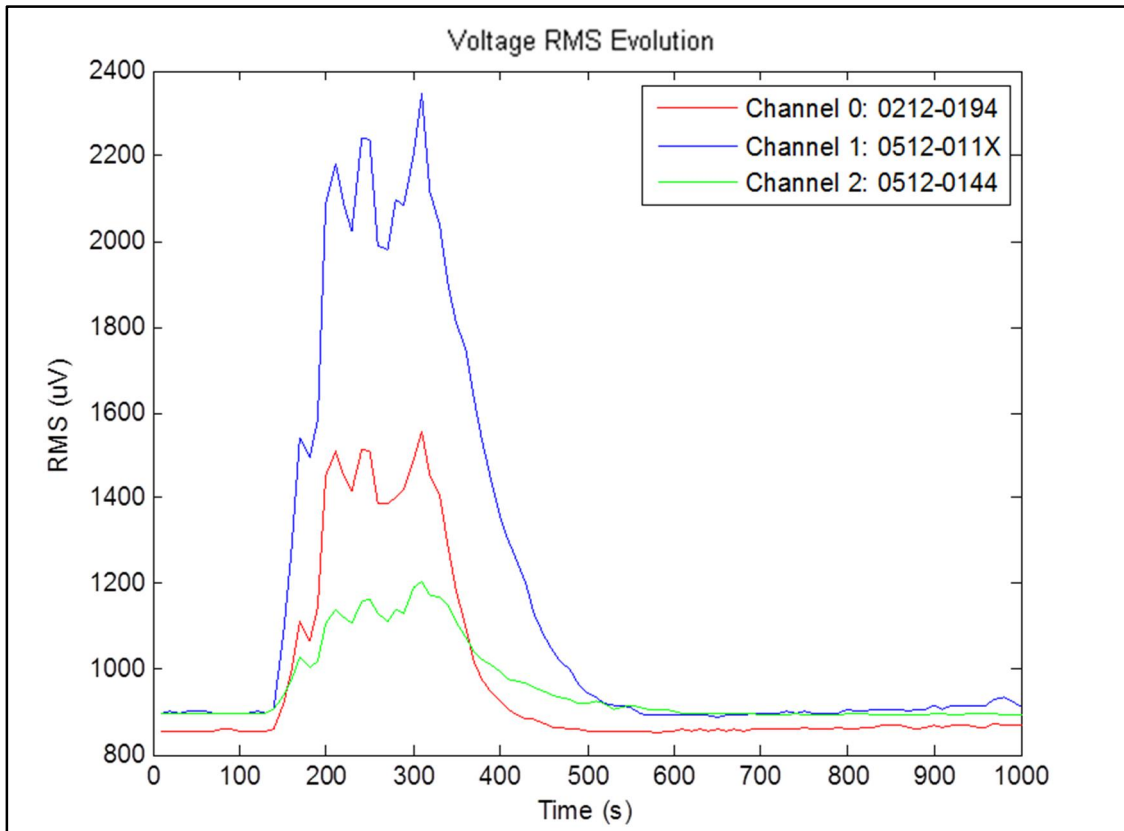


Figure 88 - Values of the voltage RMS through the acquired data during acquisition 3b, (acquisition with temperature variation)

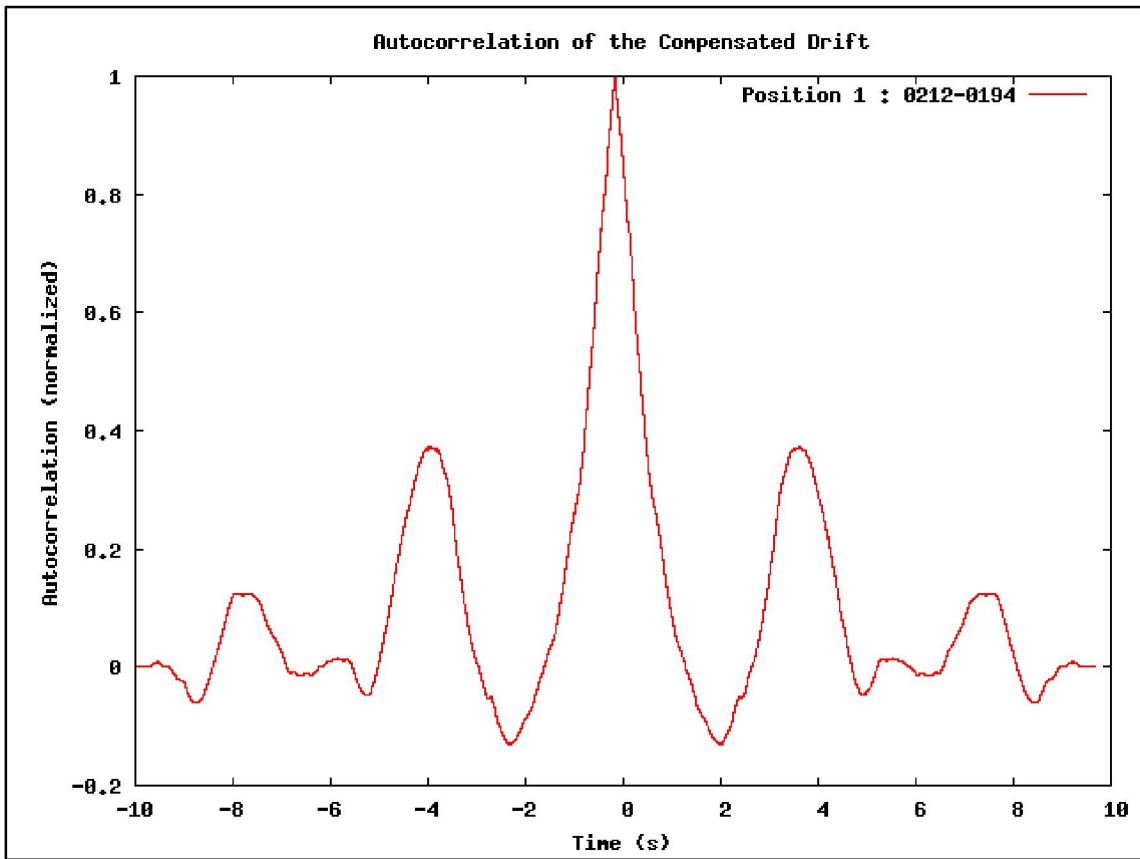


Figure 89 – Autocorrelation of the compensated integral of noise (the terminals of the module were short-circuited), the acquisition lasted 10 seconds

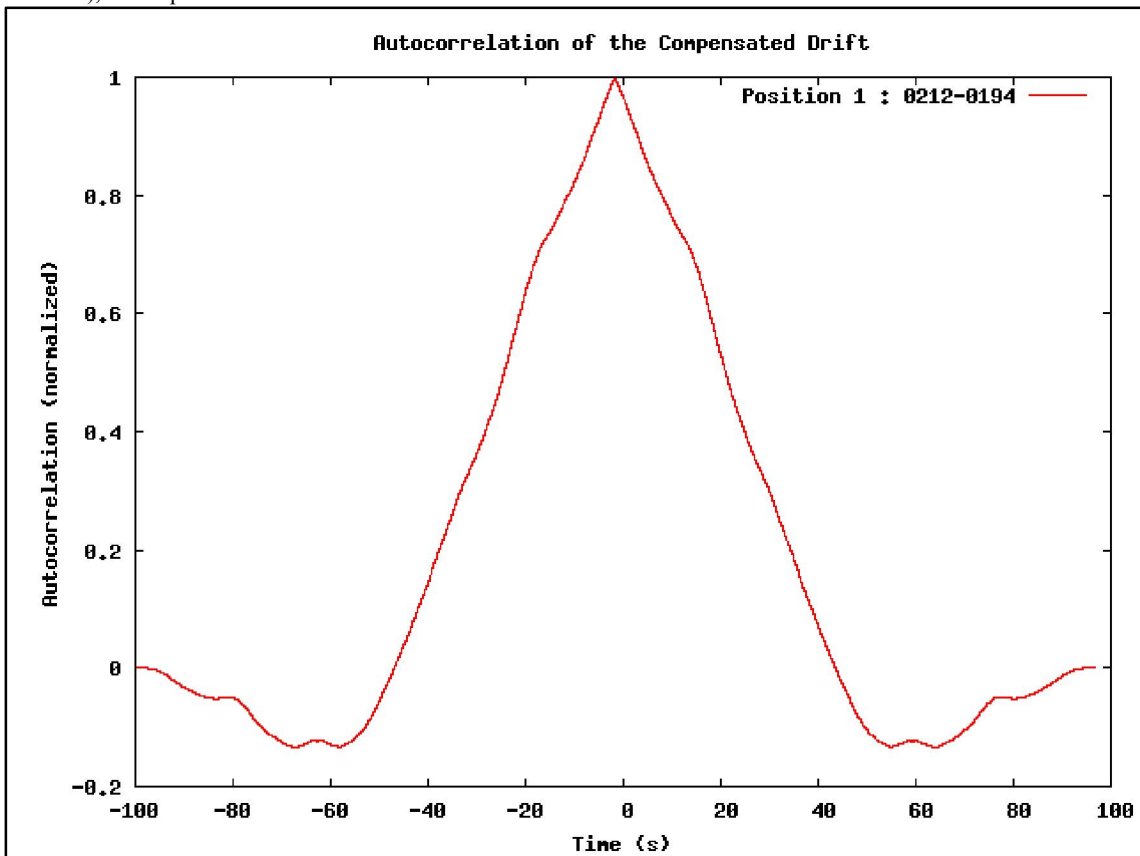


Figure 90 - Autocorrelation of the compensated integral of noise (the terminals of the module were short-circuited), the acquisition lasted 100 seconds

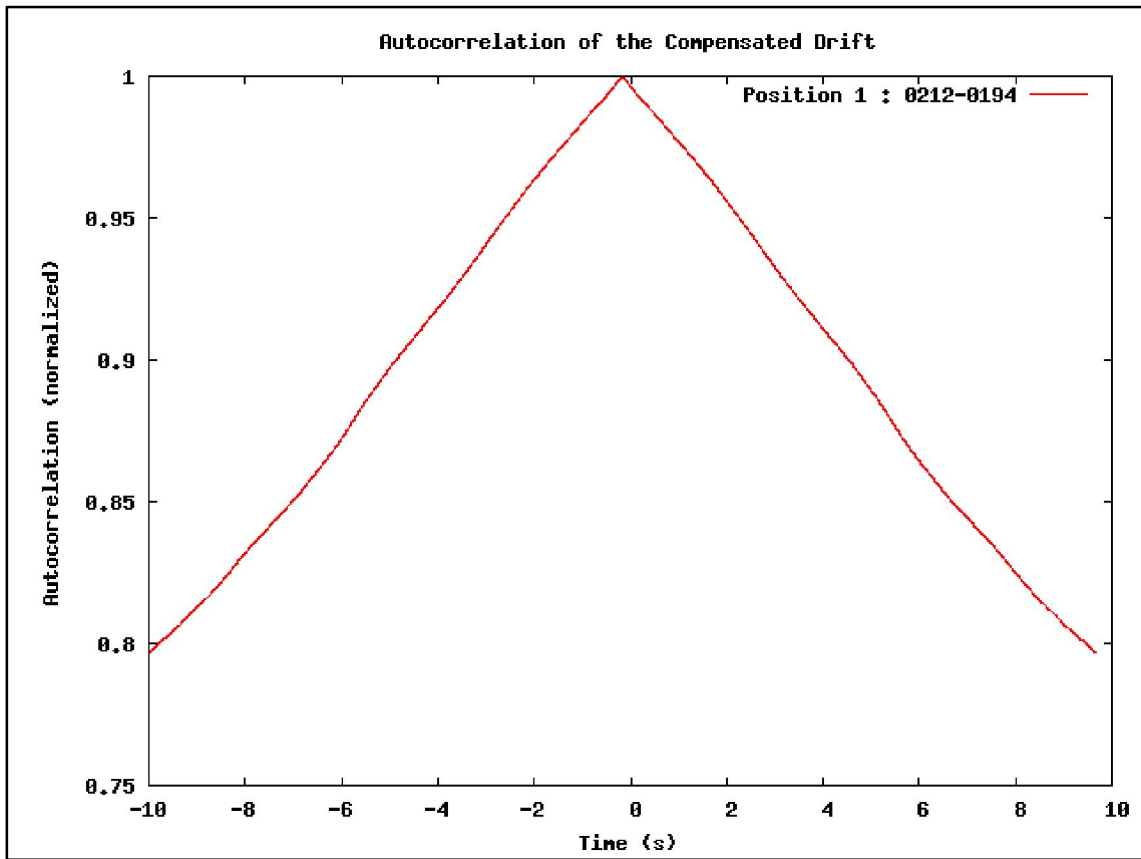


Figure 91 - Autocorrelation of the compensated integral of noise (the terminals of the module were short-circuited). The acquisition lasted 100 seconds, it is the same as in Figure 90, but the autocorrelation was limited to the first 10 seconds.

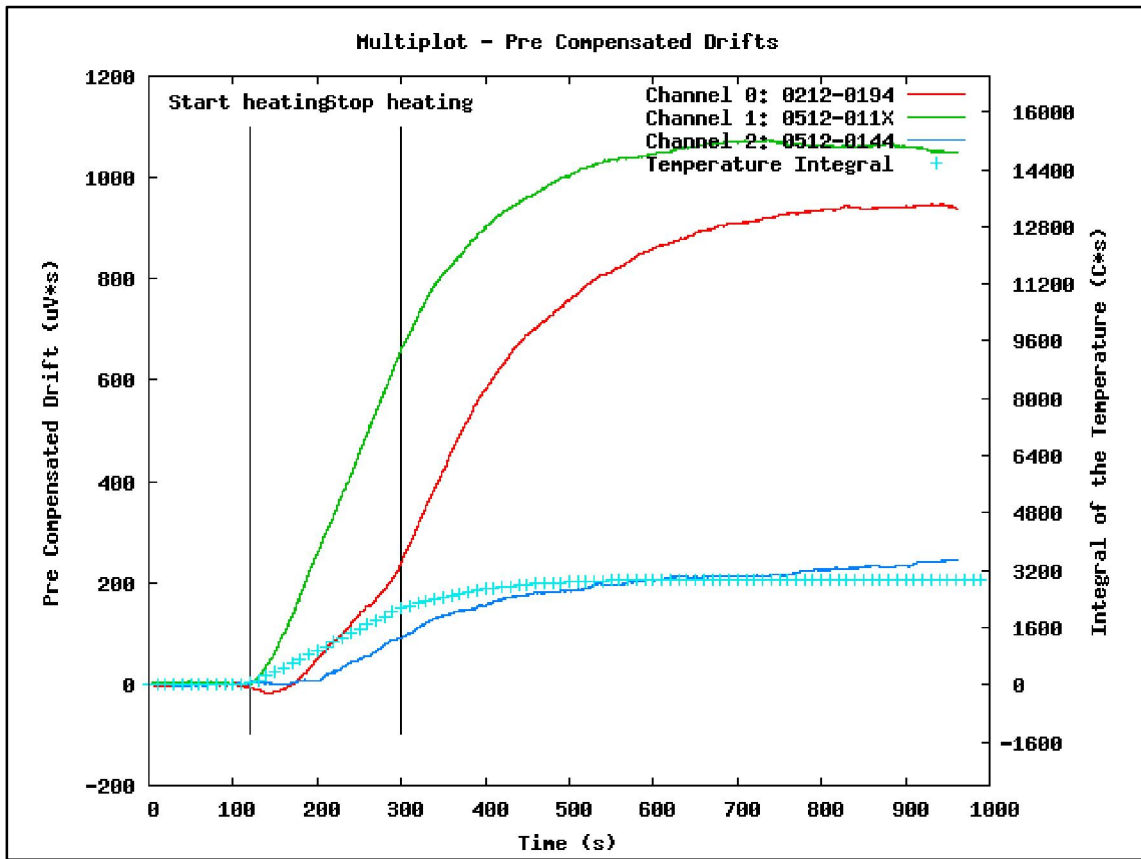


Figure 92 - Multiplot of all Pre Compensated Drift on acquisition 3a with the integral of the temperature adjusted to the channel 2 integral curve

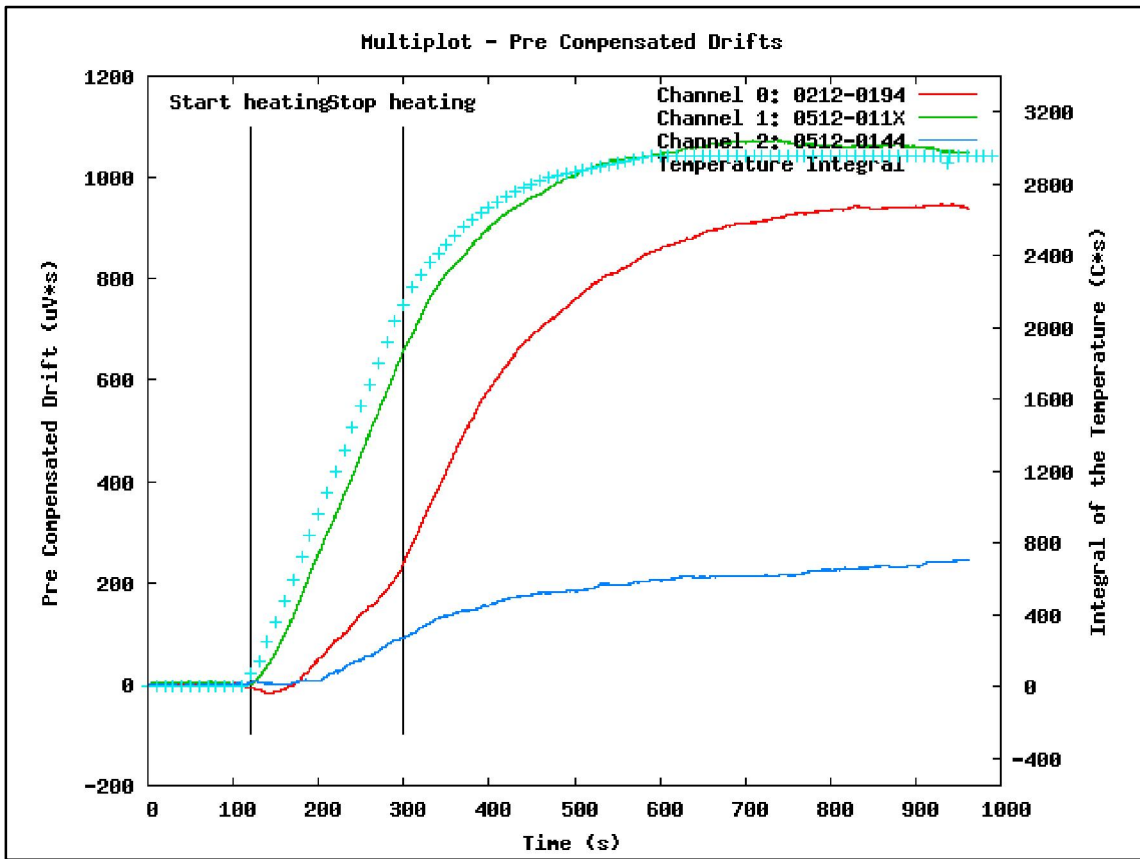


Figure 93 - Multiplot of all Pre Compensated Drift on acquisition 3a with the integral of the temperature adjusted to the channel 1 integral curve

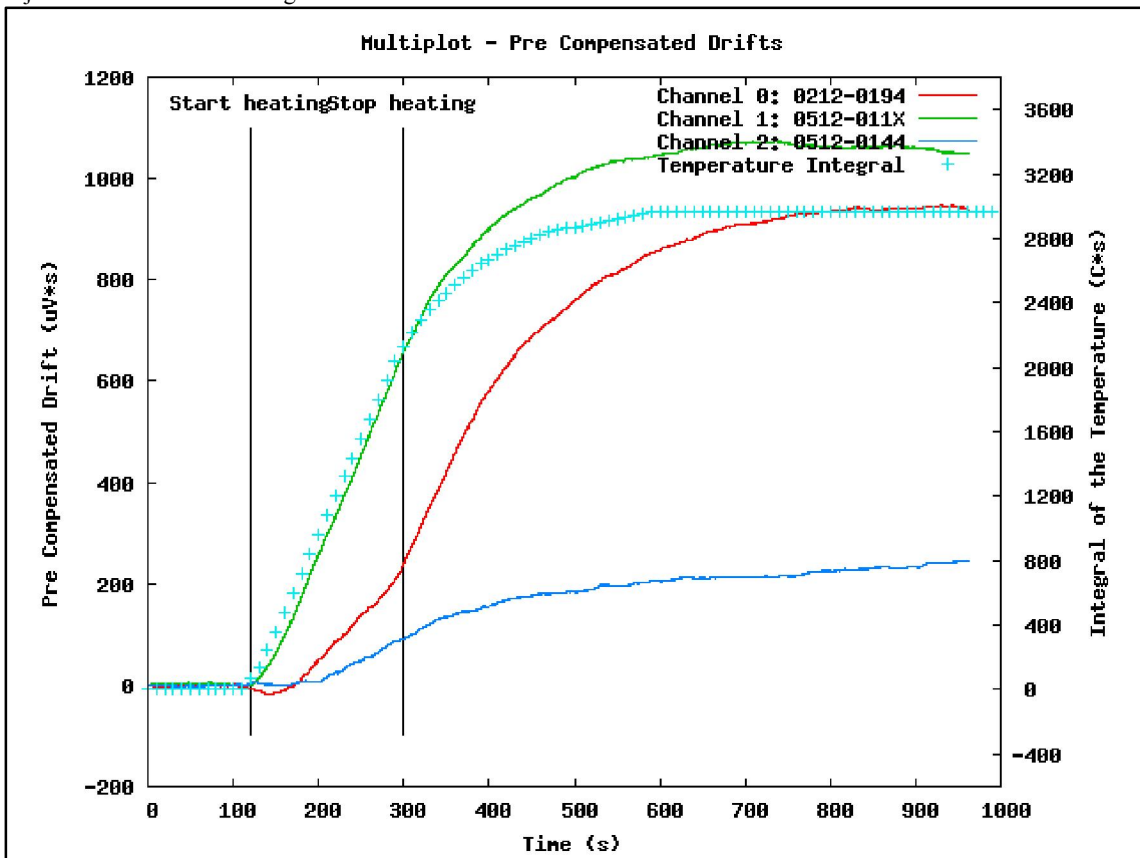


Figure 94 - Multiplot of all Pre Compensated Drift on acquisition 3a with the integral of the temperature adjusted to the channel 0 integral curve

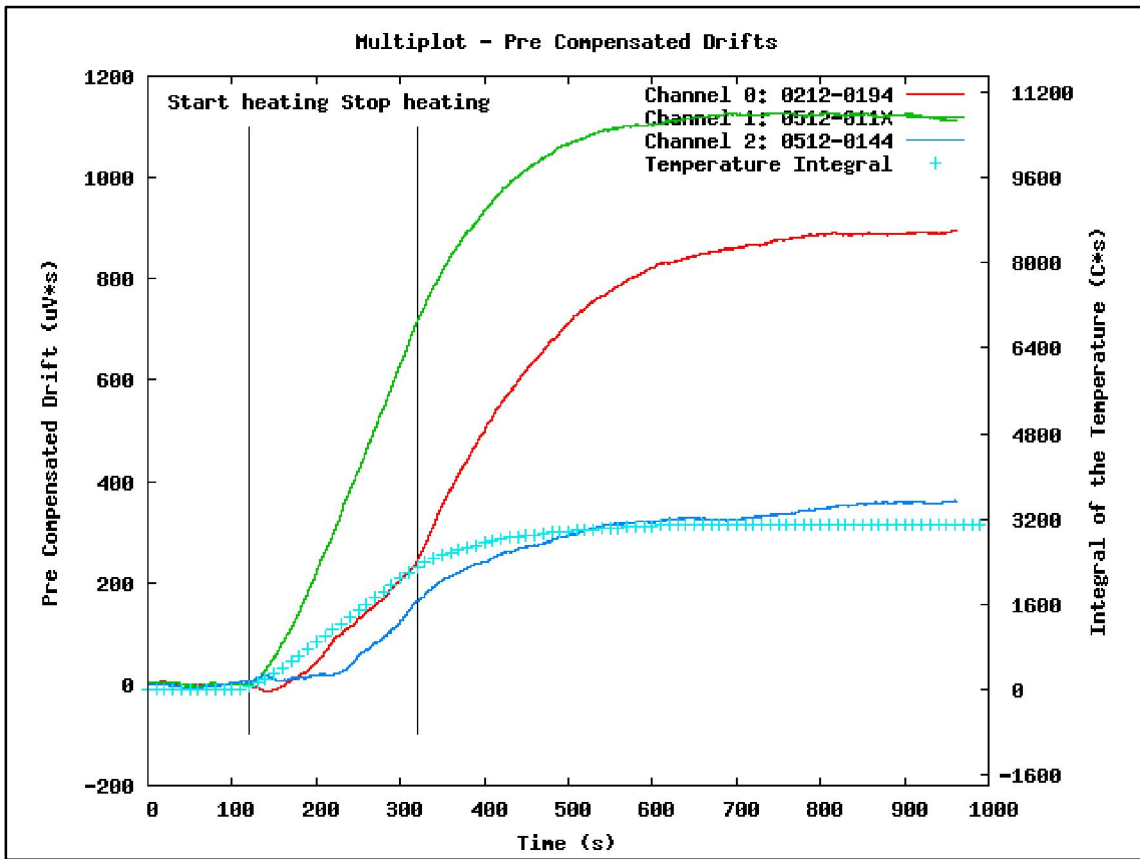


Figure 95 - Multiplot of all Pre Compensated Drift on acquisition 3b with the integral of the temperature adjusted to the channel 2 integral curve

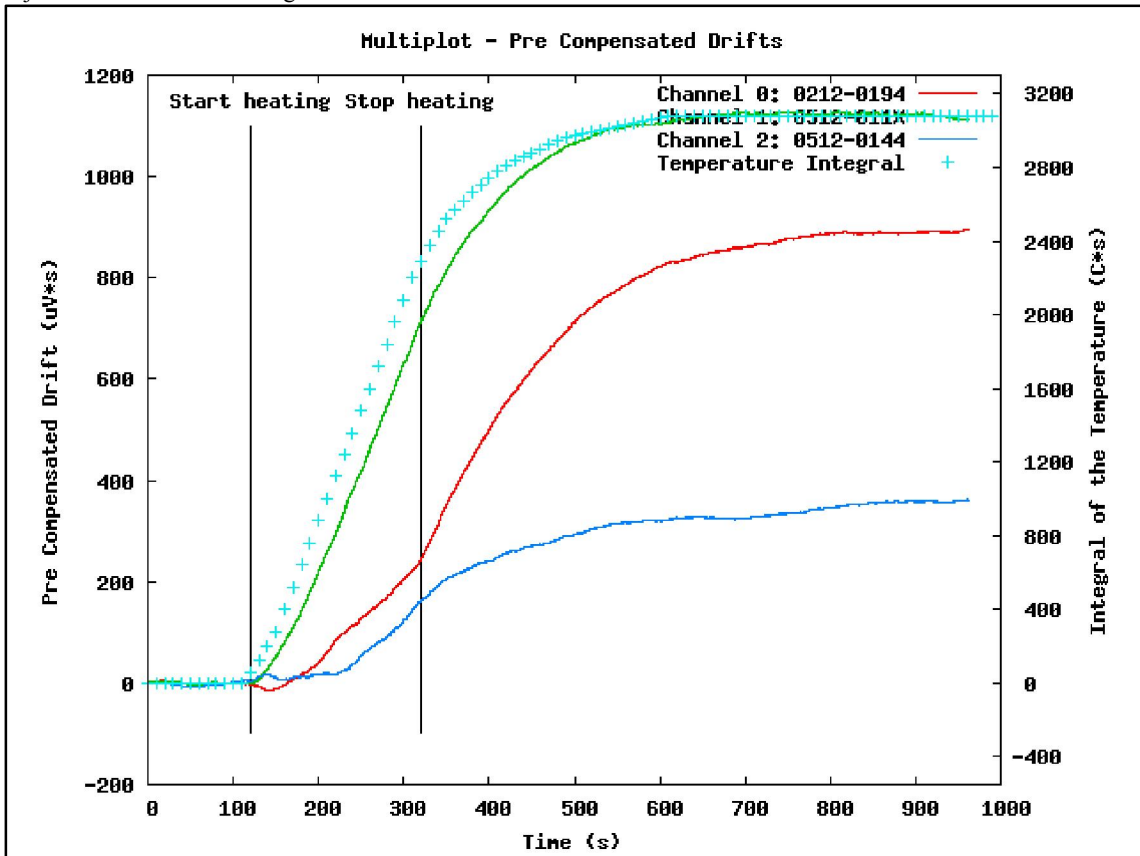


Figure 96 - Multiplot of all Pre Compensated Drift on acquisition 3b with the integral of the temperature adjusted to the channel 1 integral curve

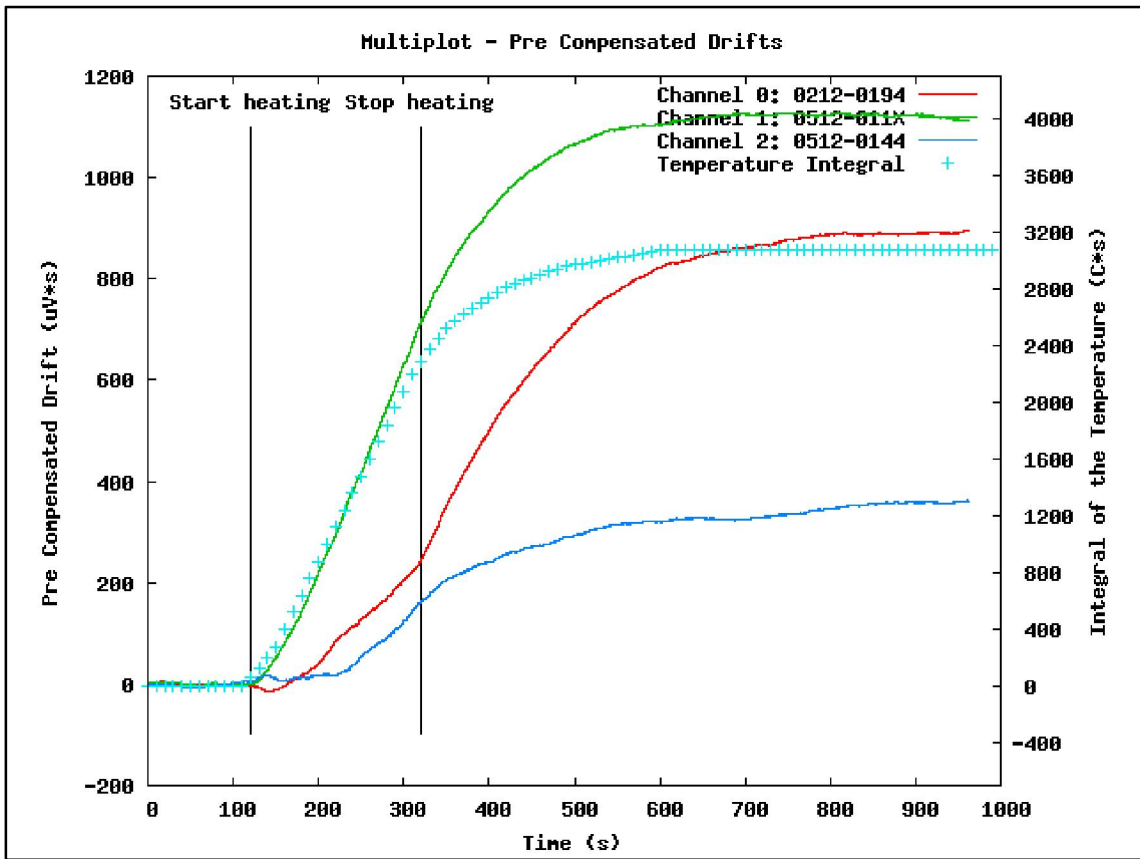


Figure 97 - Multiplot of all Pre Compensated Drift on acquisition 3b with the integral of the temperature adjusted to the channel 0 integral curve

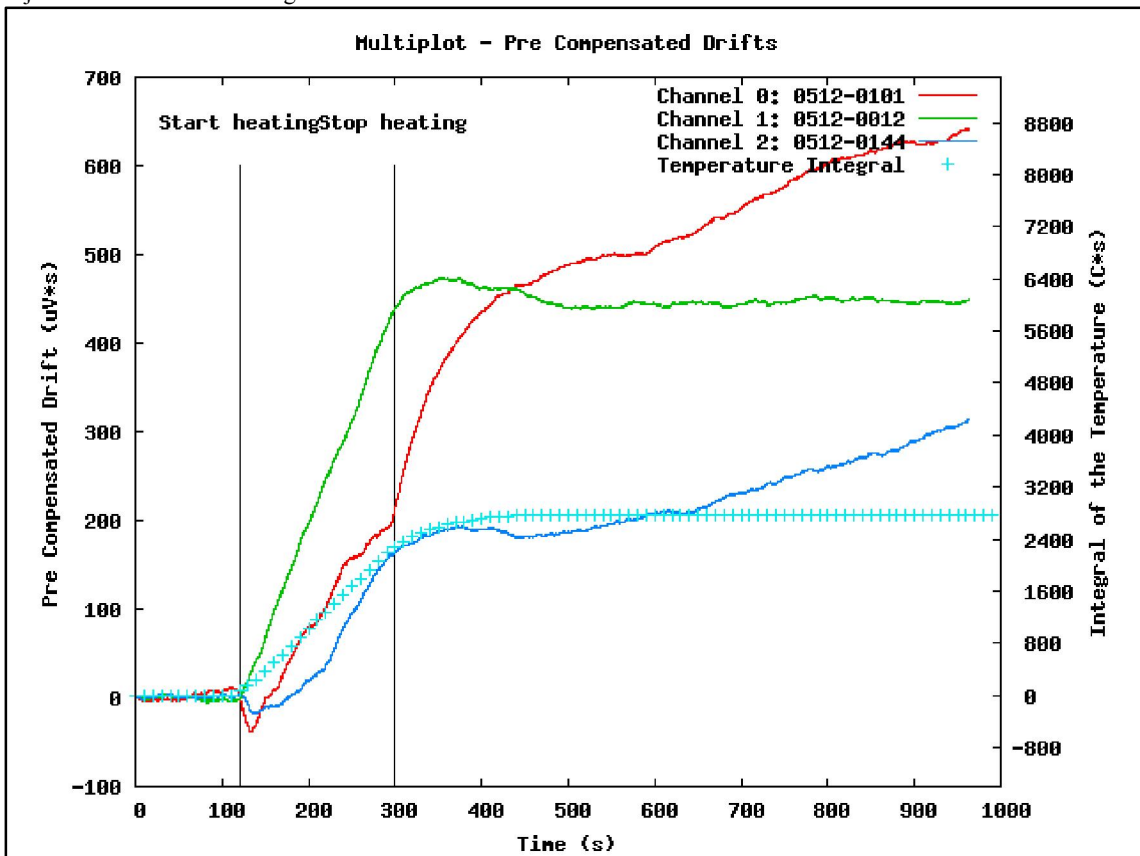


Figure 98 - Multiplot of all Pre Compensated Drift on acquisition 4a with the integral of the temperature adjusted to the channel 2 integral curve

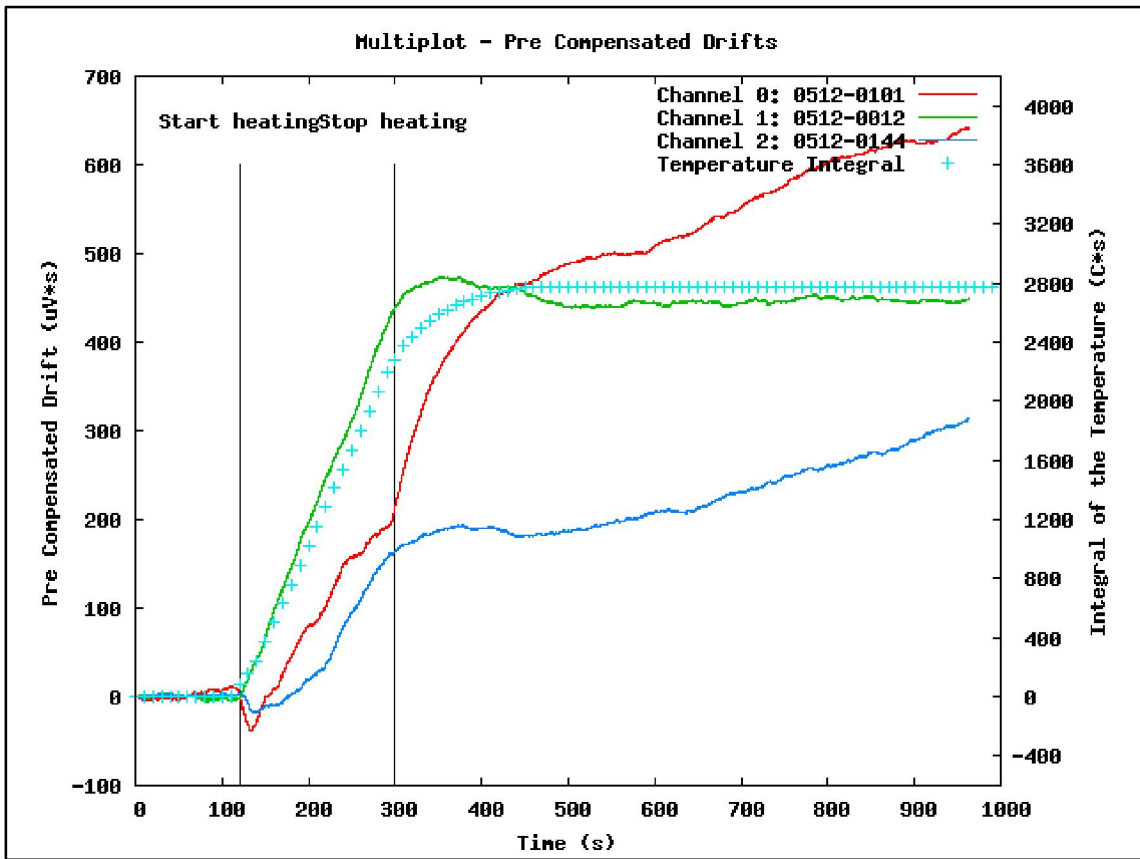


Figure 99 - Multiplot of all Pre Compensated Drift on acquisition 4a with the integral of the temperature adjusted to the channel 1 integral curve

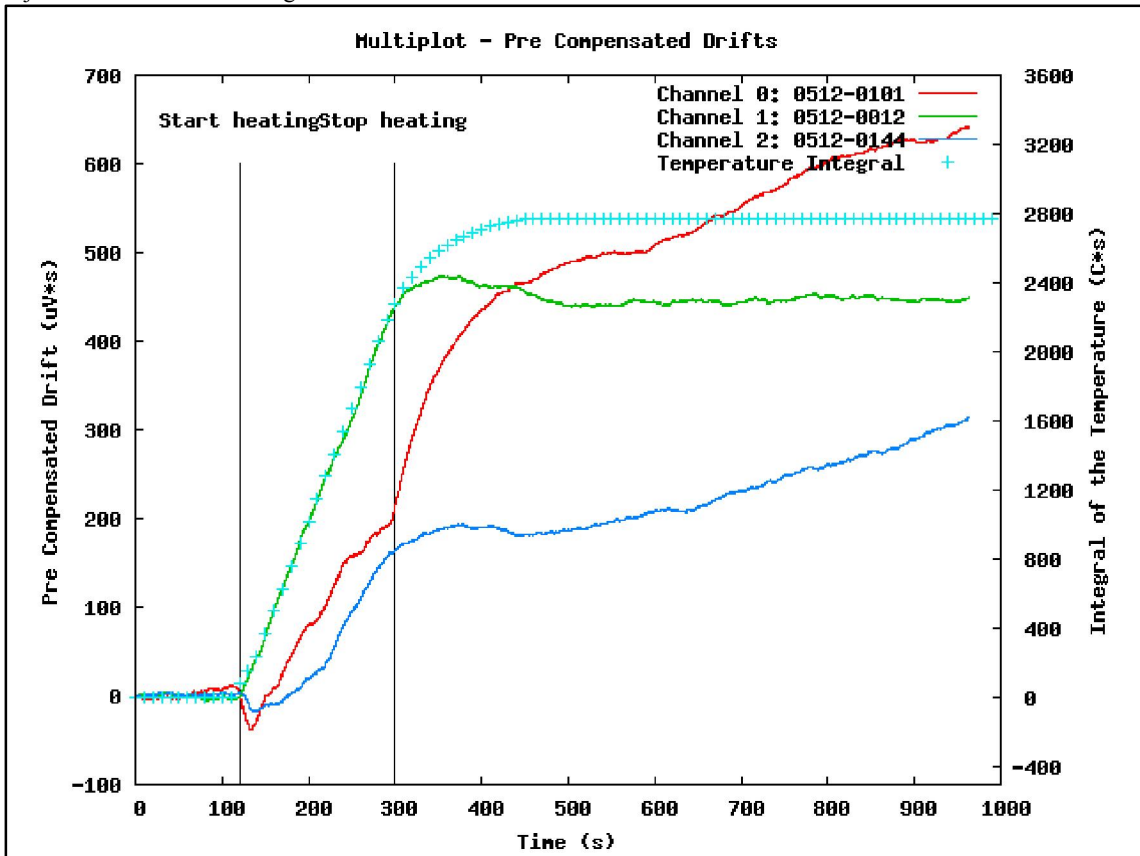


Figure 100 - Multiplot of all Pre Compensated Drift on acquisition 4a with the integral of the temperature adjusted to the channel 0 integral curve

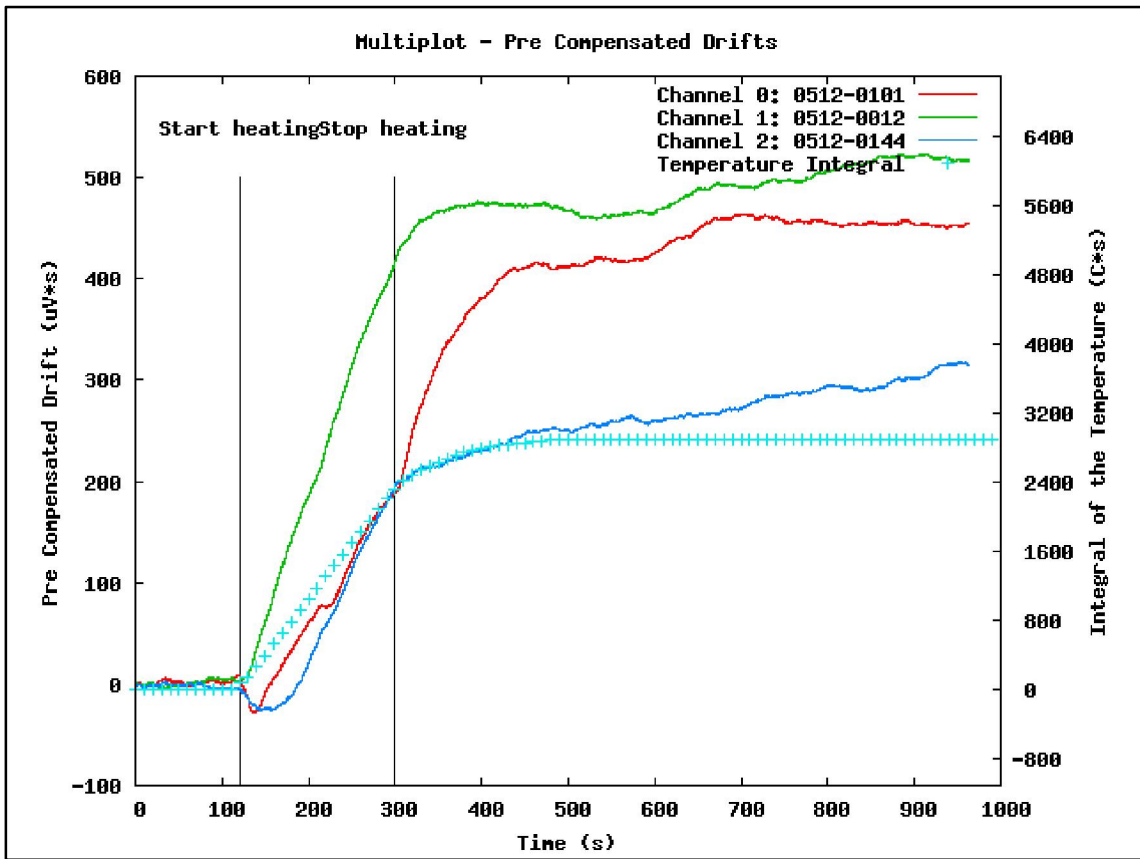


Figure 101 - Multiplot of all Pre Compensated Drift on acquisition 4b with the integral of the temperature adjusted to the channel 2 integral curve

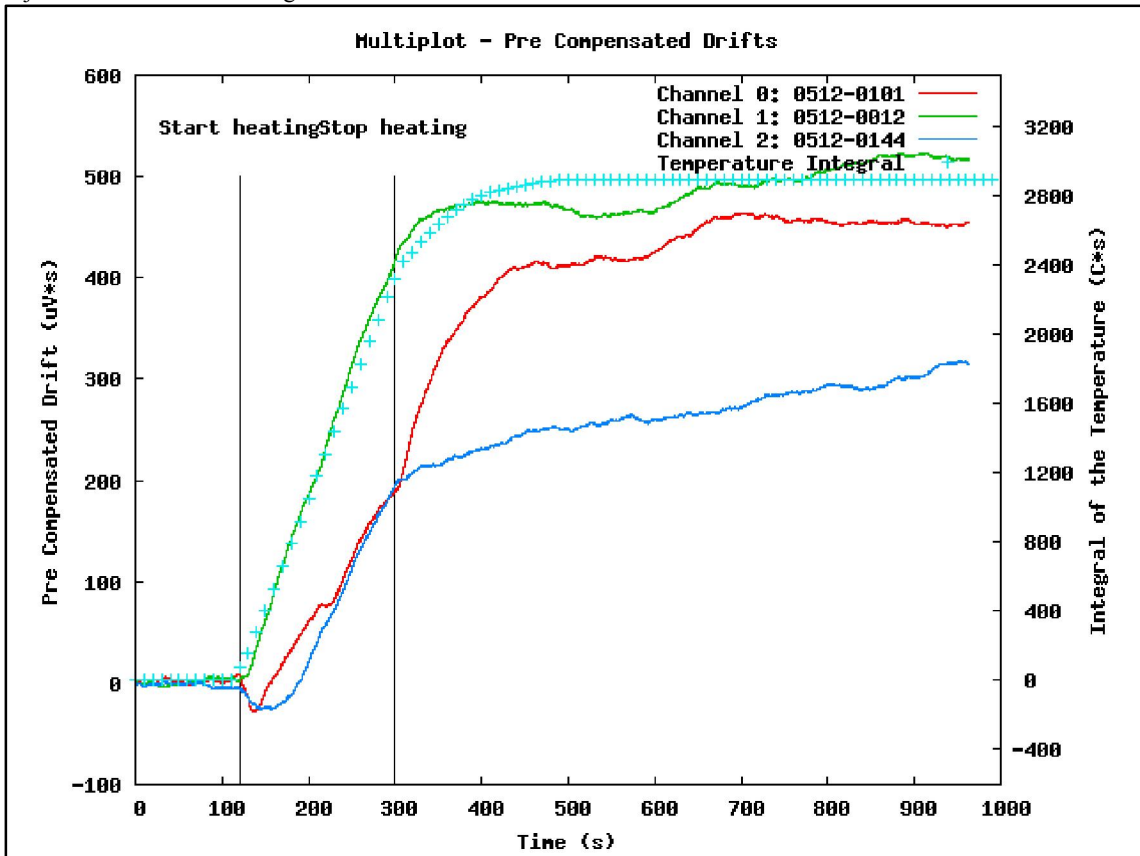


Figure 102 - Multiplot of all Pre Compensated Drift on acquisition 4b with the integral of the temperature adjusted to the channel 1 integral curve

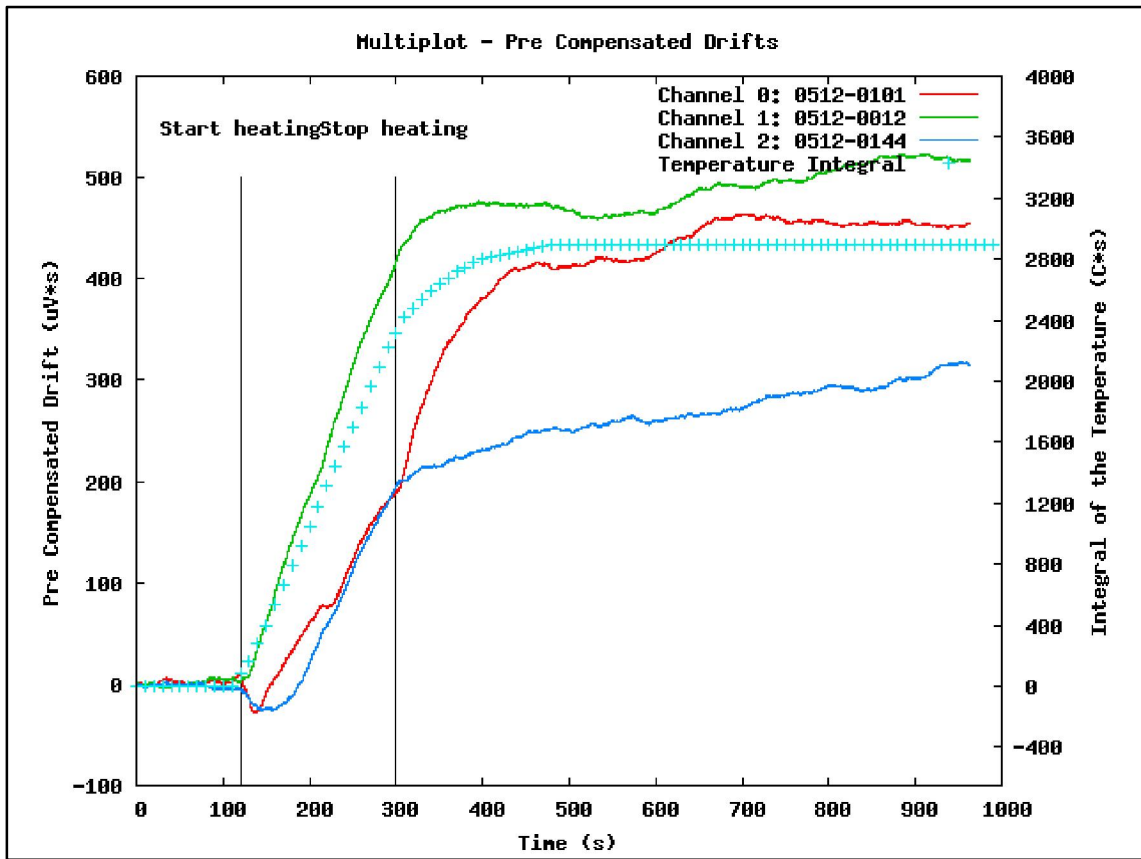


Figure 103 - Multiplot of all Pre Compensated Drift on acquisition 4b with the integral of the temperature adjusted to the channel 0 integral curve